PARAMETRIC EVALUATION OF WATER TREEING IN EPR-INSULATED MEDIUM VOLTAGE CABLES USING FINITE ELEMENT ANALYSIS

A Thesis

SUBMITTED TO THE FACULTY OF THE

UNIVERSITY OF MINNESOTA DULUTH

BY

SEAN MICHAEL O'BRIEN

IN PARTIAL FULFILLMENT OF THE REQUIREMENTS

FOR THE DEGREE OF

MASTER OF SCIENCE IN MECHANICAL ENGINEERING

Advisor: Dr. Brian Hinderliter

May 2021

Acknowledgements

I would first like to thank my parents John and Tammy O'Brien who have wholeheartedly supported my educational and career goals and have always pushed me to excel in everything I do. Without their guidance and assistance, I would not be the person I am today.

I would like to thank Dr. Brian Hinderliter for introducing me to the topic of this thesis, guiding me through the research process, and aiding me in my role as a teaching assistant. His support and encouragement kept me motivated and ensured that I remained focused on completing this thesis.

I would like to thank Drs. Robert Duckworth, Margaret Elmer-Dixon, Michael Greminger, and Melissa Maurer-Jones for agreeing to serve on my thesis committee.

I would like to thank my fellow graduate research associates, Alec Becker and Adam Finke, for their support and always being available to discuss both research and non-research related topics.

I would like to thank Drs. Venkata Gireesh Menta, Emmanuel Enemuoh, and Abdulaziz Abutunis for supporting me as a teaching assistant. The unique opportunity given to me in this role provided me immense joy and expanded my enthusiasm for engineering and teaching.

Lastly, I would like to thank everyone I had the pleasure of working with these past six years at the University of Minnesota Duluth. In one way or another, you have all contributed to this thesis.

Abstract

Medium voltage (MV) electric cables are used extensively in industrial settings, including nuclear power plants (NPPs). In NPPs, these cables provide supplementary power for safety systems to continue operating during emergency events. Despite efforts to maintain these cables, premature failure is known to occur, with the predominant causal factor being water tree-induced degradation of the cable's insulation component. To better understand the effects of this degradation source, this thesis presents a parametric evaluation of various water tree and cable parameters using finite-element analysis (FEA). The parameters being evaluated for a MV cable insulated with ethylene propylene rubber (EPR) are water tree depth, composition, and geometry, as defined by aspect ratio (AR), and cable operating frequency and temperature. Evaluation is performed in five separate but interrelated areas pertaining to the measurement of degradation: global capacitance, global resistance, voltage and electric field distribution, localized specific energy absorption rate, and localized temperature rise. Results show that the rate of water tree-induced degradation is affected by each parameter. In general, rate of degradation was found to be directly related with water tree depth and AR, and cable temperature, but inversely related with cable operating frequency. Although values differed, these trends were largely maintained regardless of water tree composition. The results and findings of this parametric evaluation have provided an advanced understanding of water tree degradation in MV EPR-insulated cables. In addition, an argument for further use of FEA in conjunction with physical cable testing was presented, with the conclusion being that there exists a strong motivation to pair the two together.

Table of Contents

List of Tables

List of Figures

List of Equations

List of Abbreviations

AC.....Alternating Current

Ansys.....Ansys Electronics Desktop

AR.....Aspect Ratio

ASTM.....American Society for Testing and Materials

COMSOL.....COMSOL Multiphysics

$CuSO_4$.....Aqueous Copper Sulfate

DC.....Direct Current

EPR.....Ethylene Propylene Rubber

FEA.....Finite-Element Analysis

H_2O.....Pure Distilled Water

HV.....High Voltage

LTR.....Localized Temperature Rise

LV.....Low Voltage

MV.....Medium Voltage

NEI.....Nuclear Energy Institute

NPP.....Nuclear Power Plant

PD.....Partial Discharge

PDC.....Polarization-Depolarization Current

PE.....Polyethylene

pH.....Potential of Hydrogen

PVC.....Polyvinyl Chloride

Q3D.....Quasi-Three-Dimensional

RF-EMF.....Radio Frequency Electromagnetic Field

SAR.....Specific Energy Absorption Rate

TDR.....Time Domain Reflectometry

TIRI.....Thermal Infrared Imaging

U_0.....Usual Operating Voltage

VLF.....Very Low Frequency

V&V.....Validation and Verification

XLPE.....Cross-Linked Polyethylene

2D.....Two-Dimensional

3D.....Three-Dimensional

CHAPTER ONE:
INTRODUCTION

1.1 Background on Electric Cables

Electric power cables are typically categorized into one of three groups depending on their operating voltage: low voltage (LV) cables, which operate in the range of 2 kV and lower; medium voltage (MV) cables, which operate in the range of 2 kV to 35 kV; and high voltage (HV) cables, which operate in the range of 35 kV and higher [1]. Because of their small operating voltages, LV cables produce a less intense electric field than MV or HV cables. For this reason, they are commonly used in many building applications including lighting systems, sound and video devices, and alarm systems [2,3]. MV cables, which are the focus of this thesis, differ from LV cables in that they are constructed with a higher degree of precision that provides them extra protection [1]. These cables are typically found in many industrial settings including chemical plants, wind farms, and nuclear power plants (NPPs). MV cables are often used in industrial plants to provide backup power in the event of a power outage or plant emergency [4]. Cables classified as HV are used to distribute large amounts of power and are found in applications like radar systems, satellite propulsion, and transmission lines [5].

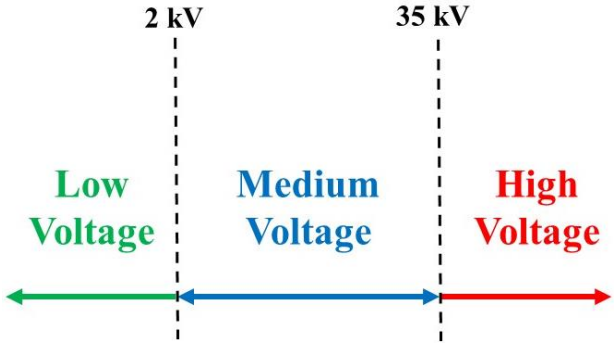

Figure 1. Visual representation of operating voltage categories.

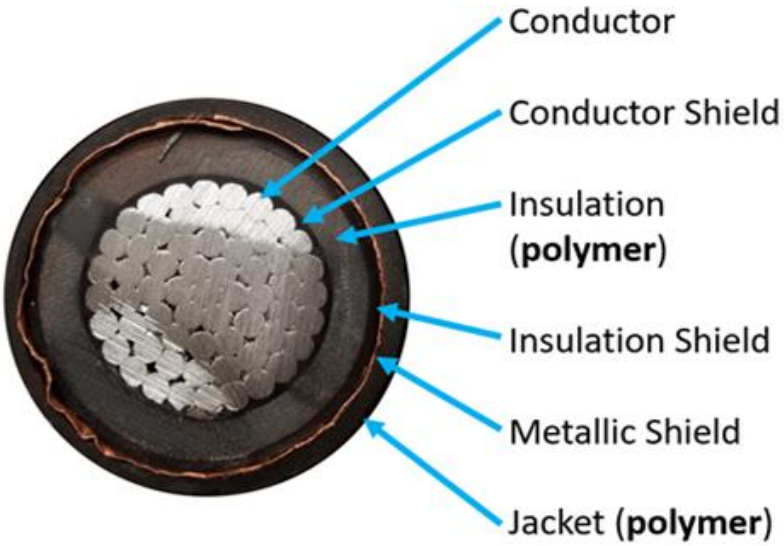

Figure 2. Cross-sectional view of a typical underground MV cable found in a NPP.

A typical MV cable consists of the following components starting from the cable's center: conductor, conductor shield, insulation, insulation shield, metallic shield, and jacket, as shown in Figure 2. The innermost component is the conductor, which typically consists of either a single solid strand made from aluminum or copper, or several wires of the same material neatly organized to form a roughly round shape. The purpose of the conductor is to carry the electrical current from the power source to the device being powered. The following layer that covers the conductor is known as the conductor shield. The conductor shield is a thin compound typically made from a semi-conductive polymer material containing carbon black. It works to provide a smooth circular boundary around the conductor which in turn reduces the stress concentration at the insulation interface [6]. The next layer is the insulation which is typically made from a polymer material and is the primary cable component this thesis is concerned with. The insulation acts as a barrier between the charged conductor and the grounded component by restricting the flow of electrical current through the cable. It must be constructed of a

material having a breakdown strength greater than the maximum electric field strength experienced during standard operation in order to prevent cable breakdown. For the majority of MV cables, the insulation is made of a thermosetting material like cross-linked polyethylene (XLPE) or ethylene propylene rubber (EPR), as shown in Figure 3.

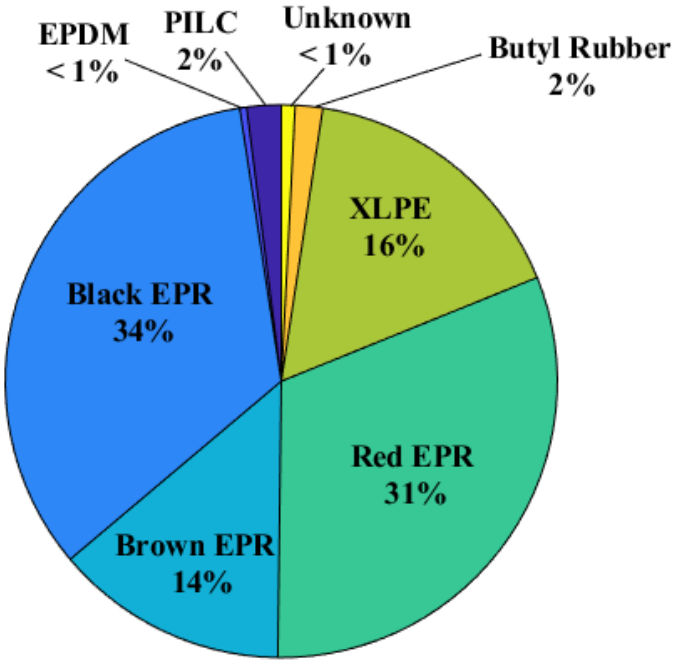

Figure 3. Distribution of insulation materials among MV cables from a Nuclear Energy Institute (NEI) survey conducted in 2005 [7].

After the polymer insulation comes the insulation shield, which functions similarly to the conductor shield. The insulation shield is typically made from a semi-conductive polymer material containing carbon black and works to provide a smooth and radial electric field in the cable. It is important for the insulation shield to be easily removed so that it can be terminated and spliced, but must also be securely bonded to the polymer insulation to prevent air voids from forming during operation. Air voids on their own are not particularly dangerous, but if water or moisture were to enter these voids, a

partial discharge (PD) inside the insulation could occur [8]. The next layer is the metallic shield, which is usually made from copper but occasionally from aluminum. The metallic shield has three main purposes: providing a path for the electrical current to flow to the grounded source, providing a path for the flow of fault currents, and lessening the touch potential in the case of accidentally hitting the cable during digging operations [8]. In addition, the metallic shield acts as a Faraday cage by confining the electric field inside the cable [6]. The outermost component of the cable is the polymer jacket, typically made from a thermoplastic like polyvinyl chloride (PVC) or a thermoset like Neoprene made by the company DuPont de Nemours. The role of the polymer jacket is that of protection; it provides mechanical strength to the cable, resistance to water ingress and oxidation damage, and a defense against unfavorable environmental conditions after installation, among other safeguarding measures [9].

1.2 Electric Cable Degradation

MV electric cables play an important role in the safety and wellbeing of NPPs. They provide supplementary power for safety systems to continue operating during emergency events, thus allowing for uninterrupted reactor operations for a short period of time [10]. Because of their critical importance to NPP operations, MV cables are typically installed in locations like underground concrete ducts or electrical conduits that work to lessen their exposure to the environment [10]. Although these cables are not operating continuously, they must still meet the same reliability and lifetime performance requirements of LV instrument and control cables located in-plant, which are rated for 40 years of operation from the initial plant start date in the United States [10]. For this

reason, and because of the harsh environments they typically operate in, all MV cables used in the operation of NPP safety systems are qualified before installation to determine their expected lifetimes [10]. In addition, many of these cables are tested periodically during plant shutdowns, though this testing and the testing that occurred prior to installation do not consider extreme accident conditions which may result in failure.

Figure 4. Failed underground electric cable [11].

Despite the significant effort taken to protect MV cables, the possibility of premature failure, shown in Figure 4, is still present and is an area of concern for cable degradation researchers and NPP operators. Shown in Figure 5 are the results of a NEI survey conducted in 2005 that highlights the prevalence of premature underground MV cable failure in the NPP industry. The primary function of the failed cables from the survey was the operation of safety systems like fire protection and backup power in the event of a plant blackout. Of the 47 NPPs that replied to the survey, 15 experienced at least one underground MV cable failure, with the most likely cause of failure being the result of extended submersion in a wet environment. Of the 50 reported failures, over

one-third occurred 19 years or less after starting operation, with the earliest reported failure occurring after only five years.

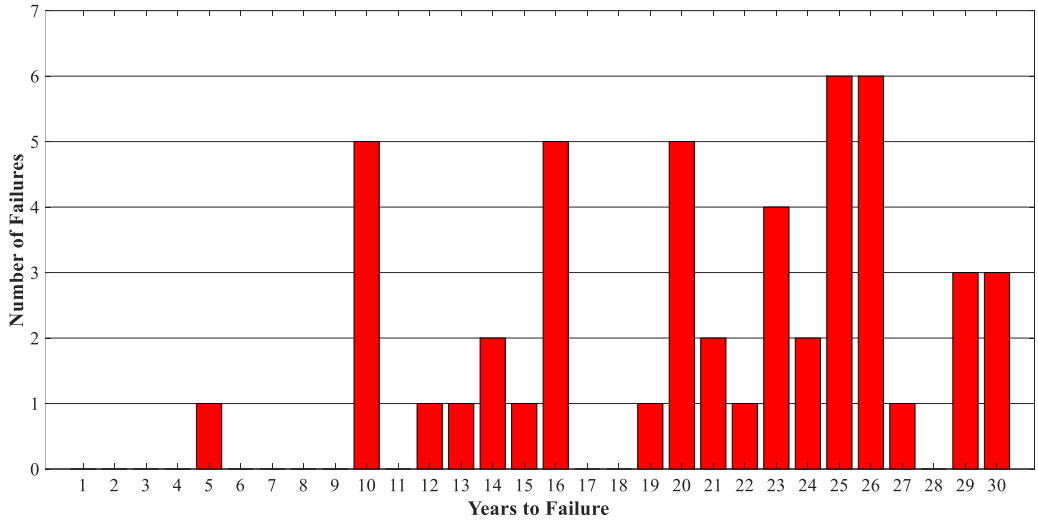

Figure 5. MV cable failure results from a 2005 NEI survey [7].

Given the significant number of failures reported and the potential plant interruptions they can cause, a better understanding of the methods of failure and the effects of environmental-induced degradation is required. The result will be improved accuracy of lifetime service predictions for cables which will help to inform their maintenance schedules. One issue preventing these cables from achieving their 40-year lifetime is the enhanced rate of degradation caused by various environmental stressors present in NPPs. These stressors have the potential to degrade the electrical and mechanical properties of the cables, which leads to accelerated aging and the potential for premature failure well before their rated lifetimes.

As shown in Figure 6, there are several categories of reported causes or causal factors related to premature cable failure. The most prominent categories from the study are: “Water/Moisture,” which includes all failures related to the presence of water inside

the cable, including water treeing and general water intrusion (40% of the total responses); “Manufacturing Defect,” which includes all failures related to defective cable components, including broken conductor wires, voids in the insulation, and jacket damage [12] (17% of the total responses); and “Human Error,” which includes any failure that involves human interaction, including improper cable installation and maintenance (11% of the total responses). Seeing that the “Water/Moisture” category makes up the majority of reported cable failures, it is therefore worthwhile to further explore degradation mechanisms of this kind and develop a better understanding of how the health of a cable is affected by extended exposure to water.

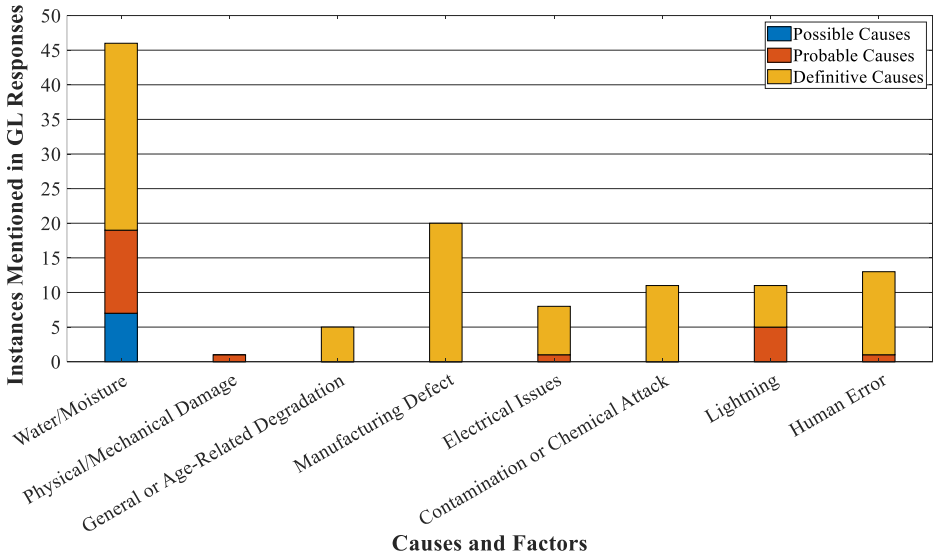

Figure 6. Categories of cable failures and number of responses [13].

1.3 Overview of Insulation Treeing

Insulation treeing is an umbrella term encompassing pre-breakdown phenomena associated with MV cable failure due to degraded insulation [14]. The word “treeing” comes from the tree-like structure and outward growth pattern typically associated with

this degradation mechanism. The formation of an insulation tree almost always occurs at defective points inside the cable insulation where the material is degraded or contains some defect such as a void or protrusion [14]. Insulation trees are usually not found in LV cables because the electric field inside cables of this type is not intense enough for tree formation. The average electric field for tree formation must be at least 2.8 kV mm^{-1} which is much greater than the 0.6 kV mm^{-1} electric field typically found in LV cables [15]. Similarly, insulation trees are usually not found in HV cables because they are manufactured to such a high standard due to their voltage rating, which eliminates most defects in the material. With little to no defects present in the material, the chance of an insulation tree forming and actually damaging an HV cable is not as significant as that for MV cables.

Insulation treeing can be broken down into three types depending on the solution and formation method of the tree: water treeing, electrical treeing, and electrochemical treeing. Water trees always occur in the presence of an electrically charged solution inside the insulation material whereas electrical trees can form with or without the presence of a solution. It is also possible for a water tree to evolve into an electrical tree, but typically not the other way around. Electrochemical treeing is commonly used interchangeably with water treeing in literature but is always defined as an insulation tree composed of an electrically charged solution containing ions from a particular salt. For the purpose of this thesis, all insulation trees containing an electrically charged solution with salt ions, such as aqueous copper sulfate ($CuSO_4$), will be classified as water trees.

The tree-like appearance typically associated with insulation trees is not entirely unusual. In fact, these tree-like structures were first noticed in 1777 by Georg Christoph Lichtenberg who was studying branching discharge patterns on dielectric materials. Because of Lichtenberg's work, branching discharge patterns (known today as Lichtenberg figures, shown in Figure 7) are known to occur inside certain solids, liquids, and gases during dielectric breakdown. Additionally, there are naturally occurring Lichtenberg figures like lightning, also shown in Figure 7, that develop tree-like structures similar to those of insulation trees.

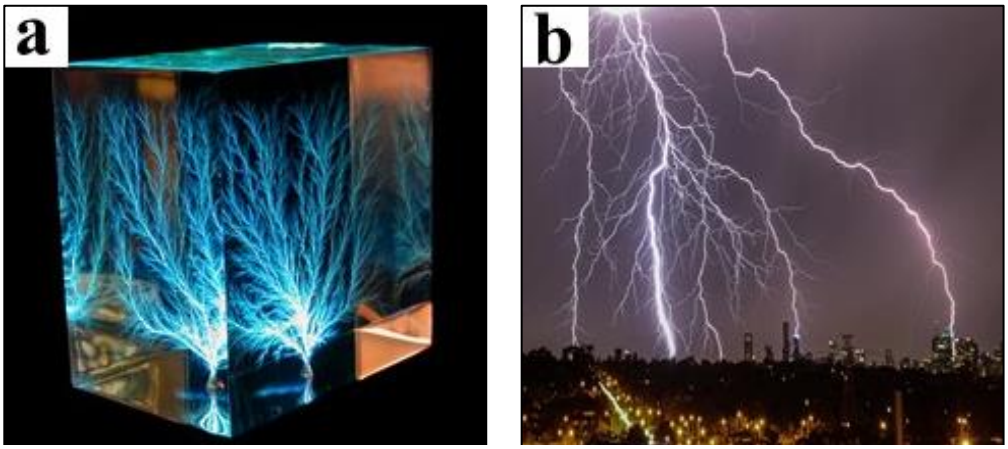

Figure 7. (a) Lichtenberg figure encased in a block of clear acrylic [16]; (b) lightning strike with tree pattern [17].

The first reported occurrence of insulation treeing in cables was in the mid-1930s when previously failed paper insulation was examined, and a tree-like structure was observed inside [18]. Shortly after this observation, polyethylene (PE) began to take a more prominent role as the premier insulation material for underground cables because of its strong dielectric properties, long lifetime, and low cost [14]. These favorable features created the illusion that PE-insulated cables would last for a significant amount of time under most conditions, and were essentially immune from insulation-related failures. This

illusion was shattered in 1971 by Vahlstrom and Lawson who discovered several recently failed PE-insulated underground cables that were all affected to some extent by insulation treeing. Although it was suspected that insulation treeing was not the direct cause of failure, the discovery was significant enough to warrant an expansion of research into the reason why insulation trees form inside a cable's insulation in the first place.

1.3.1 Water Treeing

Of the three insulation tree types, water trees are the most prominent and are considered to be the primary degradation mechanism for underground MV cables [19]. In the absence of other degradation stressors, water treeing does not directly cause failure in a cable. It is even possible for a water tree to completely bridge the insulation from the insulation shield to the inner conductor and still not cause a failure [19]. Instead, water treeing has the function of weakening the dielectric strength of the insulation material over time which can eventually lead to a dielectric breakdown in the form of localized PDs in the material [19]. Additionally, there exists the possibility that a water tree will transform into an electrical tree which may directly lead to cable failure.

The physical geometry of a water tree can be defined as a collection of micro-sized cylindrical pathways connected to form a single structure [20]. These pathways, also known as branches, vary in size and shape but typically have diameters in the range of 5 to 300 micrometers [20]. The geometry of a particular water tree varies depending on the type of tree it is, which is related to its structure and growth pattern. The three primary water tree types are bow-tie, vented, and bush, all shown in Figure 8. Each water tree type typically develops in areas of defective insulation containing voids or

protrusions but possess differing growth patterns. A bow-tie water tree, aptly named for its resemblance to the necktie of the same name, will grow in two separate directions. Vented water trees only grow in a single direction and are believed to be the predominant water tree type leading to eventual breakdown of the insulation [21]. A bush water tree is defined as a collection of vented water trees possessing the same growth pattern as that of the tree type it is composed of [21]. Additionally, bow-tie water trees can form at any point inside the insulation whereas vented and bush water trees usually initiate at the interface of the insulation and insulation or conductor shield components.

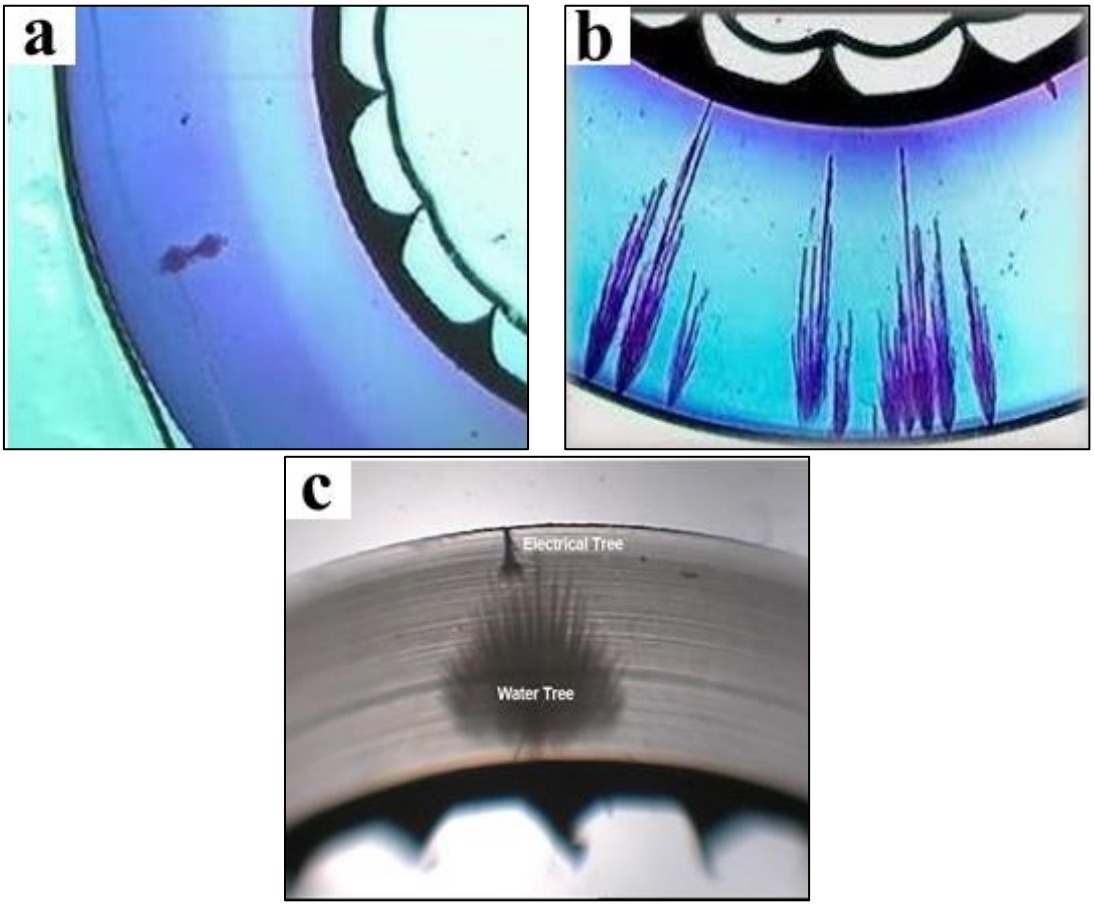

Figure 8. (a) Bow-tie water tree [22]; (b) vented water trees [23]; (c) bush water tree [24].

Water tree formation and growth requires the presence of both an electrically charged solution and a significantly intense electric field in the cable's insulation. The required electric field intensity is approximately 2.8 kV mm^{-1}, which is a value much less than that required for electrical tree formation. In addition, a void or protrusion must be present for water tree formation to occur. There are two prevailing theories as to the specific process of water tree formation and its subsequent growth through the insulation. The first theory states that water trees form due to radical creation in areas of insulation containing voids or protrusions because of water dissociation [25,26]. The radicals react with the insulation material thus forming polymer radicals through chain scission [25,26], with oxidation also being a potential contributor. The broken chains reconnect with nearby chains which expands the initial void or protrusion into the beginning structure of a water tree [25,26]. The cable's applied electric field creates mechanical stress on nearby polar chains resulting in segmented motion and the creation of extra volume in the insulation [25,26]. The extra volume allows for new oxidation sites to appear and provides additional transportation routes for water molecules [25,26]. Similar to the first theory, the second theory of water tree formation and growth also states that water trees form due to the expansion of voids or protrusions in the insulation, but instead of radical creation through water dissociation, the process occurs because of mechanical forces created by the cable's electric field [25,27]. After water tree formation, continued growth occurs through the merger of several voids or protrusions which are each filled with an electrically charged solution and thus are partially conductive [25,27]. The effect of being

partially conductive results in an intensified electric field at the pole of the water tree, which promotes inward growth toward the cable's conductor component [25,27].

1.3.2 Electrical Treeing

Electrical treeing, an example of which is shown in Figure 8 along with a bush water tree, can occur in both alternating current (AC) and direct current (DC) systems, and either with or absent a water tree. Unlike the water treeing phenomenon, the presence of electrical trees in cable insulation has the possibility of directly causing failure due to insulation breakdown [28]. The probability of electrical tree formation and time to breakdown are a function of several factors including magnitude and frequency of the applied voltage, electrode geometry, temperature of the cable [29], as well as the presence of anti-treeing chemicals inside the insulation. Electrical trees typically form in areas of insulation defects such as voids, protrusions, and imperfections, or may develop directly from a water tree already present in the insulation [30]. The factors that influence the transformation of a water tree to an electrical tree include the size of the water tree [31], the level of degradation currently presented by the water tree structure [32,33], the magnitude and frequency of the applied voltage [34], and the temperature of the cable [35]. Whether formed in the area of an insulation defect or from the transformation of a water tree, the shape of an electrical tree is highly dependent on the intensity of the electric field present in the area where the tree is formed. High intensity electric fields produce electrical trees with a somewhat bushy shape whereas low intensity electric fields produce electrical trees containing branch-like structures [25].

The lifecycle of an electrical tree is composed of three primary phases: formation, growth, and breakdown of the cable insulation. As with water trees, electrical trees typically start in areas of high electrical stress such as voids or protrusions in the insulation. Because the formation phase requires a significantly intense electric field (approximately 100 kV mm^{-1} for PE), electrical tree formation usually occurs in one of the previously mentioned defect areas [36]. These defect areas may exhibit an electric field intensity far greater than that found in other areas of the insulation, making them ideal locations for electrical tree formation. A significantly intense electric field in these defect areas leads to electron emission and the subsequent injection of electrons into the insulation [36]. This results in the accumulation of space charge which is then preserved in the defect areas as a heterocharge [36]. The buildup of heterocharge in the defect areas causes an additional increase in the intensity of the electric field which leads to localized degradation of the insulation material and the formation of an electrical tree [36]. Following the formation phase is the continued growth of the electrical tree because of a stream of electrons that result in the creation of the first channel of the tree [36]. In addition to injection, electrons are also removed from the insulation causing a phenomenon known as an electron avalanche [36]. An electron avalanche is a process where free electrons in the presence of an electric field accelerate and subsequently collide with other nearby atoms, thereby ionizing them and releasing additional electrons which furthers the growth process [37]. In cable insulation, this allows for randomized electrical tree growth in all directions and the formation of additional tree channels starting from the first channel [36]. The subsequently formed tree channels have a higher

than normal inner gas pressure which is known to reduce the magnitude of an electron avalanche [36]. This provides for a reduction in growth of the electrical tree with this effect being more profound in trees with a bushy shape than those consisting of branch-like structures [36]. Lastly, after a certain degree of growth has occurred, the electrical tree will rapidly produce a complete breakdown in the insulation and the cable will be short circuited.

1.4 Current Methods for Evaluating Cable Degradation

Several methods exist for evaluating electric cable degradation as well as predicting the remaining life of those cables currently in operation. They range from those that are nondestructive and allow for continued cable operation, to those that are potentially destructive and require the cable to be taken offline. The following test methods are discussed in this section: visual inspection, thermal infrared imaging, voltage withstand testing, leakage current testing, partial discharge testing, time domain reflectometry, polarization and depolarization current testing, and dissipation factor testing.

1.4.1 Visual Inspection

The simplest and most cost-effective method for evaluating the condition and health of a cable is visual inspection. This method makes use of a qualified visual inspector who checks both the cable itself and its surrounding environment for signs of damage, contamination, or the presence of environmental stressors like temperature or moisture [38]. The inspector is mainly looking for changes in color, crack propagation, and evidence of cable surface changes such as contamination in the form of water,

chemicals, or dirt [38]. Most of the information gathered through visual inspection is qualitative, but some defects like crack width and depth can be tracked over time to reveal the crack's rate and direction of growth [38]. The visual inspection is typically done by the naked eye of the inspector, but can be assisted using items like a camera, flashlight, or magnifying glass.

One major challenge with visual inspection is that the cable must be easily accessible by the inspector, which is difficult when cables are located underground as is typical of MV cables in NPPs. With the assistance of a device called an illuminated borescope, these cables can be inspected below ground without having to disrupt their placement [38]. This device allows the inspector to see into underground areas like concrete ducts or electrical conduits where cables are present. Additionally, this device has the capability to record pictures or videos of what it is viewing, which is very helpful when documenting cable degradation over time [38].

1.4.2 Thermal Infrared Imaging

Thermal infrared imaging (TIRI) is a nondestructive test commonly found in many industries and is used to create a heat map of a particular object or person [39]. TIRI is also frequently used in conjunction with other test methods to detect degradation in electrical systems including cables. Although TIRI cannot quantitatively measure the dielectric properties of a cable, it provides useful information regarding the cable's health by identifying areas with unusually high resistivity or surface temperature [40]. Because an ideal cable operating in a homogeneous environment will radiate heat uniformly and in a predictable fashion, any deviations from uniformity, like unusually high resistivity or

surface temperature, are causes for concern as they are typically indicative of localized dielectric losses [38,40].

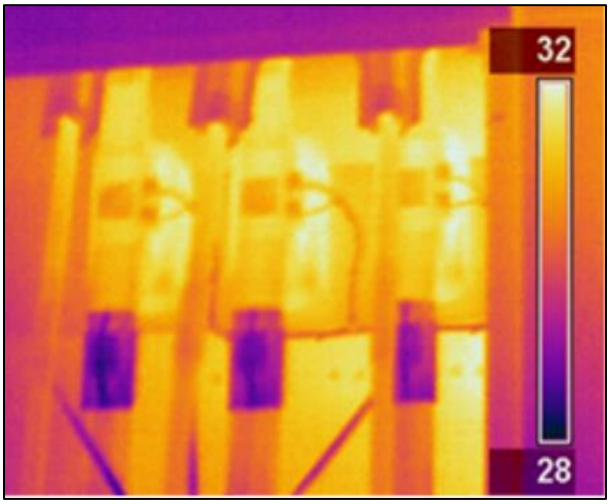

Figure 9. Thermal scan of a 13.8 kV cable with a temperature spread of 28 to 32°C [41].

There are two primary issues with using TIRI testing for underground MV cables. The first issue is that the cables must be accessible by the operator, which as previously noted is difficult with underground MV cables that are enclosed in concrete ducts or electrical conduits. Recent literature has yielded potential resolutions to this issue; instead of measuring the temperature of the cable directly, the temperature of the structure the cable is located in or that of the surrounding soil can be measured, and the cable's temperature can be inferred based off these measurements [42,43]. The second issue is that it may not be possible to detect water-related degradation such as water treeing, which as Figure 6 shows, is the most prominent factor leading to cable failure [38]. Two potential resolutions for this were proposed in a 2015 report by Sandia National Laboratories. First, instead of directly looking for water tree degradation in the cable insulation, the cable jacket could be examined for water ingress using an applied

temperature gradient and TIRI [38]. If water is present in the jacket, that may indicate that water is also present in the insulation. At the very least, further testing of the cable should be performed to confirm or deny that possibility. Second, testing at high frequencies such as those above 800 Hz could intensify dielectric losses in the cable more so than those at low frequencies, which would result in temperature deviations that could be detected by a TIRI tester [38]. The locations of these temperature deviations would then be interpreted as areas where water tree degradation may be occurring.

1.4.3 Voltage Withstand

Voltage withstand testing is considered the most straightforward method for detecting cable degradation, but has disadvantages of being potentially destructive both in the short and long term, and requiring that the cable be taken offline while testing occurs [40,44]. During the test, a voltage that is around two or three times greater than the cable's usual operating voltage, U_0, is applied for a finite amount of time [7,38]. This leads to the formation of an electric field far more intense than the field experienced by the cable during normal operation. If the resulting electric field strength surpasses the breakdown strength at any point inside the cable insulation, a breakdown will occur at that specific point and the test is thereby destructive. Generally, the specific section of insulation where the breakdown occurred can be located, repaired, and retested to confirm that it meets the requirements of the withstand test [40]. In the case that additional breakdowns occur after repairing and retesting the insulation, it is advised that the entire segment of insulation be replaced before bringing the cable back online [44].

The majority of voltage withstand testing occurs using one of three voltage types: DC, AC, and AC very low frequency (VLF) [7,38,40,44]. DC withstand testing has historically been the industry-preferred test type, but has since fallen out of favor after it was shown to have certain issues [38,40,44]. The test results have shown no correlation with the presence of insulation trees or defects, and it has been determined that high DC voltage can accelerate degradation in XLPE insulation because of the accumulation of space charges [7,38,40,44]. Although this accumulation does not occur in rubber-based insulations like EPR, the prevalence of XLPE insulation in cables connected to electric distribution systems makes this concern justified [7]. AC voltage withstand testing has the advantage of stressing the cable insulation in the same fashion as during operation, making it the preferred test type [7]. The test occurs in the frequency range of 20 to 300 Hz, making it an ideal test type for a wide array of cable systems [40]. Additionally, the polarity of AC voltage is reversed after every half cycle unlike DC voltage, which prevents the accumulation of space charges in the insulation that could potentially cause premature failure [7,38,40,44]. VLF voltage withstand testing operates in the frequency range of 0.01 to 1 Hz and can be used to test all categories of cable insulation [40]. Advantages of VLF include ease of mobility because of the relatively small size of the testing equipment, and the ability to generate faster growth for some defects compared to that of normal operating frequencies [40]. As with standard AC testing, VLF voltage withstand testing uses an alternating polarity which prevents the build-up of space charges and stresses the insulation in a similar way as during normal cable operation [7].

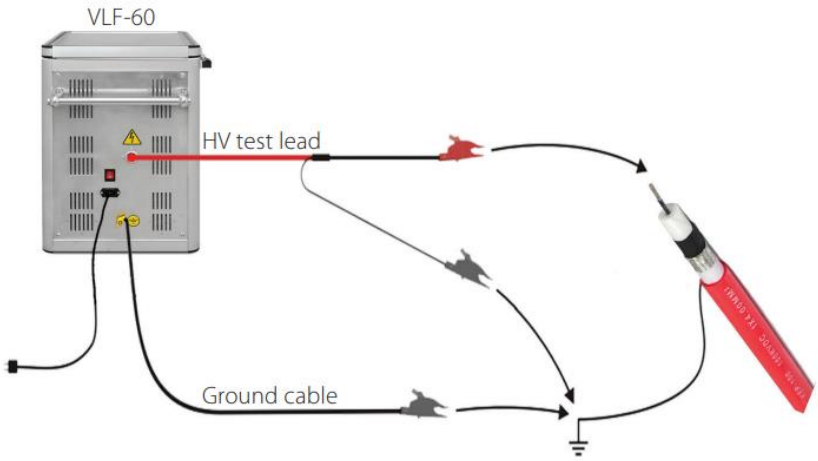

Figure 10. Setup for VLF voltage withstand testing [45].

1.4.4 Leakage Current

Considered to be one of the simplest and most cost-effective methods for testing cables in operation, leakage current testing is useful in determining the extent to which a cable has been degraded by quantifying the electrical resistance of the insulation. A DC voltage lower than what is normally used in withstand testing is applied in a stepwise manner to an offline cable, and the leakage current flowing through the insulation is measured over a period of approximately ten minutes. The leakage current is heavily dependent on a variety of cable parameters and conditions, including cable size, operating temperature, water ingress, and level of oxidation. Knowing both the applied voltage and leakage current inside the insulation, the resistance can be calculated and compared to that of a healthy cable. A lower resistance through the insulation is correlated with a higher leakage current, and is indicative of the presence of moisture or a conductive contaminant inside a defect or void. Because the test results are highly sensitive to various environmental factors, which tend to be quite variable, it is difficult to document

degradation over time. This leads to the test generally being classified as pass or fail depending on the calculated resistance. The variable nature of the test gives rise to the possibility that a healthy cable could be classified as a fail, or vice versa, depending on the present conditions of the cable's environment.

1.4.5 Partial Discharge

PD testing originated in the 1970s and has been used ever since to test cable insulation for defects and degradation related to environmental and operational conditions, manufacturing, and damage caused during installation [38,40]. PD testing begins in the following way: starting from zero, voltage is applied to a cable and inevitably spreads to defective areas in the insulation. As the voltage continues to increase, a PD occurs, which is where the defective areas conduct, and voltage is distributed to the surrounding insulation [7]. A single PD occurrence usually does not have a considerable effect on the health of a cable, but multiple PDs over the course of months and years can potentially lead to a failure.

PD testing can be performed with the cable either online or offline, with the former using a voltage of U_0 and the latter using a voltage higher than U_0 [40]. Online PD testing is advantageous because the cable does not have to be taken out of operation to perform the test, which alleviates downtime and the extra cost associated with it. One disadvantage of online PD testing is that by using U_0 as the test voltage, there is no chance of initiating a PD in defects that require a voltage higher than U_0. This disadvantage is mended with offline PD testing, which can cause initiation of defects normally not present during online PD testing conditions. Disadvantages of offline PD

testing include having to take the cable offline to perform the test and causing defects to activate that could have been indefinitely inert in normal operating conditions.

PD testing is considered to be a stochastic process because the test results are highly dependent on several factors, including insulation type, testing voltage, temperature, and defect geometry and location [7,40]. Consequently, the test results are highly variable and occasionally produce inaccurate conclusions. The absence of a PD does not necessarily rule out the presence of a defect in the cable; in fact, it is quite possible that a defect is present but does not have the specific characteristics required to initiate a PD. This is especially true in the case of water tree defects, which may not possess the required magnitude of electrical stress for a PD to occur [7].

1.4.6 Time Domain Reflectometry

Time domain reflectometry (TDR) is a method commonly used to detect degradation in both overhead and underground cables. This method can also be used to determine the total length of a cable in operation [46]. TDR works in the same manner as a radar system, relying on reflected signals to determine points of interest inside a cable. The points of interest, in this case being defects or faults, are found by determining the locations of the reflected signals which correspond to areas where the cable's electrical impedance is distorted. The TDR test starts in the following manner: an energy pulse in the form of a voltage is applied to the cable, which creates a wave that propagates along the length of the cable being tested. If the cable is healthy, it will have a uniform electrical impedance throughout; if the cable is degraded, there will be a distortion in the electrical impedance, which will cause the wave to reflect to its starting position. The

energy pulse is reflected when it reaches one of the following: the end of the cable, a defect inside the cable, or the location of some other fault that causes a distortion of the cable's electrical impedance. If an electrical impedance distortion is found within the cable, the travel time of the wave to and from said distortion can be converted to a distance, which is used to determine the location of a defect or fault accurate to within one foot.

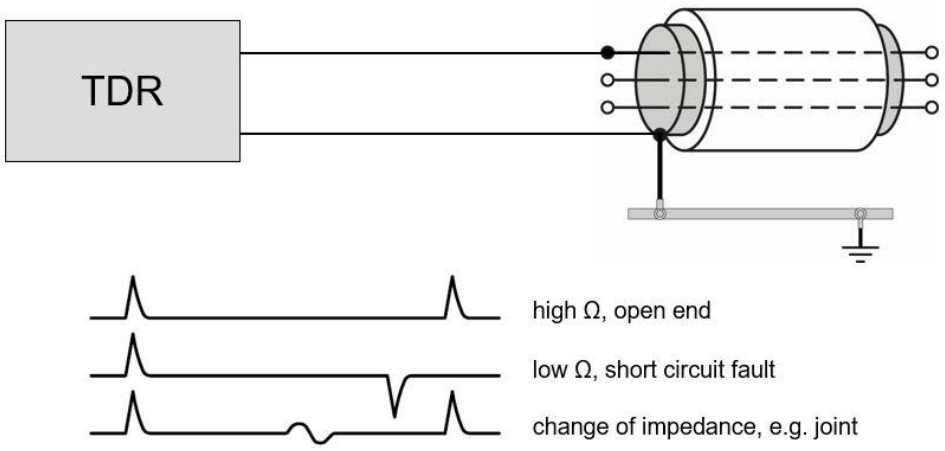

Figure 11. Setup for TDR testing with electrical impedance characteristics [46].

1.4.7 Polarization-Depolarization Current

Polarization-depolarization current (PDC) testing is another nondestructive method used to assess cable health by evaluating the moisture content and electrical conductivity of the cable's insulation [47]. Ever since its introduction in the 1990s, PDC testing has been widely popular in the field of cable testing because of its simplicity and swiftness in gathering measurements [40,47]. PDC testing starts with the application of a relatively low DC voltage (as low as 30 V) to an offline cable for a predetermined amount of time. The polarization current, which is the charging current that flows

through the cable as the voltage is applied, is measured and recorded during this time. After the polarization current is measured, the cable is intentionally short circuited for a brief period of time to discharge the capacitive current flowing in the cable. The discharging capacitive current, known as the depolarization current, is also measured and recorded under a short circuit circumstance for a period of time equivalent to that of the polarization current measurement. The measured currents are then assessed and compared to those of known healthy cables to determine if the tested cable has degraded. Common analysis techniques include comparing the polarization current per unit length of aged and new cables, and comparing the depolarization currents at different voltages to verify the current changes at the same rate as the voltage [40].

Although convenient for its simplicity and ease of use, PDC testing does have its disadvantages. Because small currents are affected by environmental conditions [40], they may not be entirely accurate when measured which could lead to an incorrect assessment of the cable's health. PDC testing requires a longer cable length than other test methods to generate a sufficiently large enough signal to measure [40]. To generate a sufficient polarization, the cable must be energized prior to measuring the currents, and be completely discharged after testing has concluded [40]. Considering these disadvantages, it may be prudent to use PDC testing in conjunction with other cable testing methods to develop a more accurate and authentic assessment of a cable's health.

1.4.8 Dissipation Factor

Dissipation factor, also known as tan delta, is a parameter commonly correlated to a materials' ability to hold in energy, or in other words, to act as an insulator [48]. The

dissipation factor at a given voltage and frequency is defined as the ratio of the resistive and capacitive currents emanating from the cable, which is equivalent to the tangent of the dielectric loss angle [40,48]. Generally, a low dissipation factor is indicative of healthy insulation material that can efficiently store energy, whereas a high dissipation factor indicates an aged cable that is inefficient in storing energy [48]. The value of a cable's dissipation factor is influenced by a variety of environmental factors, including temperature, humidity, water ingress, and ultraviolet light [48]. The results of dissipation factor testing are most effectively analyzed when compared over a period of time or at different voltages [40]. Because dissipation factor tends to increase as the cable ages and starts to degrade, it is possible to predict the rate of aging by determining the change in dissipation factor over time or at different voltages.

Testing for dissipation factor occurs when the cable is offline using an applied AC voltage at a frequency typically in the range of 0.1 to 300 Hz [40]. Unlike voltage withstand or PD testing, dissipation factor testing can be performed at voltages lower than U_0 while still obtaining valuable results. The ability to test at voltages lower than U_0 is one advantage of dissipation factor testing because it prevents inadvertent cable aging caused by testing with voltages of U_0 or higher. Because dissipation factor is a function of the AC voltage frequency [40], its value will vary depending on the frequency used for the test. For this reason, it is difficult to create a standard criterion for correlating dissipation factor to cable health. In addition, values of dissipation factor depend on the formula of the insulation material being tested which varies based on the presence of different filler materials. This makes EPR materials difficult to analyze because of the

wide range of filler materials used in the different EPR formulas, with each possessing a different loss behavior [40].

1.5 Simulation of Cable Degradation

Another tool capable of evaluating degradation in cables is finite-element analysis (FEA). Instead of physically testing a cable currently in operation, which can be expensive, time-consuming, and result in plant downtime, FEA can be utilized to model the physical cable and predict the effect of common environmental stressors such as temperature, radiation, and water ingress on the health and operability of the cable. In situations where an operational cable cannot be easily accessed or would be burdensome to take offline, FEA results, such as those presented in this thesis, can fill the void by providing an initial assessment of the cable's health. This initial assessment, albeit limited in accuracy, can then be interpreted by cable degradation testers to determine if a more thorough test, such as those discussed in the previous section, is required.

In addition to producing quick results with little to no cost beyond the initial purchase of software, FEA has the capability to simulate a wide variety of specific conditions and scenarios that may eventually present themselves in physical cables. The effects of these conditions and scenarios may be unknown to physical cables tests, but not to the extremely versatile realm of FEA where they can easily be simulated and better understood. The advantages of FEA, as well as the plethora of data and information that can be collected through its use, provide a motivation for its further use in conjunction with physical cable tests to provide a more comprehensive understanding of cable

degradation. The final result of such a combination will inevitably be improved outcomes in the long run for cable testers and operators of NPPs.

1.6 Thesis Objectives

This thesis has six primary objectives which were developed after reviewing literature relevant to the water treeing phenomenon. The objectives are as follows:

- Develop a better understanding of water tree degradation in EPR-insulated MV cables.
- Determine the influence of water tree geometry on the rate of cable degradation.
- Compare rates of water tree degradation using pure distilled water (H_2O) and $CuSO_4$ compositions.
- Examine the degradation effects of changing temperature and cable operating frequency in the presence of water treeing.
- Predict a range of values from common cable and water tree parameters that result in permanent cable degradation.
- Provide an argument for further use of FEA in conjunction with physical cable testing.

1.7 Thesis Summary

Chapter One provided a background on electric cables and cable degradation, a discussion regarding the formation, growth, and types of insulation trees, a thorough overview of the most prominent physical cable degradation testing methods, a brief introduction to the advantages of using FEA to simulate cable degradation, and the objectives of this thesis.

Chapter Two serves as a brief review of literature relevant to this thesis. The areas of focus include the simulation of electric cable degradation, the various water tree geometries used in previous simulation work, the role of ionic solutions in cable degradation, a brief overview of experimental testing of water tree degradation, and the temperature and frequency dependency of a cable's electrical properties.

Chapter Three details the preliminary simulation work done for this thesis including the FEA software that was used and the various models that were created. Additionally, the validation and verification process used for the preliminary simulations is described, including comparison to known analytical solutions, related literature, as well as direct comparison between the two software that were used.

Chapter Four describes the updated cable model used for the primary simulation work of this thesis. The materials and dimensions of the model are provided along with a discussion of mesh refinement and convergence. Additionally, the simulation methodology, setup for the parametric study, and rationale regarding the parameters and values used in the study are provided.

Chapter Five provides the results of the parametric study along with an interpretive discussion and analysis of the key findings. Additionally, a brief discussion comparing the results to physical cable tests is provided at the end.

Chapter Six presents the conclusions of this thesis and a discussion regarding their relevance to the electric cable testing industry. Suggestions for future research in this area are also provided.

CHAPTER TWO:
REVIEW OF RELEVANT LITERATURE

2.1 Summary of Literature Review

A thorough search of literature relevant to this thesis was conducted to determine the current status of the subject. The following areas provided the focus of the literature search: simulation of cable degradation using FEA, different water tree geometries used in the simulation literature, the effect of ionic solutions on cable degradation, experimental testing of water tree degradation in cables, and the effects of temperature and frequency on the rate of cable degradation. Various shortcomings and problems with the existing literature are discussed, and the motivation for this thesis is provided at the end of the chapter.

2.2 Simulation of Electric Cable Degradation

There have been many studies conducted in the area of simulating electric cable degradation using FEA. Typically, either Ansys Electronics Desktop (Ansys) or COMSOL Multiphysics (COMSOL) FEA software have been used because of their significant capabilities in solving complex electromagnetic problems. In addition, each software possesses built-in solid modeling features which have been used extensively in the literature for designing the electric cable models being simulated. These cable models have tended to be in the two-dimensional (2D) geometrical configuration because of the simplicity in using a 2D model rather than a three-dimensional (3D) model.

Most of the existing literature has focused on the following areas of degradation in the cable's insulation component: mechanical, thermal, and electrical. Wang et al. used

COMSOL to simulate a XLPE-insulated cable model with the goal of studying the effect of changing the ratio of height to width of an elliptical water tree on the electric field strength and stress caused by a dielectrophoretic force at the water tree poles [49]. They found that as the height to width ratio increases, causing the water tree to narrow, so does the electric field strength and stress at the water tree poles. Khouildi et al. used COMSOL to study the effect of internal insulation cavities containing air or water on the temperature distribution of a XLPE-insulated cable at various operating temperatures [50]. They found that the internal insulation cavities resulted in further degradation and aging as the operating temperature increased. Xia et al. also looked at the temperature distribution of a cable containing various water cavities scattered around the insulation material, finding that the temperature inside and around the cavities was lower compared to the temperature in areas of healthy insulation [51]. It should be noted that this result is not consistent with what is found in this thesis, which is that the temperature inside and around an insulation cavity is higher than that of the surrounding insulation.

Electrical degradation, specifically degradation of the insulation material's electrical properties, has been the primary area of focus for cable degradation researchers using simulation software. Chen et al. simulated water tree degradation in a XLPE-insulated cable using COMSOL to determine the effect of increasing water tree depth on the capacitance of the cable [20]. They found that capacitance increases with water tree depth, which validated the mathematical model they proposed in the study. Burkes et al. did a similar study using an XLPE-insulated cable and found the same relationship between capacitance and water tree depth [52]. They also determined that a cable's

resistance is relatively constant up until the water tree impacts the conductor which results in a significant decrease in the value of the resistance. Alsharif et al. [53] and Liu et al. [54] both used FEA to observe a cable's voltage and electric field distribution in the presence of an insulation defect. Both studies found that the presence of a defect inside the insulation works to distort the voltage and electric field distribution, but only in the area around the defect, which was confirmed in a similar study conducted by Sandia National Laboratories [38]. Promvichai et al. indirectly built upon this result by determining that the electric field around a defective area such as a water tree is intensified with an increasing intensity observed as the water tree grows closer to the conductor [55]. Kachi et al. [56] and Jin-feng et al. [57] provided further insight in this area by using FEA to determine how the electric field intensity is affected by the size and geometry of the water tree region.

2.3 Water Tree Structure and Simulation Geometry

The structure of a physical water tree is known to be random and complex. As with electrical trees, a water tree's structure is highly dependent on a variety of factors including the cable's electric field intensity, operating frequency, the content of the composition inside the water tree region, and the specific water tree type based on its growth pattern [21]. Even if these factors are known, there exists other factors and considerations that make predicting the exact structure of the corresponding water tree next to impossible. As a result, there exists no standard definition for the structure of a water tree thus making it difficult to declare definitive conclusions regarding water tree degradation in cables. For this reason, water tree modeling with FEA has generally relied

on the approach of using a simple geometry such as an ellipsoid or a cylindrical region to represent the entire area that a physical water tree occupies. Although not physically accurate, these simple geometries are sufficient to generate approximate relationships between water tree growth and degradation of a cable's electrical properties.

In the current literature related to the simulation of water tree degradation, an ellipsoid geometry has predominantly been used to represent the region of a water tree. Famakin and Kim extensively discussed considerations related to water tree modeling using FEA and argued that the structure of a water tree is best represented by an ellipsoid [21]. This argument is tested in studies by Burkes et al. [52] and Chen et al. [20] who both used a 2D ellipsoid geometry to represent the structure of a vented water tree in their simulations. Their rationale for using an ellipsoid geometry was based on experimental work by Maeda et al. who showed that water trees exhibited a spherical shape under the standard operating frequency of 60 Hz (50 Hz for European countries) [58], as well as the assumption that water trees grow longer and narrower as they approach the cable's conductor. Similarly, Wang et al. used a 3D ellipsoid geometry to represent an insulation defect, showing that the same conclusions regarding insulation degradation could be drawn [49]. Although an ellipsoid geometry has been used in many studies, others have attempted to model the structure of a physical water tree more accurately by using complex geometrical shapes. Khouildi et al. made used of one or more circular sectors along with the outlines of two physical water trees to create their water tree models [50]. Using a similar approach, Jin-feng et al. used a combination geometry consisting of conical and spherical shapes connected together to form their water tree model [57].

2.4 Ionic Solutions and Electric Cable Degradation

Electric cables are buried in a wide array of environments that contain many different chemical components. As a result, it is quite common to find water tree regions inside cable insulation composed of a mixture of water and soluble salts like sulfates, nitrates, and chlorides. These mixtures, known as ionic solutions, contain positively and negatively charged ions known as cations and anions, respectively, which are not found in pure distilled water (H_2O). The presence of these charged ions is hypothesized to result in an accelerated rate of water tree degradation either because of reactions between the insulation material and the ions, or intercalation of the ions further into the material which facilitates the flow of electrical current.

Various studies have been conducted to better understand the effect of ionic solutions on electric cable degradation. Promvichai et al., referenced previously in the preceding section, used FEA to evaluate electric field intensity around a water tree region for various ionic solutions including $CuSO_4$, iron sulfate, and sodium chloride [55]. Of the simulated ionic solutions, they found that $CuSO_4$ provided the greatest electric field intensity and contributed the most to a water tree's growth. Another study by Promvichai et al. provided additional insight into this result, hypothesizing that $CuSO_4$ is effective in accelerating water tree growth because of its high pH and electrical conductivity [59]. The effect of cations and anions present in ionic solutions was investigated by Qureshi et al. [60], and Boonraksa and Marungsri [61], with each study concluding that both ion types have an impact on the growth of water trees in XLPE insulation. Further research by Huimin et al. examined if water tree growth is affected by an ionic solution's molar

concentration by developing and validating a model that describes ion-to-ion interactions in a solution [62]. They found that ion-to-ion interactions using a concentration of 0.1 M have a strong impact on water tree growth, but results were inconclusive using a concentration of 0.5 M.

2.5 Experimental Testing of Water Tree Degradation

There exists an expansive amount of literature related to experimental testing of water tree degradation in physical electric cables. Because the focus of this thesis is the degradation of the cable's insulation component (specifically, degradation of the insulation's electrical properties), literature relevant to that issue is discussed in this section.

In a study conducted by Al-Arainy et al., water trees were artificially created inside XLPE insulation using accelerated aging techniques including temperature cycling [63]. The goal of this study was to determine the effect of temperature on the distribution of water trees and their corresponding lengths. It was discovered that although less water trees were produced in the insulation when subjected to temperature cycling, the water tree length was on average greater than that of water trees produced in a room temperature setting. This proved that individual water tree growth is accelerated at higher and prolonged temperatures, thus creating a higher probability of permanent insulation degradation. In a similar study, Mauseth et al. created artificial water trees in XLPE insulation to determine the relationship between water tree length and accelerated ageing time [64]. As was predicted, water tree length increased as time progressed with permanent degradation of the insulation material occurring after three weeks of testing.

Another similar study by Radu et al. used artificially created water trees in XLPE insulation to show that both the relative permittivity and electric field intensity around the water tree region are time-dependent with each property increasing throughout the period of water tree growth [65]. Additional studies by Bulinksi et al. [66] and Garton et al. [67], also using XLPE insulation, provided evidence that the breakdown strength of the insulation material decreases as accelerated aging progresses, with the decrease being more profound at higher frequencies.

2.6 Effect of Temperature on Electric Cable Degradation

It is widely known that temperature has a significant effect on electric cable degradation. As previously referenced, Khouildi et al. studied the effect of cable operating temperature on XLPE insulation using COMSOL [50]. In addition to the simulation work, they also experimented with a physical cable heated to temperatures of 100 and 120°C for a set period of time. From the experimental work, they found that PD activity in the cable increased after heating, thus confirming their initial hypothesis, and validating the simulation work. In another study, Lei et al. studied the effect of cable operating temperature on EPR insulation using experimental tests [68]. Using artificially created spherical insulation cavities and temperatures ranging from 25 to 200°C, the breakdown strength and PD activity of the EPR insulation was evaluated. They found that breakdown strength decreased, and PD activity increased along with temperature, both indications of an accelerated rate of degradation. The decrease in EPR breakdown strength with increasing temperature was also discovered in work done by Duckworth et al. using harvested EPR-insulated cables from an actual NPP [69]. In addition,

Duckworth et al. showed that time to insulation failure decreases with increasing temperature, which is also shown in the work of Cao and Grzybowski [70], also using an EPR-insulated cable.

2.7 Effect of Frequency on Electric Cable Degradation

As with temperature, the operating frequency of an electric cable will influence the cable's degradation. As noted in ASTM D149 [71], frequencies above 800 Hz have the potential to cause heating of the dielectric material because of molecular dipole rotation [72]. The consequence of dielectric heating is an accelerated rate of degradation which further synergistically increases the rate of cable failure. In addition, it is known that a cable's electrical properties are affected by changes in frequency. To better understand this effect, many studies have been conducted to qualitatively determine the relationship between frequency and various electrical properties of insulation materials including relative permittivity, dissipation factor, and electrical conductivity. Two studies by Lei et al. did just this for EPR in the frequency range of 0.01 Hz to 1 MHz [68,73]. Both studies noted the following observations regarding the material properties of EPR: relative permittivity decreases continually in the frequency range of 0.01 to approximately 100 Hz, and is nearly constant for frequencies after this range; dissipation factor decreases continually as the frequency increases, with the decrease being more profound at higher temperatures; and electrical conductivity increases continually as the frequency increases. Another similar study by Wu et al. looked at the effect of frequency on the breakdown strength of XLPE [74]. They found that breakdown strength drastically decreased when their XLPE samples were tested under AC voltage compared to DC

voltage. AC voltage tests were conducted with operating frequencies ranging from 50 to 2500 Hz, with the result being that breakdown strength decreases with increasing operating frequency.

2.8 Shortcomings of Current Literature

Several shortcomings exist in the current literature that this thesis hopes to address. First and foremost, the vast majority of electric cable degradation work using simulation software has made use of only XLPE as the insulation material. Seeing that EPR insulation is used in approximately 79% of cables currently in service, as shown in Figure 3, it is worthwhile to further explore the effects of water tree degradation in cables of this variety.

Second, there is an insufficient understanding regarding the effect of water tree structure on the rate of cable degradation. In the simulation area specifically, existing literature has typically relied on using only a single physical water tree structure to create the geometry of the water trees used in the simulation models. Given the complexity and randomness of water tree growth, along with the study by Wang et al. that showed that the narrowing of a water tree region results in increasing electric field strength and stress values at the water tree poles, it is clear that water tree geometry has some effect on the rate of water tree degradation and is an important consideration when interpreting results obtained from simulation software.

Third, a comparison of water tree degradation using a variety of compositions including H_2O and ionic solutions like $CuSO_4$ is necessary to better understand the effect of the environment a cable is housed in. This comparison will also help to validate the

existing hypothesis in literature that water trees containing ionic solutions have an accelerated rate of degradation compared to those containing nonionic solutions like H_2O.

Fourth, the effects of temperature and frequency in the presence of water treeing in EPR-insulated MV cables is not sufficiently understood. As previously discussed, both parameters do affect the rate of degradation in both XLPE and EPR insulation under accelerating aging conditions. The effects of these parameters on the rate of water tree degradation is an area that requires additional insight to develop a better understanding of the water treeing phenomenon.

Lastly, establishing a known set of values from the parameters of temperature, frequency, water tree geometry, water tree composition, and water tree depth through the insulation that results in permanent degradation will help cable researchers and testers better predict when a cable is at risk for potential failure. It is hypothesized that each of these parameters have some effect on cable degradation, which will be tested through the work of this thesis. Providing further insight into the potential effects of these parameters, along with the other literature shortcomings, will help create a more comprehensive understanding of both the water treeing phenomenon and how it affects EPR-insulated cables in particular.

2.9 Thesis Motivation

In addition to establishing a more comprehensive understanding of the water treeing phenomenon in EPR-insulated MV cables, the motivation of this thesis is also to present an argument for further use of FEA in conjunction with physical cable testing. With FEA, a wide array of cable conditions and scenarios can be simulated with ease,

including those which may be characterized as uncommon occurrences in physical cables. Using the results of these simulations, it becomes possible to predict when a cable containing water trees will experience permanent degradation of the insulation material and is therefore at risk of failing. Additionally, it is also possible to establish a correlation between simulation and physical testing results in order to better predict the evolution of a cable's lifecycle. For example, global values of a cable's resistance obtained from simulation can be directly compared to the results obtained from the leakage current test performed on physical cables. Because leakage current testing is heavily dependent on a variety of factors including a cable's operating environment, it is difficult to track degradation of the insulation over time. This difficulty can be alleviated with the use of FEA which can speed up the degradation process to better predict how and when the in-service cable may fail. With FEA as a companion component, the results obtained from physical cable tests can be better understood and less prone to error and uncertainty.

CHAPTER THREE:
PRELIMINARY SIMULATIONS, VALIDATION, VERIFICATION

3.1 Summary of Simulation Software and Preliminary Models

As stated in Chapter Two, most of the literature related to the simulation of cable degradation as a result of water treeing makes use of either Ansys Electronics Desktop (Ansys) or COMSOL Multiphysics (COMSOL) FEA software. Both Ansys and COMSOL offer streamlined approaches to solving complex electromagnetic problems and possess a variety of features related to parametric evaluation, making them ideal for the work of this thesis. Additionally, both software packages have built-in solid modeling features, which eliminates the need for a separate software to design and build the simulation models. For these reasons, Ansys and COMSOL are used for all the simulation work in this thesis, with COMSOL being the software of choice used more extensively.

To develop proficiency with both Ansys and COMSOL, as well as electromagnetic simulation in general, a variety of elementary models were designed and simulated. These elementary models were of two different geometry types: a parallel plate capacitor and a coaxial cable. Each model was designed in both 2D and 3D geometrical configurations using either a single dielectric material or a mixed dielectric. The distinction between single and mixed dielectric materials is discussed in a subsequent section.

The choice of geometry types was related both to the simplicity of the models and the availability of straightforward analytical solutions. Additionally, the coaxial cable

geometry was selected knowing in advance that this particular geometry would be built upon and made into a more complex cable model for the primary simulation work of this thesis. Other than developing proficiency with both software packages, the objectives of these preliminary simulations were to verify the consistency of results between models and assess the capabilities of each software.

Additional preliminary simulations, including inserting a rectangular section of water or air inside the insulation material of a single dielectric model, were also performed but are not thoroughly discussed other than in Chapter 3.4.2. The goal of these simulations was to determine the effects of increasing water or air ingress on the capacitance, resistance, and voltage and electric field distribution of the cable.

3.2 Variation in Meshing Techniques

Ansys and COMSOL both utilize automatic adaptive meshing based on the geometry of the simulation model. Without any action from the user, each software can create a final mesh that meets the design requirements of the particular simulation method being used. In Ansys, the process of automatic adaptive meshing starts with the generation of an initial mesh that is used to perform the preliminary field calculations [75]. From there, the solution error of these preliminary field calculations is determined, and, if found to be greater than the default acceptable error set by the software, the mesh is refined in areas showing the largest amount of solution error [75]. The field calculations are again performed, and the process is repeated until either reaching an acceptable amount of solution error, or exceeding the default number of refinement passes [75]. In COMSOL, the process of automatic adaptive meshing starts with the

generation of a physics-controlled mesh adapted to the particular geometry being simulated. The default “Normal” mesh setting is used, which generates more mesh elements than required for maximum solution accuracy [76]. An iterative approach similar to that of Ansys where areas of high solution error are refined will then occur until reaching an acceptable amount of solution error [77].

The different default meshing techniques employed by Ansys and COMSOL are worth examining further in the context of solution accuracy. As will be discussed in a forthcoming section, the variation in default mesh generation between the software may have inadvertently led to a finer mesh being generated in COMSOL compared to that of Ansys. Consequently, it is hypothesized that the results obtained from COMSOL were more closely aligned with analytical solutions than those of Ansys because of this finer mesh. Because mesh refinement was not a critical component or goal of the preliminary simulations discussed in this chapter, the default mesh settings were left unchanged in both Ansys and COMSOL, therefore leaving open the possibility of variations in mesh quality. The level of mesh refinement and method of convergence for the primary simulation work using COMSOL are both discussed in Chapter 4.1.3.

3.3 Preliminary Simulations using Ansys Electronics Desktop

Shown in Figure 12 are the 2D and 3D coaxial cable models created using Ansys. In each of the models, copper is used as the material for the conducting bodies and XLPE for the dielectric(s), both considered to be at room temperature (20°C). The models shown in (a) and (b) of Figure 12 are designed with a single dielectric in-between the two conducting bodies, whereas the models in (c) and (d) utilize a mixed dielectric material

with permittivities starting from the outermost body of 2.25, 2.00, and 1.75 (labeled #1, #2, and #3, respectively, on each figure). Using multiple dielectrics with varying relative permittivities acts as a simple representation of the effects of water tree degradation on cable insulation. It is known that the relative permittivity of a water tree is greatest at the formation point and decreases as the water tree grows inward towards the conductor, which is what was simulated in the mixed dielectric models.

Both geometry types and settings were simulated in Ansys using the Maxwell and Q3D electromagnetic field designs. The Maxwell design calculates solutions to electromagnetic field problems by solving Maxwell's equations in the finite area defined as the model, while the Q3D design utilizes the method of moments. Each Maxwell design setup consists of one or more selected solver types that are used to calculate various field parameters including capacitance and conductance. For the 2D models, the Electrostatics and AC Conduction solver types from the Maxwell design were used to calculate the capacitance and resistance, respectively, of the model. For the 3D models, the Q3D design, which does not require the selection of a solver type, was used to calculate both the capacitance and resistance.

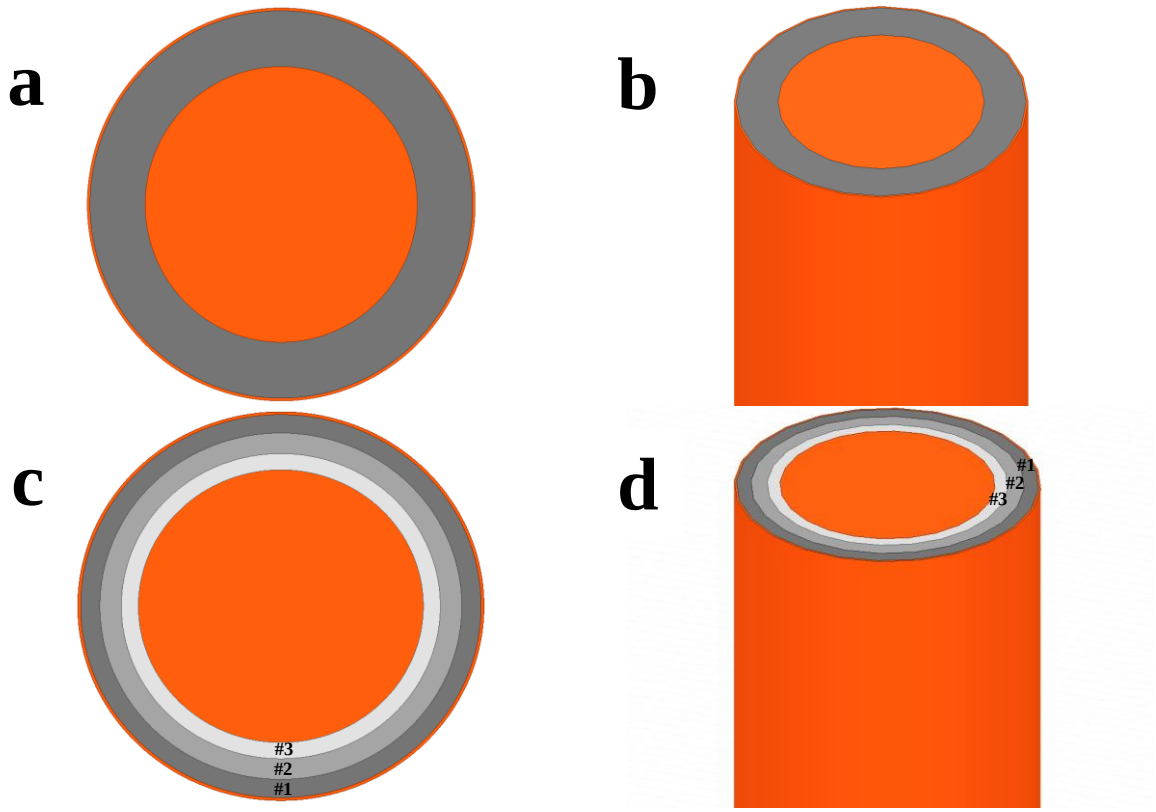

Figure 12. (a) 2D coaxial cable model with a single dielectric using Ansys; (b) 3D coaxial cable model with a single dielectric using Ansys; (c) 2D coaxial cable model with a mixed dielectric (relative permittivities of 2.25, 2.00, 1.75 from the outermost dielectric) using Ansys; (d) 3D coaxial cable model with a mixed dielectric (relative permittivities of 2.25, 2.00, 1.75 from the outermost dielectric) using Ansys.

To simulate using the Maxwell design, voltage excitations must be added to the model, as well as a matrix parameter that provides the direction of flow for the electrical current. The particular values of the voltage excitations are of little importance as long as there is a difference between them. For the sake of simplicity, a voltage excitation of one volt was added to the conductor, and the outer metallic shield was grounded. The Q3D design requires the selection of a signal net and a ground net, which for consistency were chosen to be identical to the voltage excitations in the Maxwell simulations. As for mesh creation, the default settings of amount of acceptable error and number of refinement passes were left unchanged at 1.0% and 10, respectively.

Shown in Figure 13 are the 2D and 3D parallel plate capacitor models created using Ansys. These models use the same materials, methods, and simulation setups as the coaxial cable models previously shown. With respect to the voltage excitations, the top plate is the charged body with an applied voltage of one volt and the bottom plate is grounded. Other than geometry, the only major difference between the two sets of models is the equations used to validate the simulation results, which can be found in Appendix A.

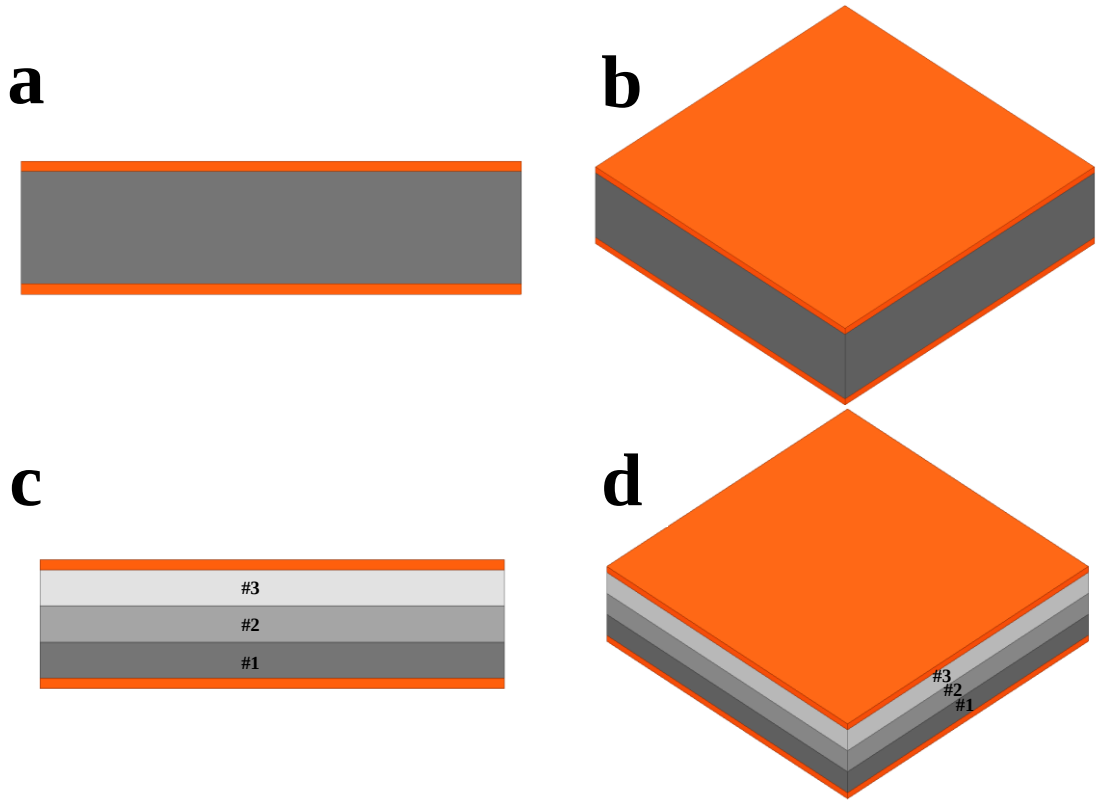

Figure 13. (a) 2D parallel plate model with a single dielectric using Ansys; (b) 3D parallel plate model with a single dielectric using Ansys; (c) 2D parallel plate model with a mixed dielectric (relative permittivities of 2.25, 2.00, 1.75 from the outermost dielectric) using Ansys; (d) 3D parallel plate model with a mixed dielectric (relative permittivities of 2.25, 2.00, 1.75 from the outermost dielectric) using Ansys.

3.4 Preliminary Simulations using COMSOL Multiphysics

Shown in Figure 14 are the 2D and 3D coaxial cable models created using COMSOL. The materials and geometries of these models are the same as their respective equivalents used in Ansys, which allows for direct comparison of results between the simulation software. The selection of voltage excitations is also identical to that of Ansys with the conductor carrying one volt and the outer metallic shield being grounded. As with those in Ansys, no mesh refinement or convergence was performed for the simulations in COMSOL.

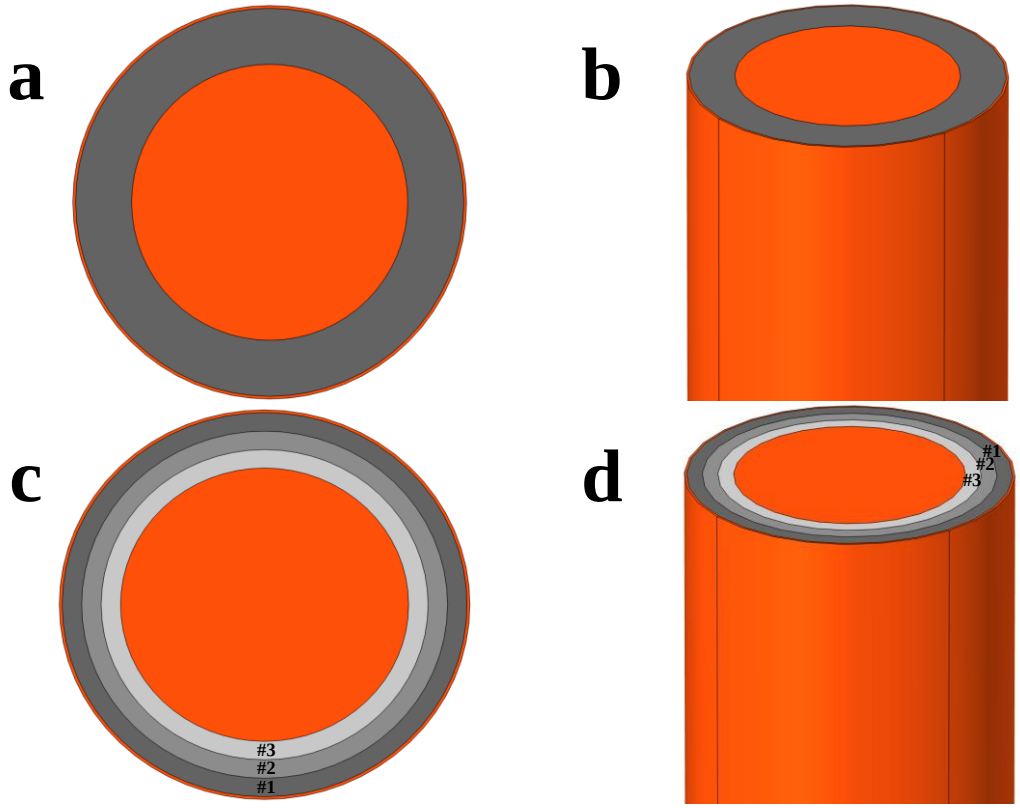

Figure 14. (a) 2D coaxial cable model with a single dielectric using COMSOL; (b) 3D coaxial cable model with a single dielectric using COMSOL; (c) 2D coaxial cable model with a mixed dielectric (relative permittivities of 2.25, 2.00, 1.75 from the outermost dielectric) using COMSOL; (d) 3D coaxial cable model with a mixed dielectric (relative permittivities of 2.25, 2.00, 1.75 from the outermost dielectric) using COMSOL.

Although very closely related, Ansys and COMSOL differ in their methods of preparing a model for simulation. Instead of choosing a base design to simulate with, COMSOL requires the selection of one or more physics branches along with a particular study type that defines how the model will be analyzed. The Electric Currents and Electrostatics physics branches, along with the Stationary study type, were used to calculate the resistance and capacitance, respectively, of the cable model. Additional discussion regarding these physics branches and study type is provided in Chapter 4.1.2.

Shown in Figure 15 are the 2D and 3D parallel plate capacitor models created using COMSOL. As with those created using Ansys, these models use the same materials, methods, and simulation setups as the coaxial cable models previously shown. Additionally, the placement of the voltage excitations is identical to what was done in Ansys, with the top plate acting as the charged body carrying an applied voltage of one volt and the bottom plate being grounded.

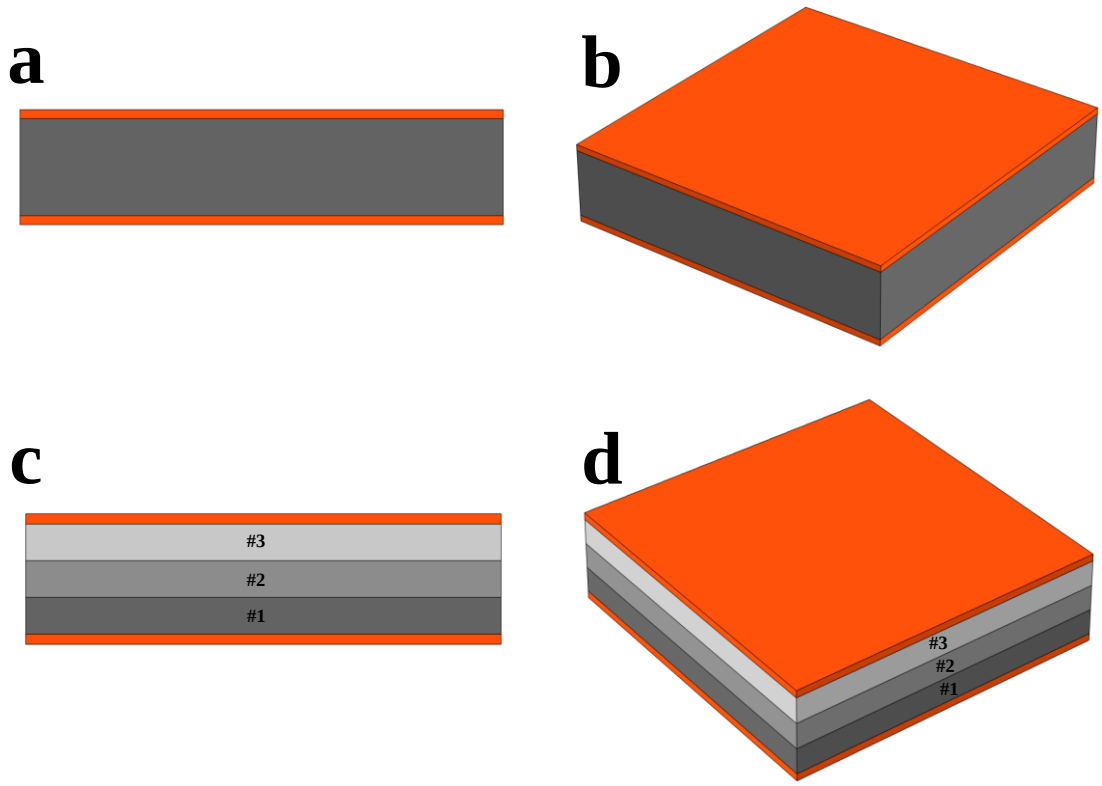

Figure 15. (a) 2D parallel plate model with a single dielectric using COMSOL; (b) 3D parallel plate model with a single dielectric using COMSOL; (c) 2D parallel plate model with a mixed dielectric (relative permittivities of 2.25, 2.00, 1.75 from the outermost dielectric) using COMSOL; (d) 3D parallel plate model with a mixed dielectric (relative permittivities of 2.25, 2.00, 1.75 from the outermost dielectric) using COMSOL.

3.5 Validation and Verification

Validation and verification (V&V) are critical steps in evaluating the credibility of an FEA model. Validation deals with how accurate the model is and how well it correlates with the physical phenomena being simulated; verification concerns the accuracy of the results computed by the model and the amount of acceptable error in comparison to known values or facts. V&V also concerns refinement and convergence of the generated mesh used in the simulations. As previously noted, mesh refinement and convergence were not critical components or goals of the preliminary simulations and are not discussed here.

With regards to validation, both model types correlate well with known physical phenomena. The materials used in the models and their respective properties, most notably relative permittivity and electrical conductivity, accurately correspond to those of known cable components. The geometry used for the coaxial cable models is consistent with that of a simplified physical cable, while the geometry for the parallel plate capacitor models is consistent with basic physical examples. Lastly, the placement of the voltage excitations is typical to that which is found in physical cables as well as basic parallel plate capacitor designs. Specifically, the conductor is selected to be the charged body, and the other component, which for the coaxial cable models is the outer metallic shield and for the parallel plate capacitor models is the bottom plate, is selected to be the grounded body. Additional discussion of model validation including rationale for the selection of the parameters used for the parametric study and their respective ranges is found in Chapter Four.

For the purpose of this thesis, verification of the preliminary simulations occurs in three areas: comparison of simulation results to known analytical solutions, comparison of simulation results to those found in related literature using XLPE as the insulation material, and comparison of simulation results between Ansys and COMSOL. Further discussion and rationale for each area of verification will be given in the forthcoming sections. Satisfactory verification in each of these areas will provide a high level of confidence in both the setup of the primary simulations as well as the results that are produced from the parametric study.

3.5.1 Comparison to Analytical Solutions

Because the geometries used in the preliminary simulations are quite common, there exists known analytical solutions for various calculated parameters that can be directly compared to the results obtained from the simulations. Values for the various calculated parameters (i.e. capacitance and resistance) are provided in Appendix B, which also includes the percent differences between the analytical and simulation values. The following paragraphs will discuss the findings from this verification approach and the conclusions that can be inferred.

For both the 2D and 3D coaxial cable models, it was found that there was less than 0.1% difference between the analytical and simulation capacitance values using a single dielectric, and less than 2% difference being found for the mixed dielectric models. The resistance values found using Ansys had a 0.5% difference with the analytical values, but the values obtained using COMSOL were identical to those calculated using the analytical approach, thus yielding a difference of zero. It is worth mentioning that resistance was not found for the 3D coaxial cable models using Ansys because of simulation errors with this particular geometry. Regardless, the Ansys results from the 2D models are well aligned with results obtained from the analytical approach. Overall, with the exception of the mixed dielectric models, COMSOL produced values more closely aligned with the corresponding analytical values than Ansys.

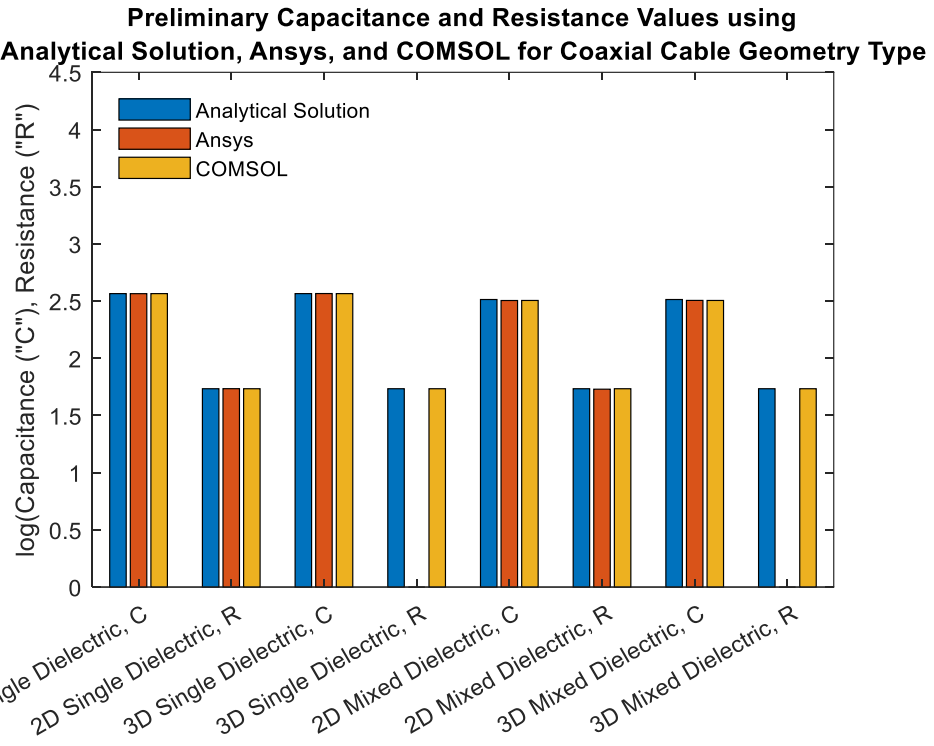

Figure 16. Capacitance (“C”) and resistance (“R”) values obtained from the analytical solution, Ansys, and COMSOL for the coaxial cable geometry type.

For the 2D parallel plate capacitor models, it was found that there was little to no difference between each simulation value when compared to the corresponding value determined from the analytical approach. As a result, percent differences between the simulation and analytical values were either zero or negligible. The 3D parallel plate capacitor models produced capacitance values identical to those calculated using the analytical approach, but resistance values varied between the two software. The percent differences were found to be 7% and 6% for the single dielectric and mixed dielectric models, respectively, using Ansys, whereas the resistance values determined from COMSOL were identical to the corresponding analytical values. Overall, the simulation and analytical values were analogous for each model and software with the only exception being the resistance values for the 3D models in Ansys.

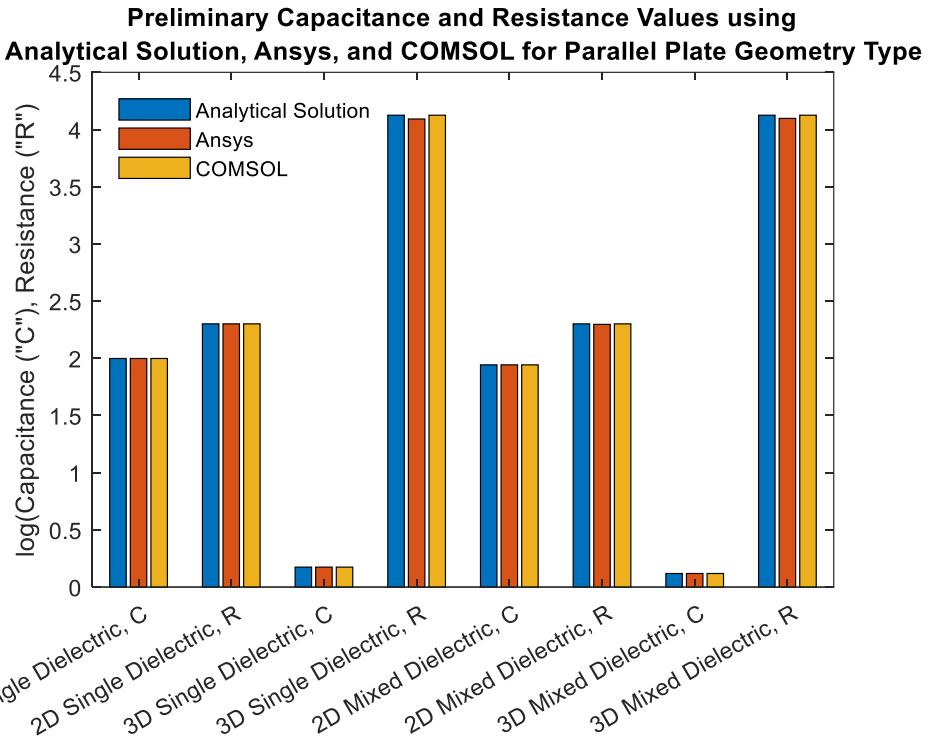

Figure 17. Capacitance (“C”) and resistance (“R”) values obtained from the analytical solution, Ansys, and COMSOL for the parallel plate geometry type.

It can be concluded that the Ansys and COMSOL simulations were successfully verified using the approach of comparison to analytical solutions. Although quite similar, and even identical for some models, the results obtained from the COMSOL models were more closely aligned with the corresponding analytical results than those obtained from the Ansys models. One possible explanation for this outcome is inconsistent mesh quality between each software, which is known to affect the accuracy of simulation results. It is possible that the automatically generated mesh in COMSOL may have been finer than the mesh generated in Ansys leading to slightly more accurate results. As previously noted, mesh refinement was not a critical component or goal of the preliminary simulations, so the truth or lack thereof for this explanation is of little importance. Mesh refinement of

the updated cable model, which is of significant importance for the primary simulation work of this thesis, is discussed in Chapter 4.1.3.

3.5.2 Comparison to Literature

As previously addressed in Chapter Two, there has been a significant amount of research done regarding the simulation of cable degradation. The vast majority of research has used XLPE as the insulation material in part because of its strong dielectric and mechanical properties when compared to EPR [78]. Additionally, the wide range of filler materials typically present in EPR make it a challenging material to provide definitive conclusions for and thus limit its use in cable simulation literature [79]. Despite these facts, the critical material properties used in the simulations for this thesis, which are relative permittivity and electrical conductivity, are similar for both XLPE and EPR. This allows for comparison between these two materials when considering results obtained using the simulation methods presented in this thesis.

When comparing the capacitance values of the mixed dielectric models to those of the single dielectric models, it was found that the value of the capacitance for the mixed dielectric models is always less than that of the single dielectric models. This result can be compared with a variety of literature sources that simulate water tree degradation in XLPE cables, some of which were previously discussed in Chapter 2.2. In these sources, as the water tree grows inward towards the conductor, the effective relative permittivity of the insulation material is increasing which leads to an increase in the value of the capacitance. The effective relative permittivity of the mixed dielectric models is less than that of the single dielectric models, which explains the decrease in capacitance for each

simulation case. As for the resistance values, no change is observed between the single and mixed dielectric models for a particular geometry because resistance is not a function of relative permittivity and the electrical conductivity of the insulation material is not changing. If the electrical conductivity were to change, which is what typically occurs when a water tree grows through the insulation, there would be a change in the value of the cable's resistance, as shown in various literature sources [52,80].

The preliminary simulations previously mentioned but not discussed in detail are those that include a rectangular section of water or air inside the insulation material of a single dielectric model. The water or air section would increase in depth through the insulation material, thus simulating the growth pattern of a physical water tree. The resulting relationships between capacitance, resistance, and voltage and electric field distribution versus section depth could be determined and compared to those relationships found in the literature for XLPE-insulated cables. From these simulations, it was found that as the depth of the water or air section increases, the capacitance increases, the resistance decreases, and the distortion of the voltage and electric field distribution increases only in the area where the water or air section is located. These results are confirmed when compared to similar simulations found in various literature sources [52,80].

3.5.3 Comparison between FEA Software

At the beginning of the work for this thesis, the FEA software that would be used had not been decided. Ansys and COMSOL emerged as the primary candidates because of the many advantageous features they possess, and their solid reputation for being able

to solve complex electromagnetic problems such as those presented in this thesis. After much consideration and testing, COMSOL was selected in part because of its more streamlined multiphysics framework compared to Ansys. Although COMSOL would be used for the primary simulation work of this thesis, it was decided that both COMSOL and Ansys would be used concurrently for the preliminary simulations in order to verify the simulation setups and results from each software in comparison to each other.

As shown in Figures 16 and 17, the preliminary simulation results for each geometry type and configuration were fairly consistent between Ansys and COMSOL. The largest differences occurred with the single and mixed dielectric 3D parallel plate capacitor models, but only for the resistance values. As previously noted, one possible explanation for these differences is inconsistent mesh quality between each software. COMSOL's automatically generated mesh may have been finer than the mesh generated by Ansys, particularly for the 3D models which are larger than the 2D models and thus require more area to be meshed. It was also determined that the preliminary simulations mentioned but not discussed in detail yielded identical trends for capacitance, resistance, and distortion of the voltage and electric field distribution for both Ansys and COMSOL. Although the specific values were slightly different between each software, the trends between the values and depth of the air or water section were consistent, which provides a high level of confidence in the simulation setups. Overall, it can be concluded that each of the preliminary simulation setups in both Ansys and COMSOL are accurate representations of each other and can produce consistent results.

3.6 Concluding Remarks

A variety of preliminary simulations were performed using two FEA software, Ansys and COMSOL. Two geometry types, a parallel plate capacitor and a coaxial cable, were created and simulated in both 2D and 3D configurations, and with a single and mixed dielectric setup. XLPE was used as the insulation material of the models because of its widespread use in related literature, as well as the fact that it possesses comparable material properties to those of EPR. The goals of these preliminary simulations were to develop proficiency in electromagnetic simulation, assess the capabilities of each software, and validate and verify the results against known solutions, related literature, and direct comparison between software. Upon completion of the preliminary simulations and collection of the results, it was determined that each goal was successfully achieved. Additionally, the simulation results from each software were found to be well aligned with the results from each of the three verification areas, which provides a high level of confidence in each of the simulation setups.

Based on what was learned from the preliminary simulations, it was decided that COMSOL would be the software of choice for the primary simulation work of this thesis. In addition to a more streamlined multiphysics framework, COMSOL has parametric evaluation features that appeared to be more intuitive than those found in Ansys. Of the geometry types and configurations that were simulated, the 2D coaxial cable model was selected to be updated for the primary simulation work. The 2D configuration was selected based on the accuracy of the results in comparison to those obtained from the same geometry type but in the 3D configuration. Additionally, the 2D model provides a

better visual representation of the effects of water tree degradation and requires less computer resources compared to the 3D model. Going forward, the 2D coaxial cable model will be transformed into a more comprehensive model that is representative of a physical underground MV cable such as the one shown in Figure 2. The materials and dimensions of the updated cable model, as well as the iterative design approach that took place, are described in further detail in the following chapter.

CHAPTER FOUR:

SIMULATION METHODOLOGY AND SETUP OF THE PARAMETRIC STUDY

4.1 Simulation Methodology

This section provides a detailed description of the simulation methodology with discussions regarding the updated cable model, simulation methods using COMSOL, mesh refinement and convergence, setup of the parametric study, the simulated temperature and frequency ranges, and the geometry and composition of the water tree region.

4.1.1 Updated Electric Cable Model

The materials and dimensions of the cable model components used in the simulations are based on those of a physical NPP MV and are provided in Table 1. Instead of the cable conductor being made of multiple conducting strands, as is typical in a physical cable, it is modeled in the simulations to be a single strand with a voltage rating of 15 kV. From initial testing, it was determined that the electrical properties of the cable are nearly identical when using either multiple strands or a single strand as the conductor. To lessen use of computer resources and simplify the model, a single strand conductor made of aluminum was used. The conductor and insulation shields were both made of a semi-conductive EPR-backed material rated for use with MV cables. The cable insulation was made from EPR, which is the most common insulation material used in MV cables. The grounded metallic shield was made from copper, and the cable jacket was made from PVC. The cable model was surrounded by an air medium to allow proper calculation of the cable's electric field.

Table 1. Cable components, outer radii from the cable center, and materials.

Cable Component	Outer Radius (mm)	Material
Conductor	13.98	Aluminum
Conductor Shield	14.98	Electrical Tape
Insulation	19.65	EPR
Insulation Shield	21.04	Electrical Tape
Metallic Shield	21.32	Copper
Jacket	23.50	PVC

Multiple iterations of this cable model were created and tested to insure equivalency of results. For each iteration, V&V was performed by comparing common electrical properties of the cable to analytical solutions and results found in literature for XLPE-insulated cables. The cable model was made progressively more complex after each iteration until reaching the final model shown in Figure 18.

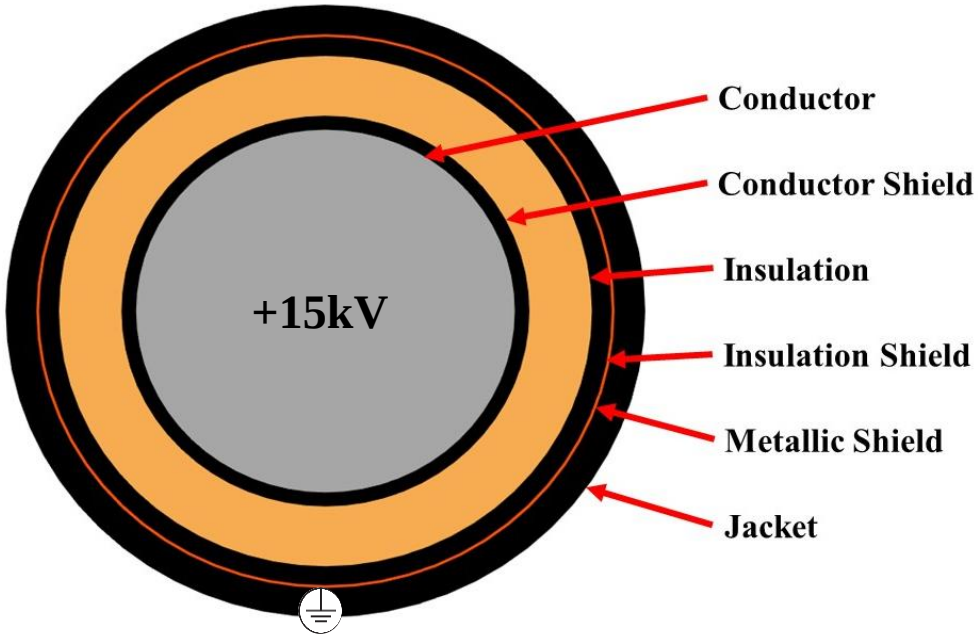

Figure 18. EPR-insulated cable model without any water treeing.

4.1.2 Simulation Methods

The Electric Currents, Electrostatics, and Heat Transfer in Solids physics branches in COMSOL were used for the simulations. The Electric Currents branch is commonly used to simulate AC and DC electric currents in capacitive and conductive applications [81]. It uses the electrical conductivities of the various materials to calculate the electric current flowing through the cable which is used to calculate the resistance [80]. The Electrostatics branch is used primarily to simulate charge conservation in dielectric materials like cable insulation under static conditions [81]. Instead of the electrical conductivity, this physics branch uses the relative permittivities of the materials to calculate the capacitance of the cable. The mathematical characterization defining the cable's electric field using both the Electric Currents and Electrostatics physics branches are described by the following governing equations:

$$\nabla \cdot J = Q_{j,v} \qquad J = \sigma E + j\omega D + J_e \qquad E = -\nabla V \tag{1}$$

$$\nabla \cdot D = \rho_v \qquad E = -\nabla V \tag{2}$$

where, J is conduction charge density (A m^{-2}), V is applied voltage (V), $Q_{j,v}$ is charge density (C m^{-3}), σ is electrical conductivity (S m^{-1}), ω is angular frequency (rad s^{-1}), E is electric field (V m^{-1}), D is electric displacement (C m^{-2}); J_e is external charge density (A m^{-2}), and ρ_v is volumetric charge density (A m^{-2}).

The Heat Transfer in Solids branch is used to determine the localized temperature rise (LTR) around the water tree region produced by electromagnetic heating. For the simulations using this physics branch, the conductor was set to an initial temperature of 70°C, while the other cable components all have an initial temperature of 20°C.

The Stationary study type was used to calculate the capacitance and resistance of the cable. For this study type, the field variables do not change over time, which allows for the computation of static electric fields. Because the field variables are constant, the term $j\omega D$ in the second Electric Currents equation is canceled out. The Frequency Domain study type was used to calculate the electric field strength at the pole of the water tree region. This study type requires a frequency value to be inputted by the user and in doing so creates a voltage source with an AC sinusoidal waveform, which is representative of physical cable operation. For the simulations involving heat transfer and LTR, a Frequency-Transient study type was used with a time duration of ten seconds. The frequencies used in the simulations are provided in a forthcoming section.

4.1.3 Mesh Refinement and Convergence

An important aspect of every FEA work is creating an adequately refined mesh. This is accomplished through a process called mesh convergence, which is used to determine the required number of elements in a model to ensure accurate results. Mesh convergence takes an initially coarse mesh with a large element size and smooths it into a finer mesh having a smaller element size. This is done through an iterative approach where a solution is repeatedly calculated and compared against a known solution until the error between the two reaches an acceptable amount. The overall simulation error is minimized by refining localized areas of high error found within the model. The level of refinement is heavily dependent on the model being simulated and the required accuracy of the simulation results.

The mesh for the primary simulations was refined by decreasing the global element size until the difference between solutions was minimized. In addition, extra refinement was added to the pole of the water tree region closest to the conductor, which is the calculation point for the electric field strength and LTR. Prior to refinement, the global element size ranged from a minimum value of 0.028 mm to a maximum value of 63 mm. After refinement, the global element size ranged from a minimum value of 0.04 mm to a maximum value of 2 mm. Additionally, the extra refinement provided at the pole of the water tree region decreased the maximum element size in that area to 0.10 mm. Mesh comparison prior to and after refinement is visually shown in Figure 19.

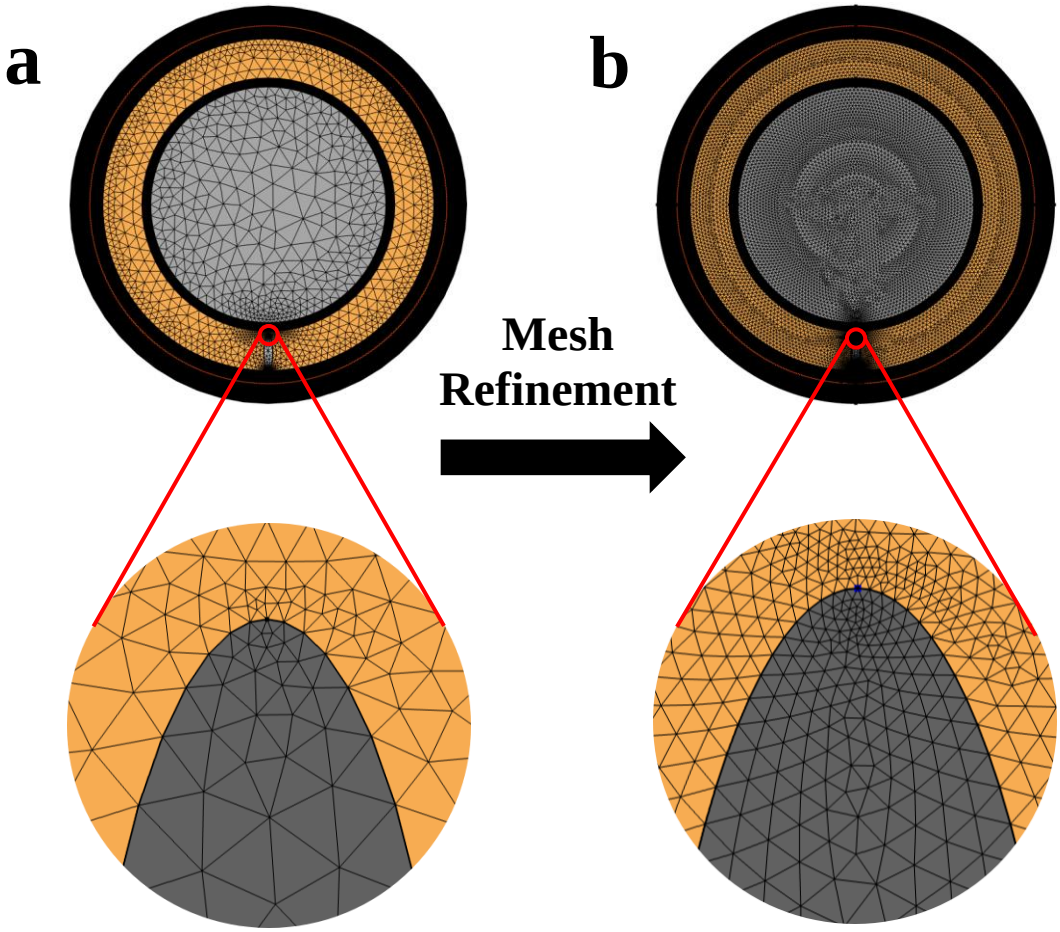

Figure 19. (a) Model prior to mesh refinement; (b) model after mesh refinement.

Since the pole of the water tree region is the calculation point, greater emphasis was placed on decreasing the element size around that particular area. This was done to account for the increasing error that occurs as the water tree aspect ratio (AR), defined as the ratio of the major axis to the minor axis of the ellipse, increases. As the AR increases, the element size required for sufficiently accurate calculations at the pole of the water tree region becomes continuously smaller.

4.2 Setup of the Parametric Study

Parametric studies are advantageous in that they allow for quick analysis of multiple parameters at varying ranges and are easily automated using simulation software such as COMSOL. The parameters being evaluated in this parametric study are cable temperature, water tree geometry, water tree composition, and cable operating frequency. Each combination of parameter values was simulated, but for the sake of limiting redundant observations due to minimal differences, only results using a subset of combinations are provided in this thesis. The ranges and rationale concerning the use of each parameter are provided in the following sections.

4.2.1 Temperature Range

A temperature range of 0 to 200°C in increments of 20°C was used for the simulations. This range was chosen because the vast majority of cable operations occur between the minimum and maximum values of the given range [38]. With the exception of the simulations to determine LTR, a constant temperature was used for the entire area of the cable model, which would not be true for a physical cable. It should also be noted

that temperatures around 140°C are typically only reached during emergency operating conditions and only for short periods of time [82].

Relative permittivity and electrical conductivity, both indicators of a material's ability to conduct electricity, change with temperature. This fact must be considered when examining the effect of changing temperature on the rate of cable degradation caused by water treeing. For cable conductors made from copper or aluminum, temperature and electrical conductivity are inversely related, with no considerable relationship between temperature and relative permittivity. For the EPR insulation, temperature and electrical conductivity are directly related, with temperature and relative permittivity being inversely related. Additionally, calculation of the LTR required thermal conductivity and isobaric specific heat capacity values for EPR, which were taken at a temperature of 20°C [83].

4.2.2 Frequency Sweep

To determine the effect of operating frequency on the rate of water tree degradation, a frequency sweep ranging from 0.01 Hz to 1 MHz was added as a component of the parametric study. The frequencies of 0.01, 60, and 800 Hz that provide a portion of the results given in Chapter Five are based on those used for physical cable tests in the field. A frequency of 0.01 Hz is typically used for VLF voltage withstand testing, and for the purpose of this thesis can be considered effectively equivalent to DC operation. A frequency of 60 Hz is the standard operating frequency for MV AC cables in the United States. From ASTM D149, the maximum recommended frequency for cable testing is 800 Hz, and frequencies greater than that value are known to potentially cause

dielectric heating which accelerates the aging process of the cable [71]. The results of simulating with frequencies above 800 Hz, specifically 10,000 and 1,000,000 Hz, are also provided in Chapter Five and are discussed in a theoretical context.

4.2.3 Water Tree Geometry and Composition

An ellipse was used to represent the geometry of the water tree region in the simulations. Although physical water trees are composed of a collection of connected micro-sized cylindrical pathways [20], the overall structure of these pathways is typically well-encompassed in the shape of an ellipse, as shown in Figure 20. Because of the varying geometry of water trees, also shown in Figure 20, the AR of the ellipse, defined as the ratio of the major axis to the minor axis, was varied from one to 60 in increments of six in order to understand the effect of narrower water trees on the electrical properties of the cable. The depth of the water tree region, starting from the outer edge of the insulation and working towards the conductor, was varied between 10 and 100% in increments of 10%. This growth path is representative of that of a vented water tree, which is shown in Figures 8 and 20.

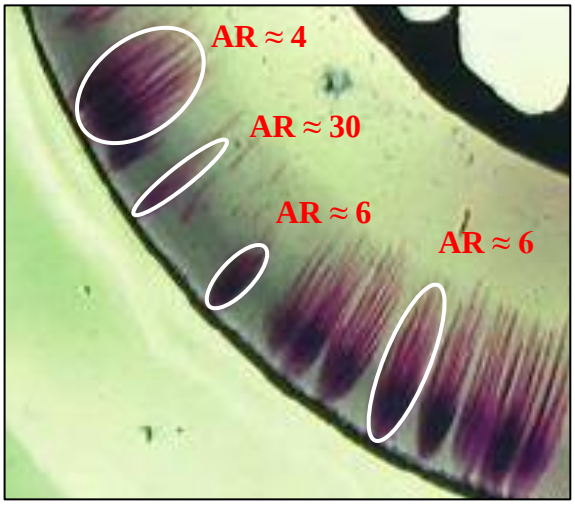

Figure 20. Water trees with varying elliptical geometries [84].

To match the experimental work of the project of which this thesis is associated with, the composition of the water tree region was varied between pure distilled water (H_2O) and aqueous copper sulfate ($CuSO_4$) (constant concentration of 1.23 M across the temperature range). H_2O was selected because it represents the most basic composition of a water tree and is easily obtainable in a laboratory setting for use in physical cable testing. $CuSO_4$, which is a known ionic solution, was selected because of the current hypothesis in cable degradation literature that the presence of ionic solutions results in an accelerated rate of water tree degradation.

Electrical and thermal properties of the two compositions varied with temperature and were taken from ASTM D1125 and related literature [85-92]. Both compositions exhibit the same relationships between temperature and relative permittivity, and temperature and electrical conductivity. Temperature and relative permittivity are inversely related, with increasing temperature producing a decreasing relative permittivity; temperature and electrical conductivity are directly related, with increasing temperature producing an increasing electrical conductivity. These relationships are visually shown in Appendix C.

The following assumptions are made regarding the electrical properties of the water tree model:

1. The entire composition of the water tree region is either H_2O (assumed to be saturated) or $CuSO_4$ in aqueous form.
2. The relative permittivity and electrical conductivity values are constant across the entire length of the water tree region.

The primary purpose of these two assumptions is to simply the setup and analysis portions of the simulation work. It should be noted that a physical water tree will have varying relative permittivity and electrical conductivity values across its length, and the composition of the water tree region will be a mixture of aqueous solution and insulation material. This mixture, which is based on the principles of effective medium theory, will create a composition having composite relative permittivity and electrical conductivity values that are somewhere between those of both the aqueous solution and the insulation material. Because this thesis is primarily interested in degradation trends rather than individual values, these assumptions will not have a significant effect on the results and conclusions.

Table 2. Simulation parameters and values used for the parametric study.

Simulation Parameters and Values	
Frequency (Hz)	0.01; 60; 800; 10,000; 1,000,000
Temperature (°C)	0; 20; 40; 60; 80; 100; 120; 140; 160; 180; 200
Water Tree Aspect Ratio (AR)	1; 6; 12; 18; 24; 30; 36; 42; 48; 54; 60
Water Tree Depth (%)	10; 20; 30; 40; 50; 60; 70; 80; 90; 100
Water Tree Composition	H_2O; $CuSO_4$

CHAPTER FIVE:
RESULTS AND DISCUSSION

5.1 Overview of Results

The results for this thesis are derived from five separate but interrelated areas each pertaining to the measurement of cable degradation caused by water treeing:

- Global Capacitance
- Global Resistance
- Voltage and Electric Field Distribution
- Localized Specific Energy Absorption Rate
- Localized Temperature Rise

The first area consists of global capacitance measurements in the temperature range of 0 to 200°C taken at various instances along the water tree's growth path towards the conductor. A comparison of the capacitance measurements between the pure distilled water (H_2O) and aqueous copper sulfate ($CuSO_4$) compositions is also provided. The second area consists of global resistance measurements using the same temperature range and water tree growth path as the first area, along with a similar comparison between the compositions. The third area consists of a variety of 2D surface plots showing the cable's voltage and electric field distribution for different conditions from the parameters of water tree depth, water tree aspect ratio (AR), water tree composition, operating frequency, and temperature. These plots are visually analyzed and compared to one another to determine differences in the amount of observable distortion for the various conditions. The fourth area consists of a variety of plots comparing localized specific

energy absorption rate (SAR) measurements, water tree depth, water tree AR, temperature, and operating frequencies for compositions of H_2O and $CuSO_4$. Because the maximum electric field intensity occurs at the pole of the water tree region, this position serves as the calculation point for the electric field strength which is then used in the calculation of the SAR. The fifth area consists of a discussion and analysis regarding the occurrence of a localized temperature rise (LTR) at the water tree pole. In addition, because SAR is known to be directly related with LTR, an effort is made to compare the temperature change at the pole of the water tree region with the SAR measurements previously taken.

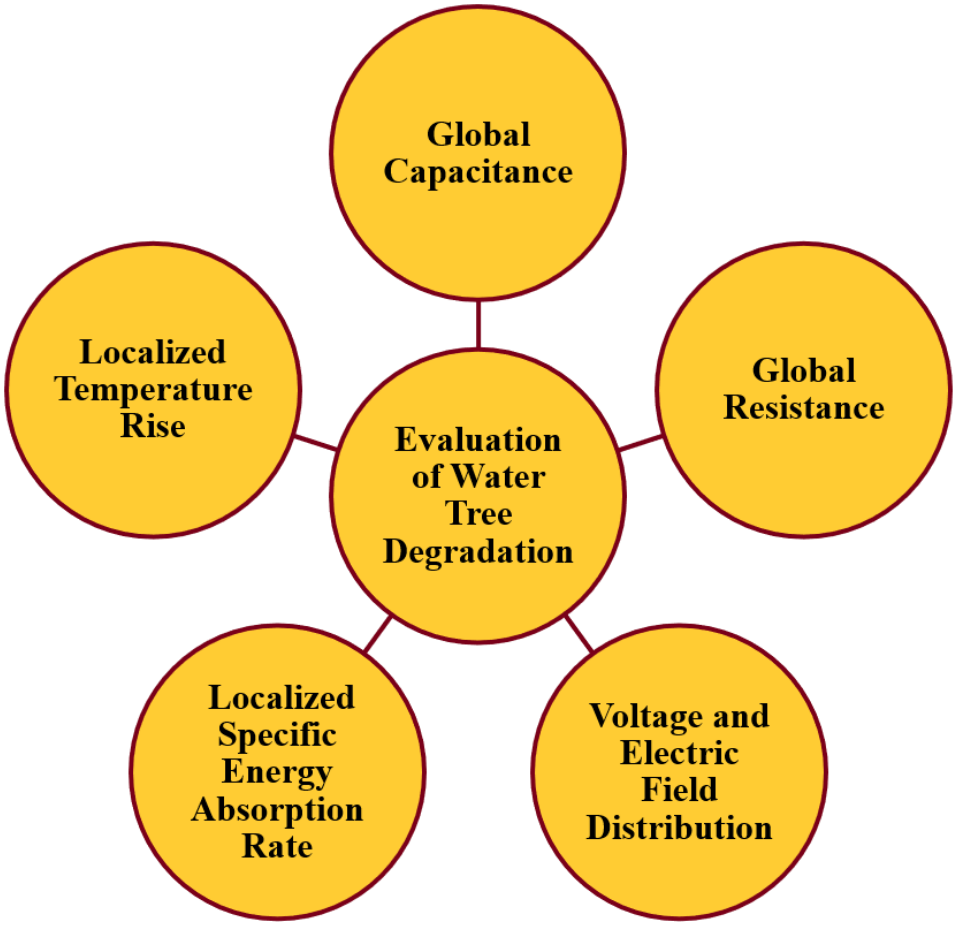

Figure 21. Five areas of results pertaining to the evaluation of water tree degradation.

After presenting each area of results separately, an overall discussion comparing all five areas is provided. Although each area on its own provides a significant amount of information regarding the effects of water treeing in EPR-insulated MV cables, when taken together, the results provide a more comprehensive understanding of the water treeing phenomenon. Additionally, each area will be compared to physical tests to show that results obtained from both FEA and physical testing can be correlated.

5.2 Model Assumptions

Before presenting the results of this thesis, it is worth reviewing the pertinent assumptions that characterize the simulation model:

- The conductor is defined as a voltage source with a value of 15 kV, and the metallic shield is grounded. AC voltage with a sinusoidal waveform is used for the voltage and electric field distribution, SAR, and LTR areas of results, whereas DC voltage is used for the global capacitance and global resistance areas.
- The current conservation boundary condition is active for the non-conducting cable components, which implies that their electrical conductivity and relative permittivity values are equivalent to those of the component materials.
- The cable model is surrounded by an air medium to allow proper calculation of the electric field. The material properties of the air medium do not change with temperature.
- The electrical properties of the water tree are equivalent to those of the composition being simulated (H_2O or $CuSO_4$).

- The electrical properties of the cable components and water tree are homogeneous and do not vary within the areas they occupy.
- Each area of results except LTR assumes a constant initial temperature for the entire cable which is equivalent to that which is being simulated. For LTR only, the conductor is set to an initial temperature of 70°C, while the other cable components and water tree all have an initial temperature of 20°C.
- LTR measurements are recorded after 10 seconds of exposure to the cable's electric field.

5.3 Global Capacitance

Figures 22 and 23 show the logarithm of the cable's global capacitance versus water tree depth for compositions of H_2O and $CuSO_4$, respectively. A base-10 logarithmic transformation was applied to the global capacitance measurements to match the other areas of results. The global capacitance is defined as the total measure of capacitance for the entire system being simulated. Because the capacitance measurements were found to be largely independent of water tree AR, only a single AR (AR = 6) is used. The temperature of the cable is varied from 0 to 200°C in increments of 20°C. The Electrostatics physics branch and Stationary study type in COMSOL, which assume nonchanging field variables and a static electric field, were used to calculate the global capacitance at each temperature and water tree depth percentage. In comparison to those studies that used XLPE as the insulation material, the global capacitance results presented in this thesis using EPR exhibit a similar trend with respect to water tree depth [20,52,80].

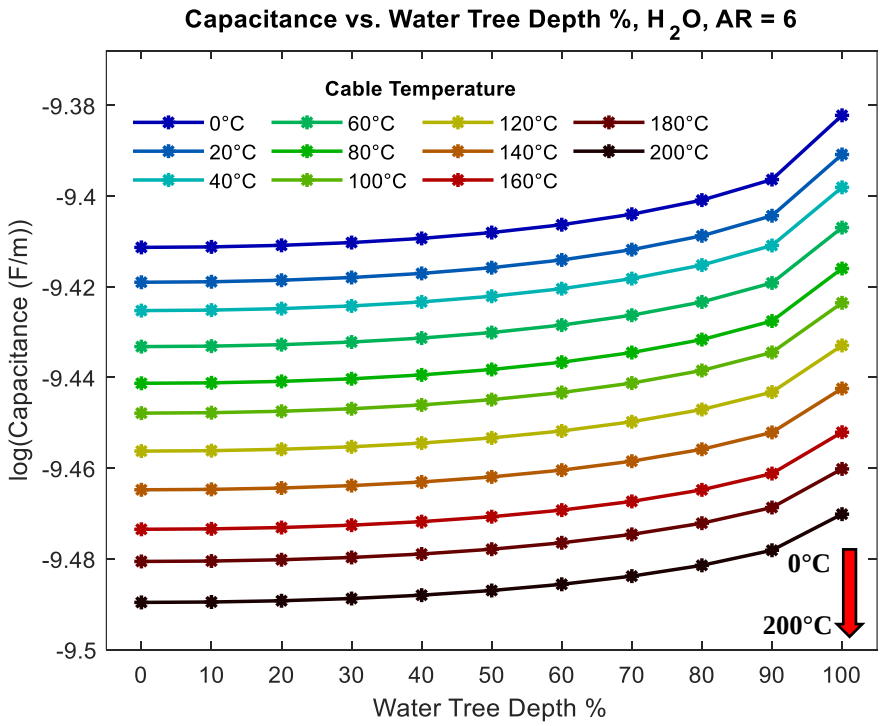

Figure 22. Logarithmic capacitance versus water tree depth using H_2O. The arrow denotes the direction of temperature increase corresponding to the order of data sets.

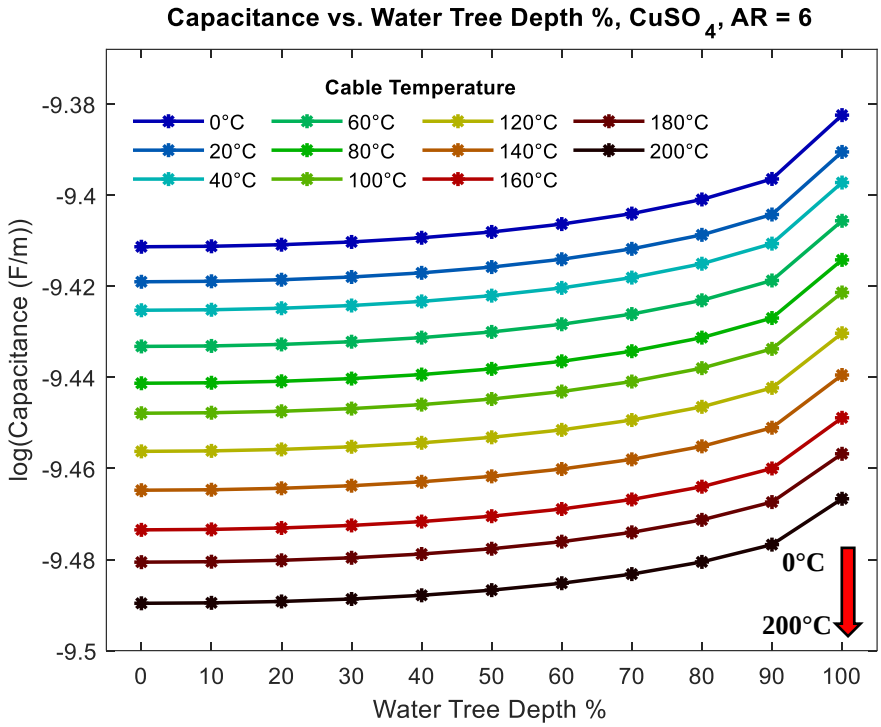

Figure 23. Logarithmic capacitance versus water tree depth using $CuSO_4$. The arrow denotes the direction of temperature increase corresponding to the order of data sets.

For both compositions, it is observed that capacitance increases as the water tree grows inward from the outer edge of the insulation toward the conductor. This is explained by the fact that as the two conducting bodies (water tree and conductor) grow closer to one another, the attraction between their respective charges becomes greater which leads to an increase in the overall capacitance of the system. For both compositions, although the capacitance is continually increasing throughout the water tree's growth path, the magnitude of increase between depths of 10 and 70% is smaller compared to that which is found between depths of 70 and 100%. For a temperature of 200°C, the percent difference in capacitance between depths of 10 and 70% is approximately 1.3% and 1.5% for H_2O and $CuSO_4$, respectively, whereas the percent difference between depths of 70 and 100% is approximately 3.2% and 3.9% for H_2O and $CuSO_4$, respectively. Based on these results, it can be stated that the capacitance increases with a greater magnitude once the water tree has grown to a depth of 70% towards the conductor.

Another observation from Figures 22 and 23 is that the cable's capacitance is affected by temperature, with an increase in temperature producing a decrease in capacitance. This can be explained when considering the relationship between temperature and the relative permittivity of EPR. As temperature increases, EPR's relative permittivity decreases because of its change in density [93]. It is known that the density of certain polymers such as EPR generally decreases with increasing temperature [93]. This decrease in density leads to a reduction in the average number of dipoles contributing to dielectric polarization, which produces a decrease in relative permittivity

[93]. Because relative permittivity is directly related to the calculation of capacitance in a cable such as what was simulated, a decreasing relative permittivity results in a decreasing capacitance, which is what is shown in Figures 22 and 23.

Figure 24 shows the logarithm of the difference in the cable's capacitance between the $CuSO_4$ and H_2O compositions versus water tree depth. Overall, capacitance values for the compositions are nearly equivalent with the largest percent difference between them being approximately 0.8% at a water tree depth of 100% and temperature of 200°C. Nevertheless, there does exist a noticeable relationship between the difference in capacitance and water tree depth. It can be observed that as water tree depth increases, the difference in capacitance between the compositions also increases, with the minimum and maximum differences occurring at water tree depths of 10 and 100%, respectively. As the water tree grows inward, the region of the cable containing either H_2O or $CuSO_4$ becomes larger which makes the difference in electrical properties between the compositions become more profound. Because of this, the difference in capacitance between the compositions becomes greater as the region containing the water tree becomes larger with increasing depth.

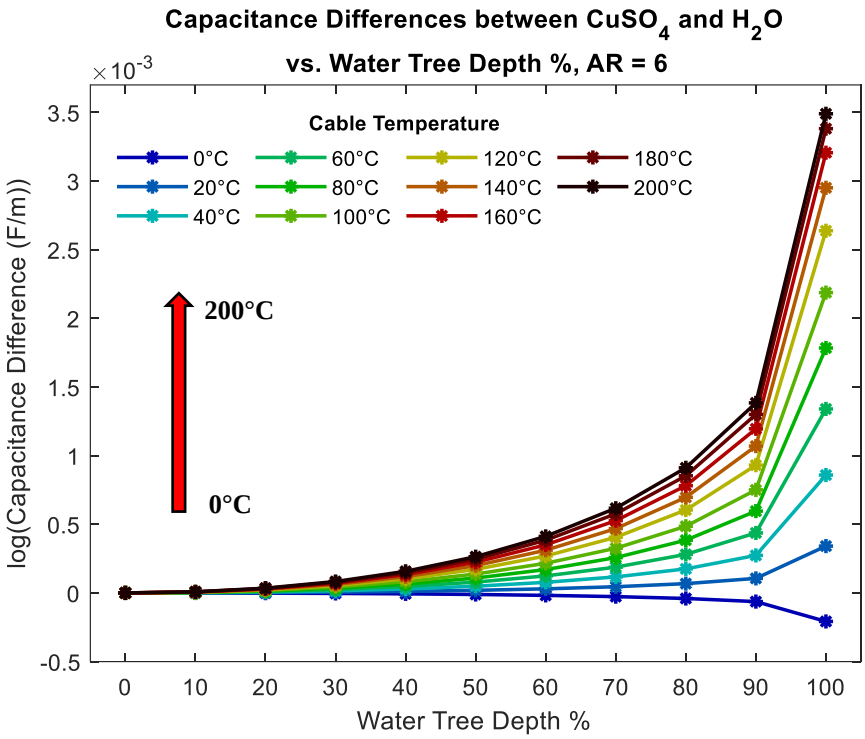

Figure 24. Logarithmic difference in capacitance between $CuSO_4$ and H_2O versus water tree depth. The arrow denotes the direction of temperature increase corresponding to the order of data sets.

Based on what is shown in Figure 24, there also exists a noticeable relationship between the difference in capacitance and the temperature of the cable. It can be stated that there is a relationship between the two parameters, with an increasing temperature producing a greater difference in capacitance. This relationship is illustrated when examining the percent differences in capacitance at the minimum and maximum temperatures using measurements taken at a water tree depth of 100%. At the temperature minimum of 0°C, the percent difference in capacitance is approximately 0.05%, whereas at the temperature maximum of 200°C, the percent difference is approximately 0.8%. Although small, it is quite possible that the difference in capacitance is large enough to affect the cable's performance, particularly at higher temperatures.

Apart from 0°C, each temperature in the simulated range produced a difference in capacitance that favored $CuSO_4$ over H_2O across the water tree's growth path. This is explained when considering how the relative permittivity of each composition changes across the simulated temperature range. It is known that 0°C is the only temperature where the relative permittivity of H_2O is greater than that of $CuSO_4$. For each temperature in the range of 20 to 200°C, the opposite is true; the relative permativity of $CuSO_4$ is greater than that of H_2O. Because capacitance is a function of relative permittivity, the composition with the greater relative permittivity will produce a larger capacitance value. At a temperature of 0°C, H_2O has the greater relative permittivity and thus produces a larger capacitance value, whereas for each temperature after, $CuSO_4$ has the greater relative permittivity and thus produces the larger capacitance value.

Upon analysis of 3D surface plots comparing global capacitance, water tree AR, and temperature at different water tree depths, it was determined that capacitance decreases with increasing water tree AR, with the effect being fairly insignificant but more profound at greater water tree depths. Because the only other noticeable relationships from these surface plots is that which was already observed in Figures 22 through 24, they are not presented in this thesis.

5.4 Global Resistance

Figures 25 and 26 show the logarithm of the cable's global resistance versus water tree depth for compositions of H_2O and $CuSO_4$, respectively. A base-10 logarithmic transformation was applied to the global resistance measurements in order to better visualize the changes occurring across the simulated temperature and depth ranges.

The global resistance is defined as the total measure of resistance for the entire system being simulated. As with the capacitance measurements, the AR of the water tree region is equal to six and left constant, while the temperature of the cable is varied from 0 to 200°C in increments of 20°C. The Electric Currents physics branch and Stationary study type in COMSOL, which assume steady current flow and a static electric field, were used to calculate the global resistance at each temperature and water tree depth percentage. In comparison to those studies that used XLPE as the insulation material, the global resistance results presented in this thesis using EPR exhibit a similar trend with respect to water tree depth [52,80].

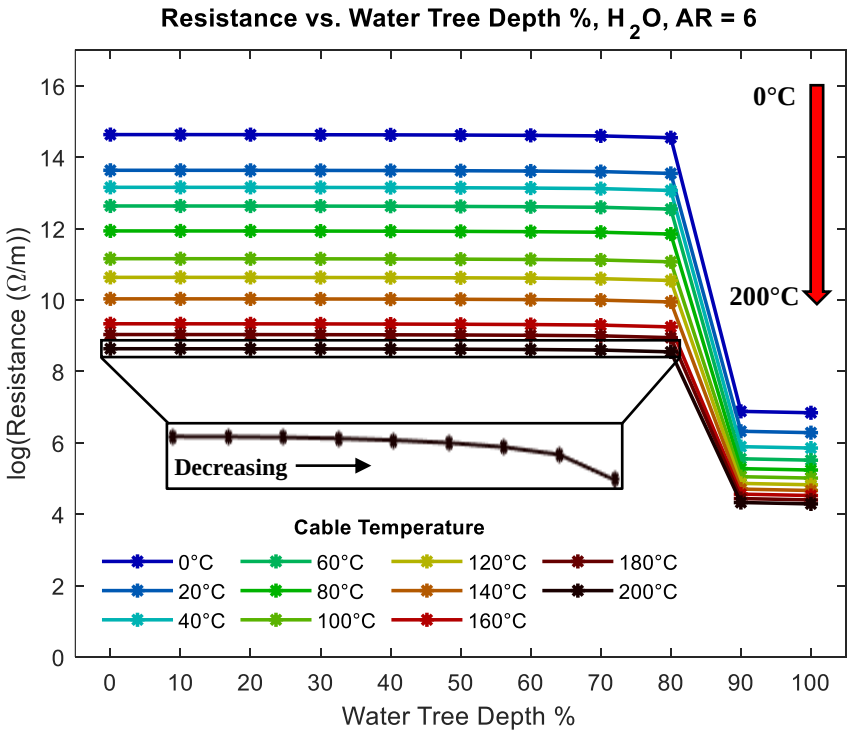

Figure 25. Logarithmic resistance versus water tree depth using H_2O. The arrow denotes the direction of temperature increase corresponding to the order of data sets.

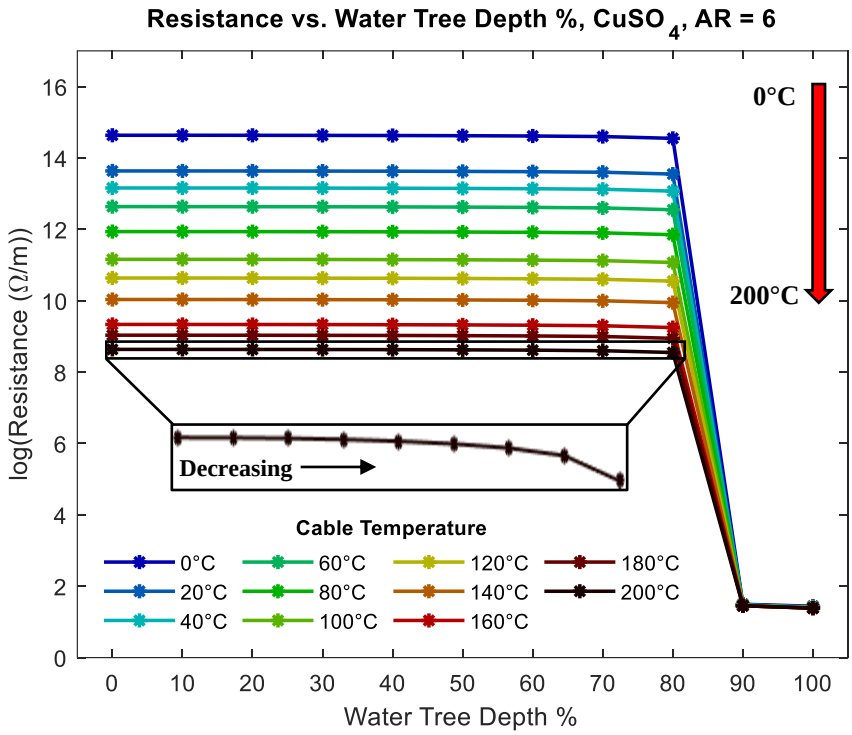

Figure 26. Logarithmic resistance versus water tree depth using $CuSO_4$. The arrow denotes the direction of temperature increase corresponding to the order of data sets.

For both compositions, it is observed that the resistance of the system is relatively constant up to a water tree depth of 80%. In actuality, the resistance in this depth range is decreasing for each temperature, but not to a significant extent. Between 80 and 90% depth, there is a sudden decrease in resistance followed by a slight decrease between 90 and 100% depth. In the depth range of 10 to 80%, the water tree is confined completely inside the insulation and thus is unable to act as a pathway for the flow of electrical current. Upon reaching a depth of 90%, the water tree has partially entered the area containing the conductor shield, which is made from a semi-conductive material bonded around the charged conductor. The connection between the semi-conductive conductor shield and the water tree creates a pathway for the flow of leakage current out of the

conductor, which produces a noticeable reduction in the resistance of the system. The system's resistance is further reduced as the water tree grows to a depth of 100% and completes the connection between the conductor and the insulation. As shown for both compositions, the decrease in resistance between 90 and 100% is noticeably less than the decrease that occurred as the water tree grew from 80 to 90% depth.

Temperature is observed to have a noticeable effect on the resistance of the system, as shown in Figures 25 and 26. For both compositions, the following relationship between temperature and resistance is observed: as temperature increases, the overall resistance of the system decreases. This is explained when considering how resistance, electrical conductivity, and temperature are related. There is a direct relationship between temperature and electrical conductivity, and an inverse relationship between electrical conductivity and resistance. Combining these two relationships yields the initial observation of decreasing resistance as temperature increases.

The magnitude of change in resistance as temperature increases is similar for both compositions up to a water tree depth of 80%. Between 80 and 100% depths is where the two compositions vary in this regard. For the H_2O composition in this depth range, the relationship between magnitude of change in resistance and temperature is similar to that which is found between 10 and 80% depth. In contrast, the $CuSO_4$ composition in the depth range of 80 to 100% exhibits a noticeably different relationship than that found between 10 and 80% depth. When comparing the percent differences in resistance between 0 and 200°C for water tree depths of 90 and 100%, there exists a significant difference between the compositions. The resistance measured using H_2O decreased by

approximately 60% as temperature increased from 0 to 200°C at both 90 and 100% depths, whereas the resistance using $CuSO_4$ decreased by only 1.4% and 2.2% for the same temperature increase at 90 and 100% depths, respectively. A possible explanation for this variation is found when comparing the electrical conductivities of the two compositions. When compared to H_2O, the electrical conductivity of $CuSO_4$ is much greater on account of the presence of charged ions. For this reason, it is possible that the effect of temperature on the resistance is minimized for water tree compositions having significantly high electrical conductivities when they come within a certain distance of a charged body such as a cable's conductor.

Figure 27 shows the logarithm of the difference in the cable's resistance between the $CuSO_4$ and H_2O compositions versus water tree depth. There is little to no difference in resistance between the compositions in the depth range of 10 to 80%, but there is a noticeable difference between 80 and 100% depth. In this depth range, the resistance measured using a water tree composed of H_2O is greater than that of a water tree composed of $CuSO_4$, which corresponds to less leakage current flow. Additionally, the resistance difference in this depth range grows larger with decreasing temperature, with the largest difference occurring at 0°C and the smallest difference occurring at 200°C. These observations are confirmed when considering the results shown in Figures 25 and 26 which show that for H_2O in this depth range, the resistance was greater at lower temperatures, and for $CuSO_4$ there was minimal difference across the simulated temperature range.

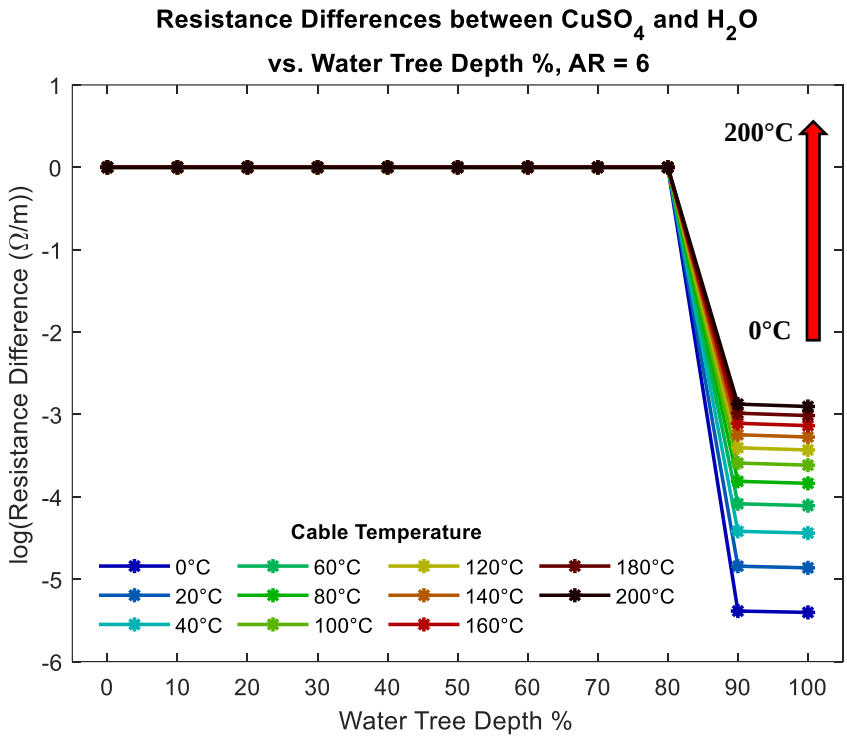

Figure 27. Logarithmic difference in resistance between $CuSO_4$ and H_2O versus water tree depth. The arrow denotes the direction of temperature increase corresponding to the order of data sets.

Analysis of 3D surface plots comparing global resistance, water tree AR, and temperature at different water tree depths yielded the conclusion of a direct relationship between resistance and AR, with the effect being fairly insignificant at depths between 10 and 80%. Because the only other noticeable relationships from these surfaces plots is that which was already observed in Figures 25 through 27, they are not presented in this thesis. The two water tree depths that provide the most significant change in resistance as water tree AR increases are 90 and 100%, which are shown for both compositions in Figure 28.

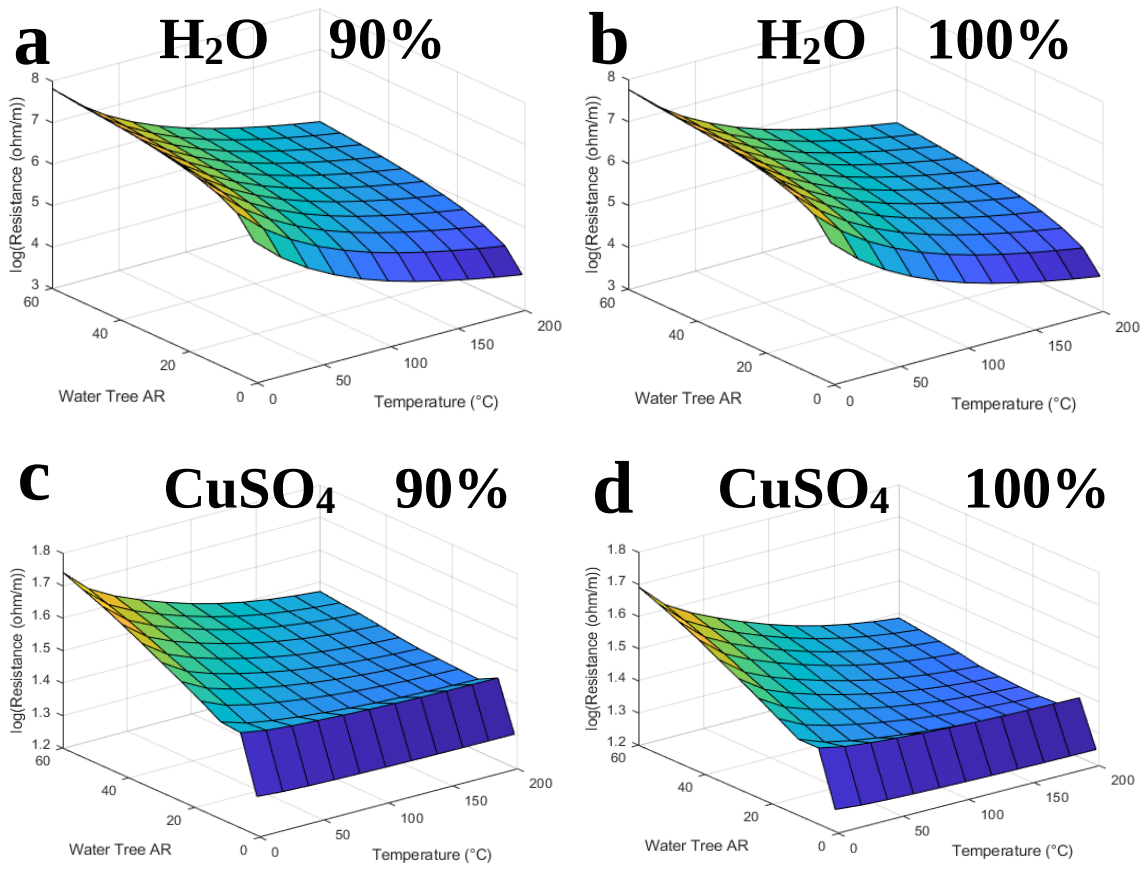

Figure 28. Surface plots comparing logarithmic resistance, water tree AR, and temperature for (a) H_2O composition at 90% depth; (b) H_2O composition at 100% depth; (c) $CuSO_4$ composition at 90% depth; (d) $CuSO_4$ composition at 100% depth.

For each composition at both 90 and 100% water tree depths, there exists a noticeable relationship between resistance and water tree AR, which is that increasing water tree AR produces an increase in resistance. This relationship is explained when considering the effect narrowing of the water tree region has on the amount of leakage current flowing out of the conductor. As AR increases and the water tree narrows, the amount of area inside the conductor shield that the water tree occupies decreases and thus the pathway for the flow of leakage current is made smaller. With less leakage current

flowing out of the conductor, the global resistance of the system does not decrease as significantly as it does when a larger water tree with a smaller AR is present.

5.5 Voltage and Electric Field Distribution

Another way to examine the effects of water tree degradation is by observing how the voltage and electric field distribution of a cable changes with increasing water tree depth, which is known to occur [38,53,54,80]. Shown in Figure 29 is the voltage and electric field distribution for the cable model in the absence of water treeing. The colors displayed on the surface plot correspond to the voltage reading throughout the cable, and the arrows represent the electric field. The voltage reading is at a maximum value of 15 kV in the area containing the conductor and conductor shield, and it slowly decreases until reaching a value of zero at the grounded metallic shield. By acting as a Faraday cage, the metallic shield confines the electric field inside the cable and prevents any voltage buildup in areas outside the cable. Since the electric field consists of both a magnitude and direction at any given location, it can be defined as a vector quantity and is thus represented by an arrow with a length proportional to the strength of the electric field at that location. The direction of the electric field vectors is identical to that of the flow of electrical current, which is from the charged conductor to the grounded metallic shield.

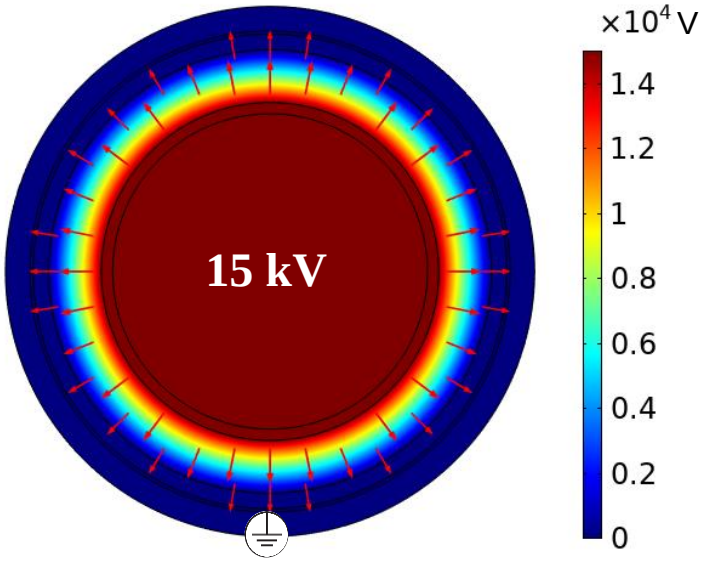

Figure 29. Voltage and electric field distribution for the simulation model without water treeing. The color bar on the right side is a measure of voltage and is in units of volts.

When a water tree enters the insulation, the cable's voltage and electric field distribution begins to distort. The primary distortionary effects are a disruption of the normal flow of voltage through the insulation, and a change in the intensity and direction of the electric field particularly in the area surrounding the water tree region. The forthcoming plots provided in Figures 30 through 39 visually show these distortionary effects using various parameter values and either H_2O or $CuSO_4$ as the water tree composition. These parameters, specifically water tree depth, water tree AR, operating frequency, and temperature, are varied to determine what effect if any they have on the rate of water tree degradation. To best represent the changes that are occurring, only a subset of values from each parameter are used to generate the plots provided in this thesis:

- Water Tree Depth: 10%; 50%; 70%; 90%; and 100%
- Water Tree AR: 6; 60
- Operating Frequency: 0.01 Hz; 60 Hz; 10,000 Hz; and 1,000,000 Hz
- Temperature: 0°C; 200°C

When distribution plots using an operating frequency of 60 Hz were compared to those at 800 Hz, no change was visually apparent. For this reason, distribution plots at 800 Hz are excluded from this thesis. Likewise for temperature, no change was visually apparent as temperature increased in 20°C increments. For this reason, the temperature extremes of 0 and 200°C, which exhibit the greatest difference in distribution among the temperature combinations, were selected for inclusion in this thesis.

Trends and observations with regards to distortion of the cable's voltage and electric field distribution are presented in the following sections. Each section is devoted to a single water tree depth using the parameter values previously given. In addition to describing the effects of each parameter being studied, a discussion regarding the overall trend in distortion as water tree depth increases is provided.

5.5.1 Distribution Distortion at 10% Water Tree Depth

Figures 30 and 31 show voltage and electric field distribution plots at a water tree depth of 10% for H_2O and $CuSO_4$ compositions. For these plots, along with those provided in Figures 32 through 39, an elliptical shape has been added around the region containing the water tree for better visibility. At this depth, the water tree is visibly present inside the insulation but has no significant distortionary effect on the voltage and electric field distribution. When comparing water tree ARs, it is observed that there is

slightly more voltage distortion for an AR of six versus that for an AR of 60. This observation is noticeable when comparing the first and second rows, and third and fourth rows, of Figures 30 and 31. Because the water tree with an AR of six occupies more area inside the insulation, it is expected that it will have a greater distortionary effect compared to the other AR. In addition to the observable voltage distortion, there is also a slight directional change of the electric field vectors closest to the water tree region. Instead of pointing directly at the grounded source, these vectors are now angled slightly inwards toward the water tree. Although there is no noticeable change in length of these vectors, the slight directional change indicates that distortion has begun to occur. Because the water tree has only just started to grow, this directional change is barely visible, but more so in the plots for an AR of six. As for the other parameters, there is no visible change in the cable's distribution when temperature, frequency, and composition are contrasted. Nonetheless, these parameters do cause some change in the distribution, with the primary effects being increased voltage distortion and an enhanced electric field around the water tree region.

As the water tree grows from a depth of 10 to 40%, the amount of observable distortion in the voltage and electric field distribution, particularly in the area inside and around the water tree region, continues to increase. To limit redundant observations, plots in this depth range are not presented in this thesis. Instead, the next section will examine the cable's distribution after the water tree has grown to a depth of 50%.

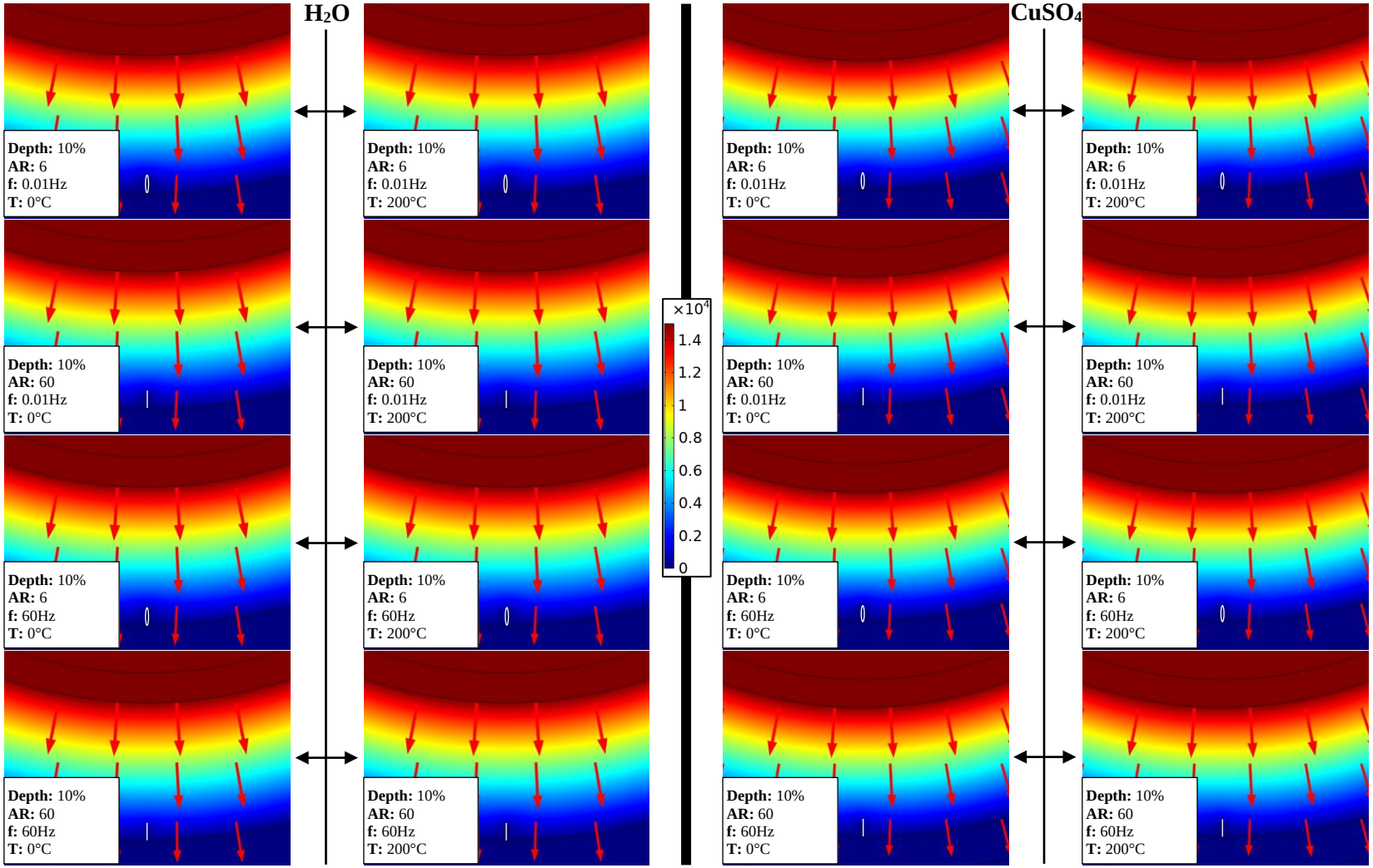

Figure 30. Voltage and electric field distribution plots at 10% water tree depth and frequencies (“f”) of 0.01 and 60 Hz.

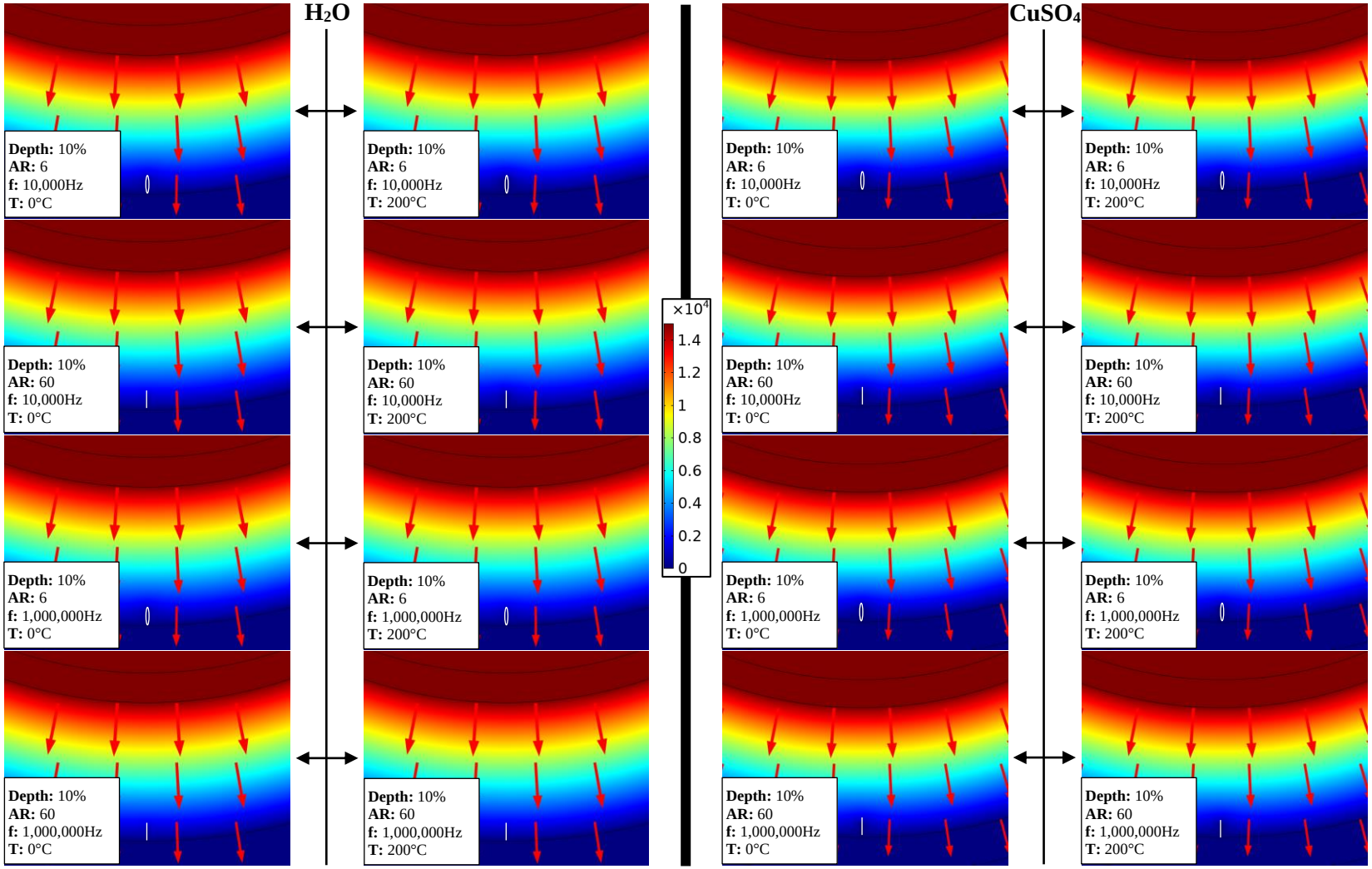

Figure 31. Voltage and electric field distribution plots at 10% water tree depth and frequencies ("f") of 10,000 and 1,000,000 Hz.

5.5.2 Distribution Distortion at 50% Water Tree Depth

Now that the water tree has grown a considerable distance through the cable, significant distortionary effects are beginning to occur. When the water tree was examined at 10% depth, the distortionary effects were present but insignificant due to the small size of the water tree. Because of this, the effects of changing water tree AR, frequency, and temperature were not readily apparent on the distribution plots. Having reached a depth of 50%, the effects of these parameters are now more visually apparent.

Figures 32 and 33 show voltage and electric field distribution plots at a water tree depth of 50% for H_2O and $CuSO_4$ compositions. Compared to the previous distribution plots at 10% depth, these plots show a significant change in voltage distortion and a noticeable increase in electric field intensity in the region occupied by the water tree. When comparing water tree ARs at each frequency, there is noticeably more voltage distortion in the plots containing a water tree with an AR of six because of the larger area it occupies in the cable. Because of its contact with the grounded metallic shield, the voltage inside and around the water tree is approximately zero.

At a frequency of 0.01 Hz, there is no noticeable difference in voltage or electric field distortion with changing temperature and water tree composition. For each plot using this frequency, the electric field vectors around the water tree have changed direction again and are now pointed directly inward towards the region occupied by the water. This coincides with a further increase in electric field intensity around the water tree region.

At a frequency of 60 Hz, there is no noticeable difference in voltage or electric field distortion with changing temperature and water tree composition for an AR of six. This conclusion also applies for $CuSO_4$ using an AR of 60 at both temperatures, but not for H_2O under the same conditions. The distributions plots for H_2O show noticeably less voltage distortion and more outward-pointing electric field vectors at 0°C compared to 200°C. This is the first visual indication that temperature influences the distortion of the voltage and electric field distribution. With regards to frequency, there is no noticeable difference in distortion for both compositions as frequency increases from 0.01 to 60 Hz.

At a frequency of 10,000 Hz, the trend of increasing temperature producing more voltage distortion is now observed for H_2O using both water tree ARs. In addition, at this frequency and composition for a water tree with an AR of 60, it is observed that the electric field vectors are more inward pointing for a temperature of 200°C but not for 0°C. This observation indicates that the electric field is less intense around the water tree at 0°C compared to 200°C. There is also noticeably less voltage distortion at this frequency for a water tree AR of six and temperature of 0°C compared to the previous frequency and same parameter values. This is the first visual indication that frequency influences the distortion of the voltage and electric field distribution, at least for H_2O. When observing the plots for $CuSO_4$ at this frequency, there is still no noticeable difference in voltage or electric field distortion with changing temperature and water tree AR. Additionally, there is no noticeable difference in distortion for $CuSO_4$ as frequency increases.

At a frequency of 1,000,000 Hz for H_2O, the same trend between water tree AR and distortion as was found for the previous frequency exists, but the opposite trend is observed between temperature and distortion. There is slightly less voltage distortion at 200°C compared to 0°C, which is contrary to the trend of the previous frequency which was that increasing temperature produces more voltage distortion. As with the previous frequency for $CuSO_4$, no noticeable difference in voltage or electric field distortion exists with changing temperature and water tree AR. Additionally, like the previous frequency, there is no noticeable change in distortion for $CuSO_4$ as frequency increases.

For this depth, the following overall trends are observed for H_2O: as water tree AR and frequency increase, voltage distortion decreases, and the electric field vectors become more outward pointing from the water tree, which indicates a reduction in the electric field intensity; as temperature increases, voltage distortion appears unchanged at frequencies of 0.01 and 60 Hz, with an increase and decrease in distortion observed at frequencies of 10,000 and 1,000,000 Hz, respectively. As for the trend between temperature and electric field distortion, the electric field vectors tend to be more inward pointing with increasing temperature, with the exception being those at a frequency of 1,000,000 Hz. Although the vectors around the water tree do no change significantly in length, the directional change indicates an increasing electric field intensity in that area. As for $CuSO_4$, no noticeable trends in distortion between temperature, water tree AR, and frequency were found to exist. In the next section, the voltage and electric field distributions using the same parameters and values at a water tree depth of 70% will be observed.

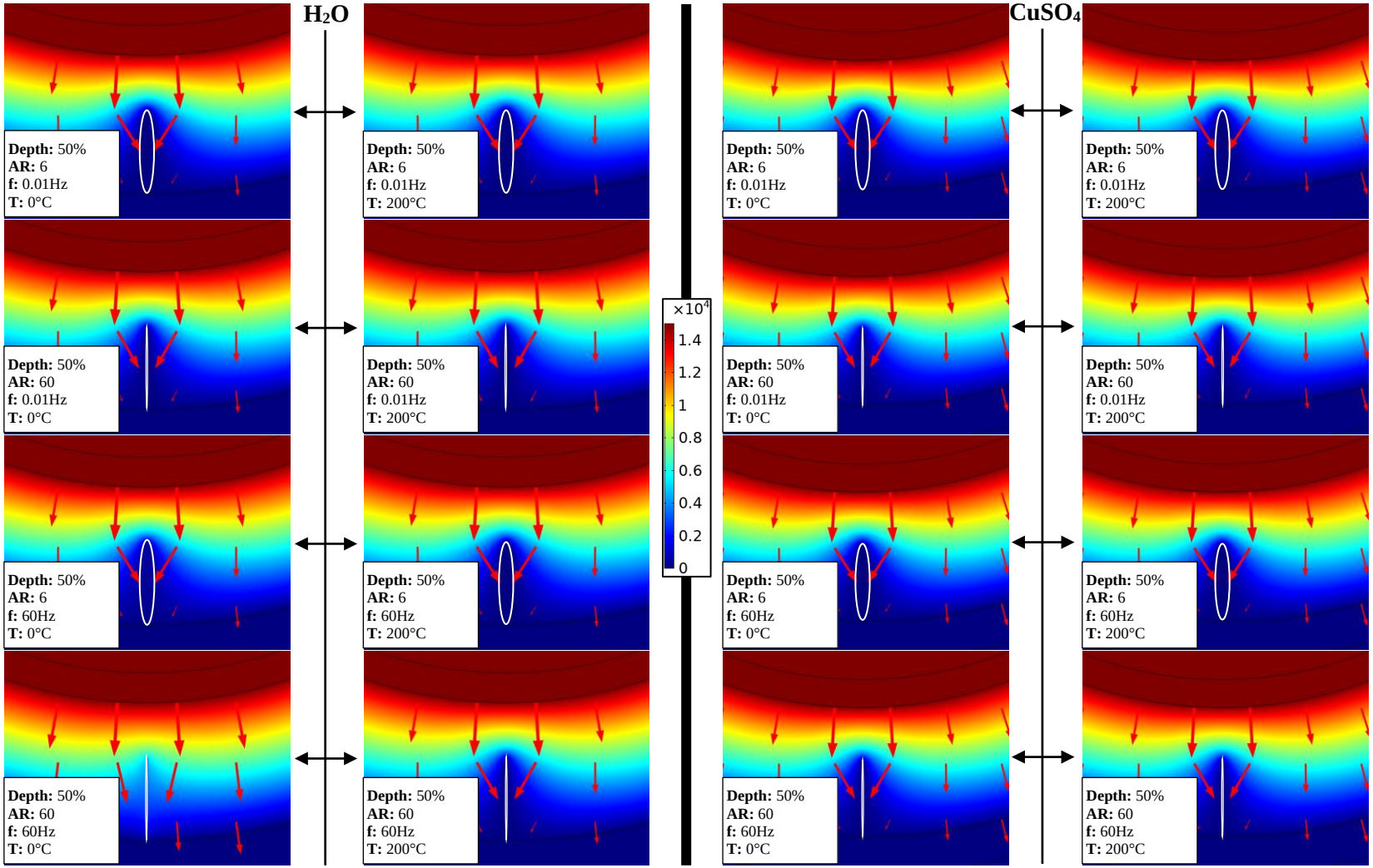

Figure 32. Voltage and electric field distribution plots at 50% water tree depth and frequencies (“f”) of 0.01 and 60 Hz.

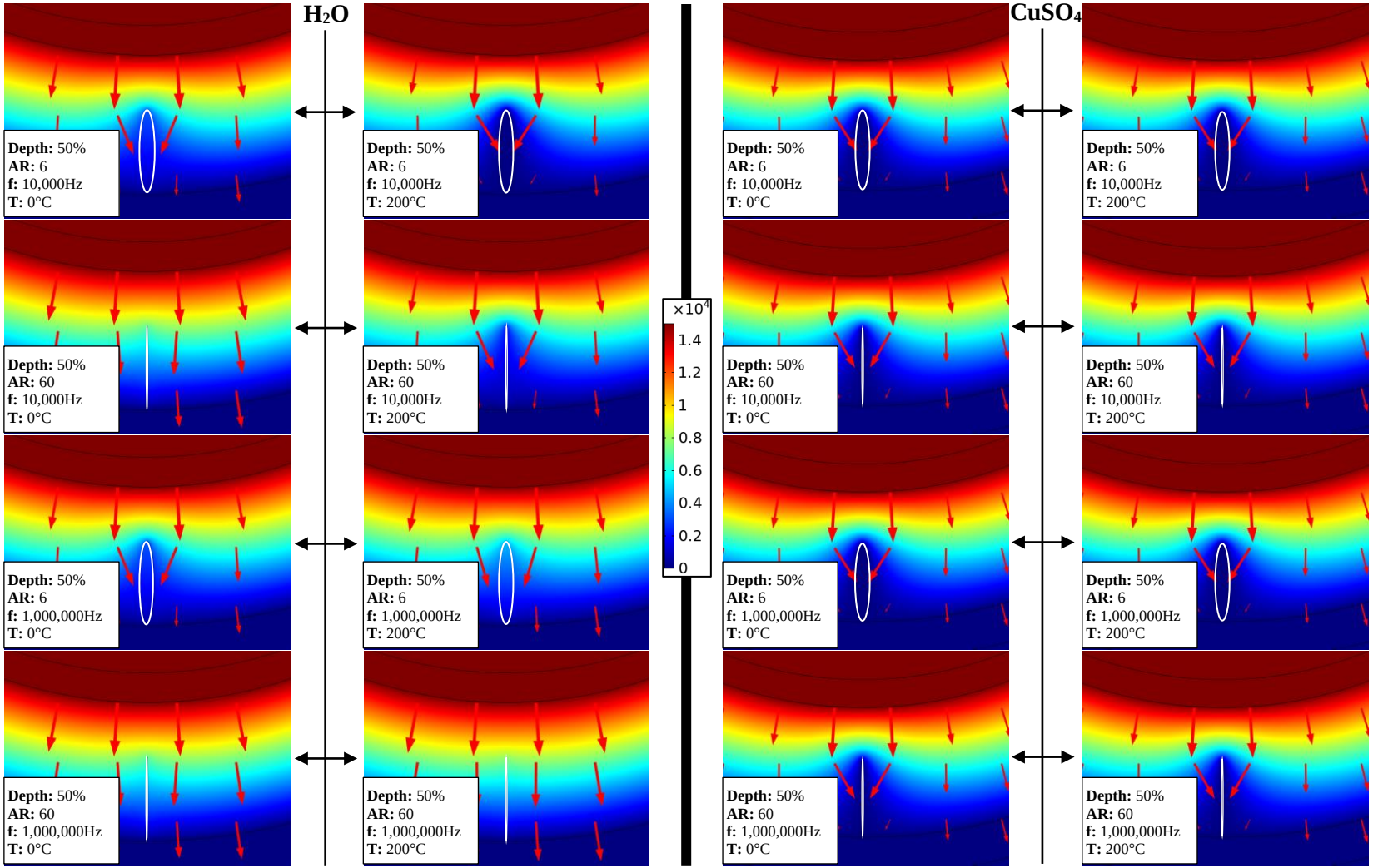

Figure 33. Voltage and electric field distribution plots at 50% water tree depth and frequencies ("f") of 10,000 and 1,000,000 Hz.

5.5.3 Distribution Distortion at 70% Water Tree Depth

Figures 34 and 35 show voltage and electric field distribution plots at a water tree depth of 70% for H_2O and $CuSO_4$ compositions. Compared to the previous distribution plots at 50% depth, the general observation is that the amount of voltage and electric field distortion has increased because of the water tree's continued advancement through the cable. Trends similar to those at 50% depth are also observed here: as water tree AR and frequency increase, voltage distortion decreases, and the electric field vectors become more outward pointing from the water tree; as temperature increases, voltage distortion appears unchanged at a frequency of 0.01 Hz, increases at frequencies of 60 and 10,000 Hz, and decreases at a frequency of 1,000,000 Hz. As for the trend between temperature and electric field distortion, the electric field vectors tend to be more inward pointing with increasing temperature, with the exception being a frequency of 1,000,000 Hz. With regards to the plots using $CuSO_4$, there is still no noticeable difference in voltage or electric field distortion as the values of the parameters are changed.

When examining the electric field vectors distributed throughout the cable, it is observed that the vector lengths are shorter than those of previous depths. Based on the relationship between vector length and electric field magnitude, this appears indicative of a reduction in electric field intensity. On the contrary, the electric field intensity around the water tree area closest to the conductor has increased to such an extent that it makes the surrounding areas appear less intense. COMSOL uses automatic vector scaling when generating distribution plots, which leads to the appearance of a reduction an electric field intensity at this depth when in fact the opposite is true.

When taking a closer look at the length and direction of the electric field vectors, it is observed that the maximum electric field intensity always occurs at the location where the water tree pole is present. This observation holds true regardless of water tree depth. As a result, the area of insulation surrounding the water tree pole will be the first to experience a permanent breakdown. Although the breakdown location cannot be visually observed on the voltage and electric field distribution plots, it can be inferred based on the length of the electric field vectors at the water tree pole compared to those in other areas of the cable. Using the first two rows of plots in Figure 35 as an example, it is observed that the electric field vectors at the water tree pole are much longer than those in other areas of the cable. Knowing that vector length is proportional to the strength of the electric field in that area, it is clear that electric field intensity is at a maximum at the water tree pole and thus permanent breakdown will first occur at that location.

Upon reaching a depth of 90%, the water tree partially enters the conductor shield and creates a pathway for the flow of leakage current out of the conductor. The flow of leakage current produces drastically different distortionary effects than those observed for previous depths when the water tree was completely enclosed inside the insulation. In the next section, the distortionary effects caused by the flow of leakage current will be visually observed using distribution plots at the same parameter values.

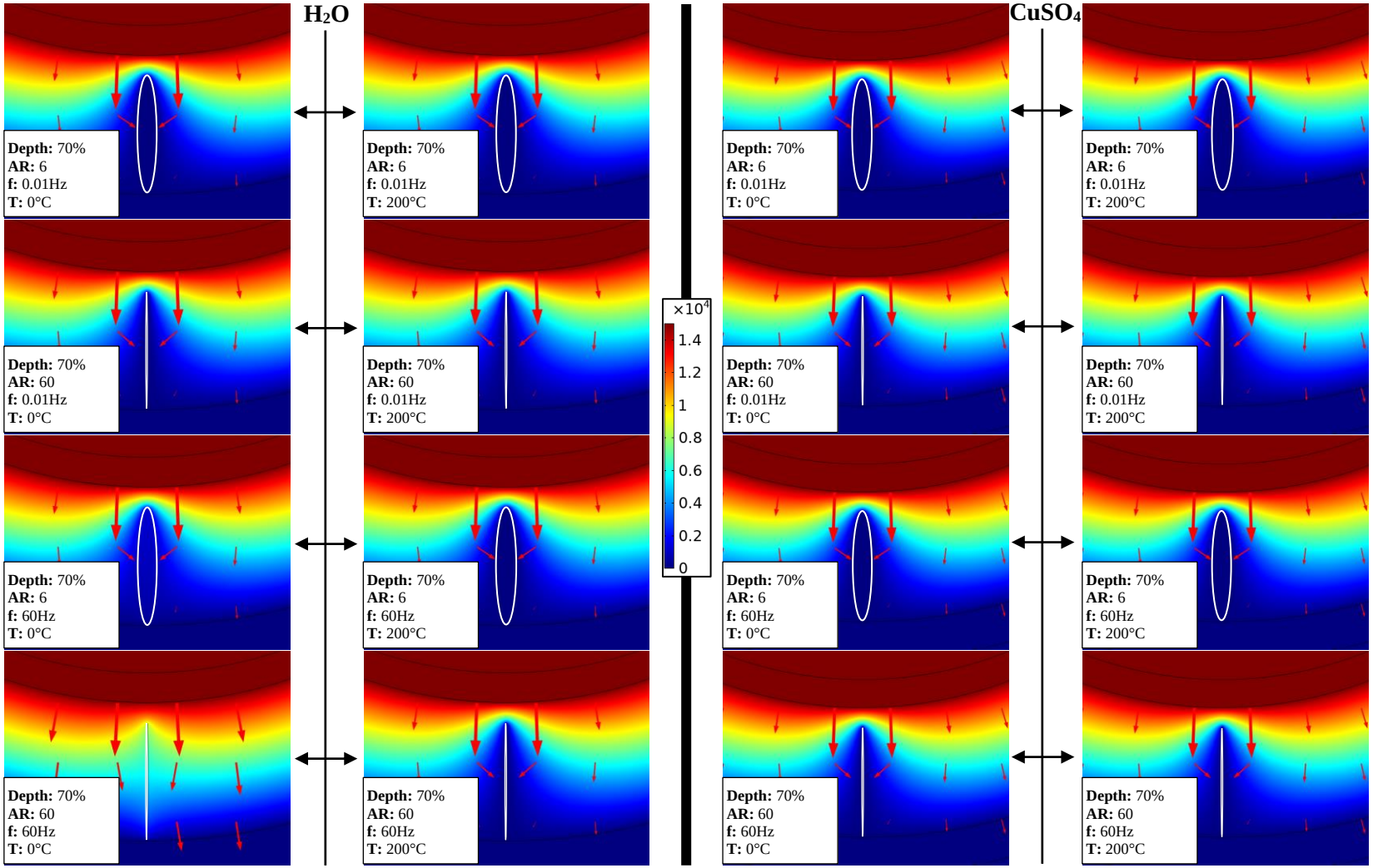

Figure 34. Voltage and electric field distribution plots at 70% water tree depth and frequencies (“f”) of 0.01 and 60 Hz.

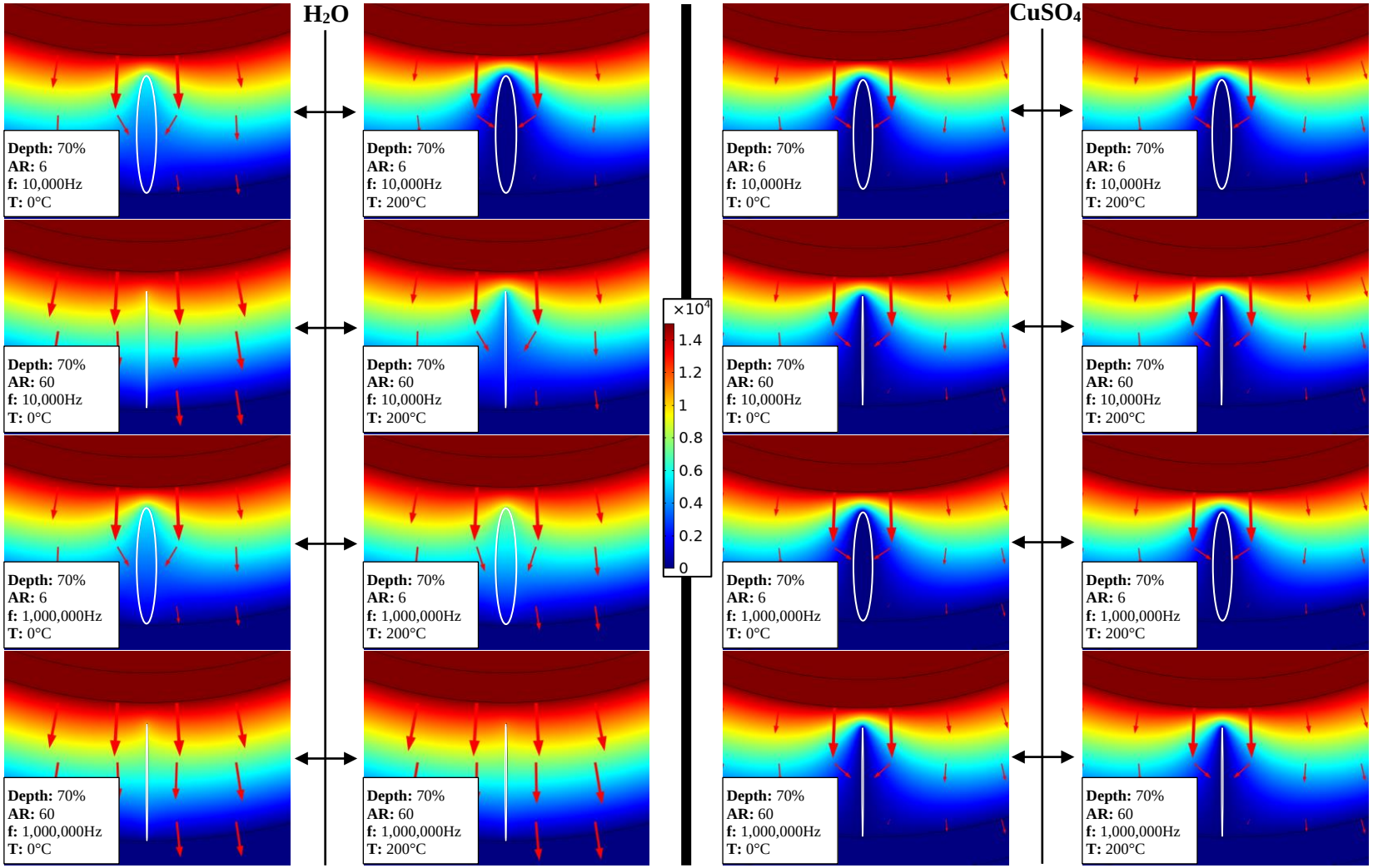

Figure 35. Voltage and electric field distribution plots at 70% water tree depth and frequencies ("f") of 10,000 and 1,000,000 Hz.

5.5.4 Distribution Distortion at 90% Water Tree Depth

Figures 36 and 37 show voltage and electric field distribution plots at a water tree depth of 90% for H_2O and $CuSO_4$ compositions. Up to this point, the water tree has been completely enclosed inside the insulation as it has grown closer to the conductor. Having now reached 90% depth, the water tree has partially entered the conductor shield, creating a pathway for the flow of leakage current out of the conductor. Compared to those at depths of 50 and 70%, each of the H_2O plots at 90% depth appear to exhibit significantly less voltage distortion at each combination of water tree AR, frequency, and temperature. There is very little observable difference between each of the H_2O plots at this depth, with the only noticeable relationships being the following: as water tree AR and frequency increase, voltage distortion decreases with no noticeable change in the length or direction of the electric field vectors surrounding the water tree region.

With each of the previous depths, the $CuSO_4$ plots showed no noticeable difference in voltage or electric field distortion as the values of the parameters changed. Now, having partially entered the conductor shield, trends between the distortionary effects and changing water tree AR and temperature can be observed. As water tree AR increases, voltage distortion decreases along with a minimal increase in length of the electric field vectors surrounding the water tree, with no noticeable directional change. As temperature increases, voltage distortion increases, with no noticeable change in length or direction of the electric field vectors. Compared to the previous depths, this distortion is no longer causing an approximate zero voltage inside and around the water tree, but an elevated voltage which correlates with a decrease in resistance and increase in

leakage current flowing out of the conductor. Additionally, there is an elevated voltage in the area where the insulation shield is connected to the water tree, which is also caused by the flow of leakage current. The increased voltage distortion produced by decreasing water tree AR and increasing temperature have the same explanations as those given in the previous discussion regarding global resistance: a larger water tree AR results in a narrower water tree region and thus a smaller pathway for the flow of leakage current, while a rising temperature increases the electrical conductivity of the composition, thus creating a decrease in resistance and increase in leakage current. With respect to frequency, there is no noticeable change in voltage or electric field distortion as frequency increases.

As previously noted, a composition having a greater electrical conductivity will produce a more significant decrease in resistance and thus a larger amount of leakage current. Because $CuSO_4$ has a greater electrical conductivity than H_2O, there is a greater amount of leakage current flowing through the water tree and thus more distortion of the voltage distribution when this composition is present. Although the H_2O plots in Figures 36 and 37 exhibit significantly less voltage distortion than previous depths, there is still leakage current flowing through the water tree at this depth, as indicated by Figure 25, but it is not significant enough to be visualized on the distribution plots. As the water tree grows further through the conductor shield, these trends in distortion between the compositions will continue to hold. This will be further examined in the next section where the water tree grows to a depth of 100% and completes the connection between the conductor and the insulation.

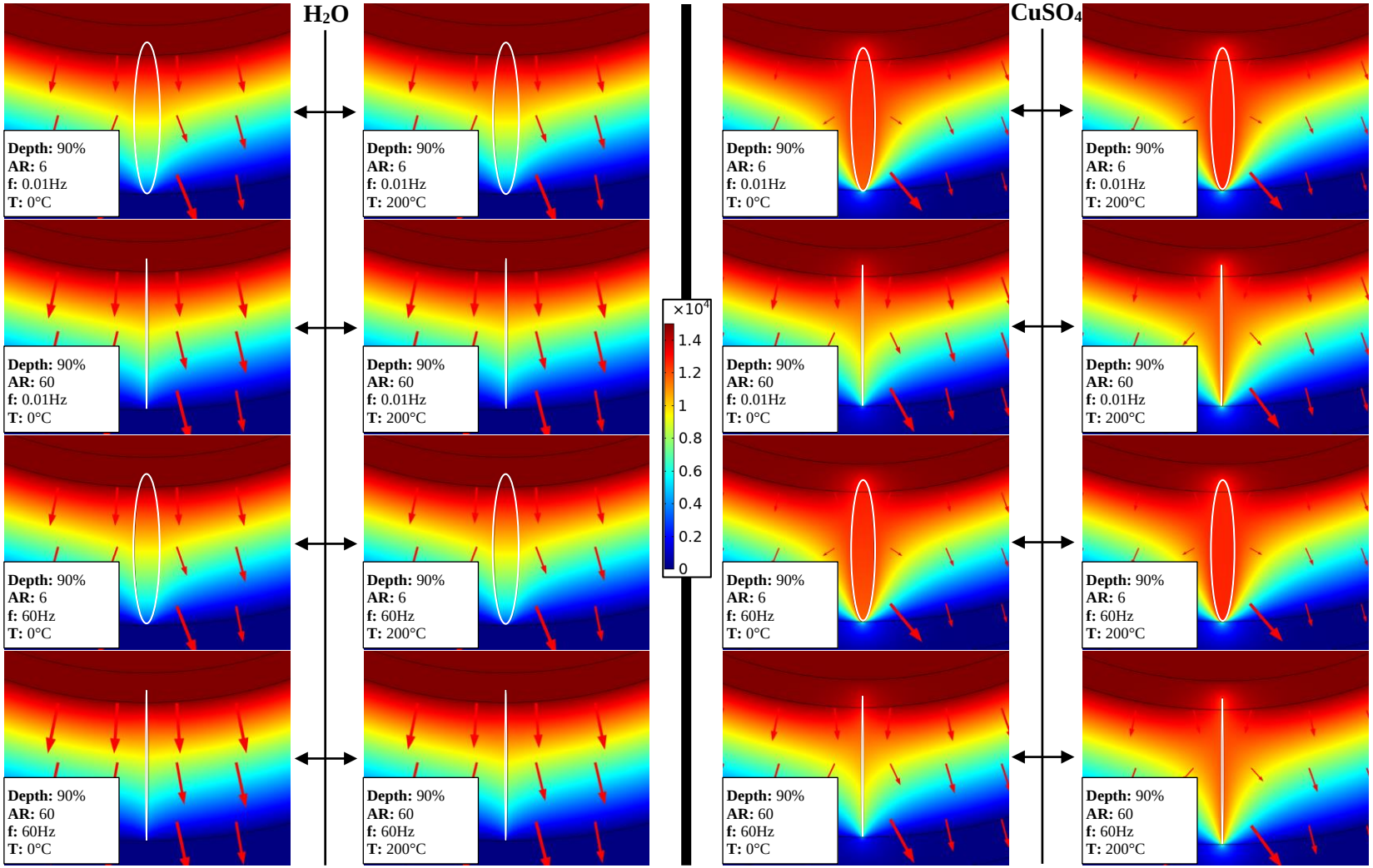

Figure 36. Voltage and electric field distribution plots at 90% water tree depth and frequencies (“f”) of 0.01 and 60 Hz.

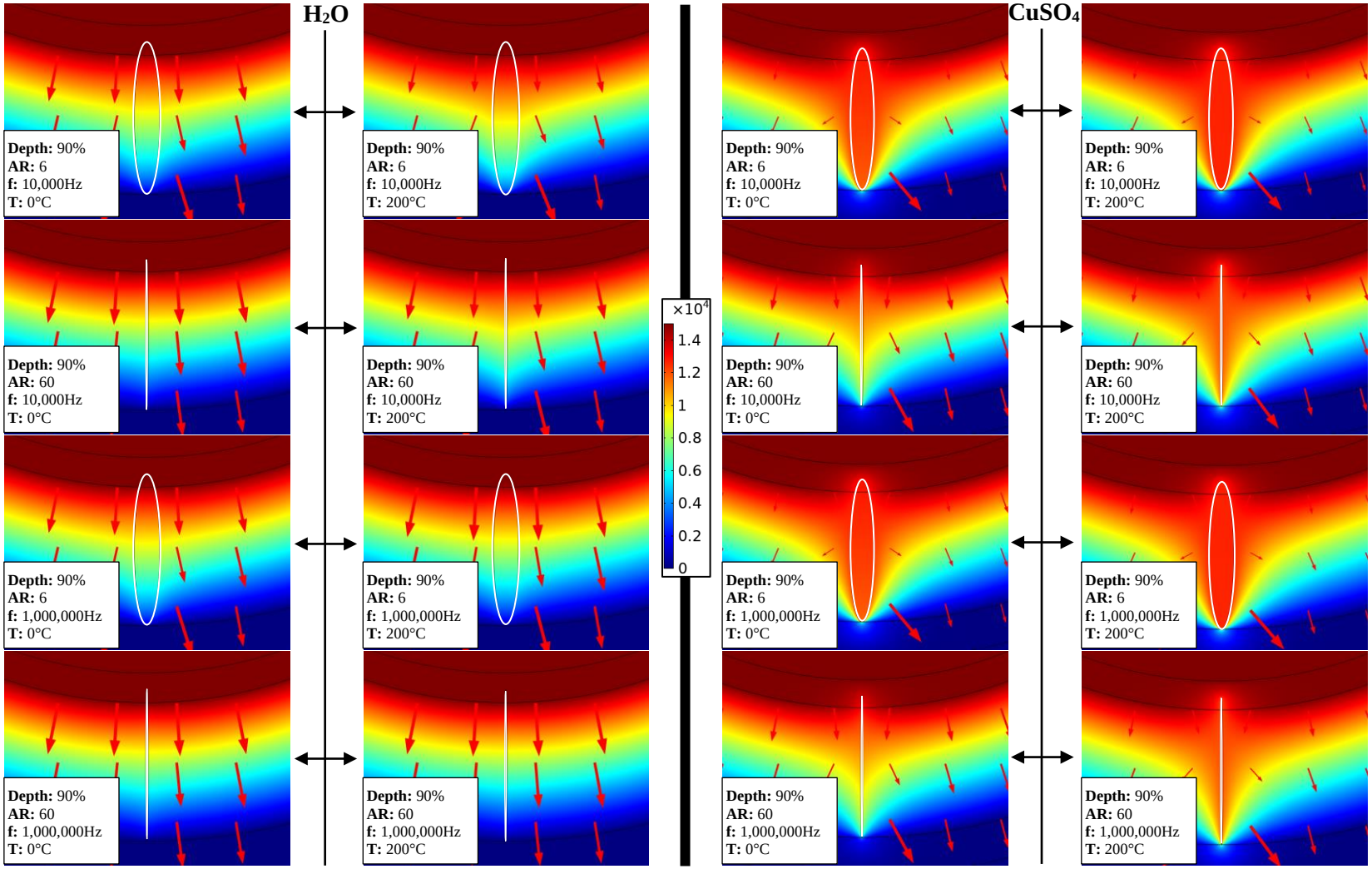

Figure 37. Voltage and electric field distribution plots at 90% water tree depth and frequencies ("f") of 10,000 and 1,000,000 Hz.

5.5.5 Distribution Distortion at 100% Water Tree Depth

Figures 38 and 39 show voltage and electric field distribution plots at a water tree depth of 100% for H_2O and $CuSO_4$ compositions. At this depth, the water tree has now grown completely through the conductor shield and is in contact with the charged conductor. Because of the connection between water tree and conductor, the amount of leakage current flowing out of the conductor has increased which correlates with a further decrease in the resistance of the system. When observing the distribution plots for H_2O, it can be stated that the same parameter trends found at 90% depth still apply: as water tree AR increases, there is slightly less voltage distortion and a minimal increase in length of the electric field vectors; as temperature increases, there is no noticeable difference in voltage distortion, and no noticeable change in the length or direction of the electric field vectors; as frequency increases, voltage distortion decreases with only a minimal reduction in length of the electric field vectors.

Similarly, the same parameter trends found at 90% depth for $CuSO_4$ also still apply: as water tree AR increases, there is significantly less voltage distortion because of the narrowing of the water tree region, along with a minimal increase in length of the electric field vectors with no noticeable directional change; as temperature increases, voltage distortion increases with no noticeable change in length or direction of the electric field vectors; as with the previous water tree depths, there is no noticeable difference in voltage or electric field distortion as frequency increases. Additionally, the elevated voltage in the insulation shield that was observed at 90% depth is also present for the $CuSO_4$ distribution plots at this depth.

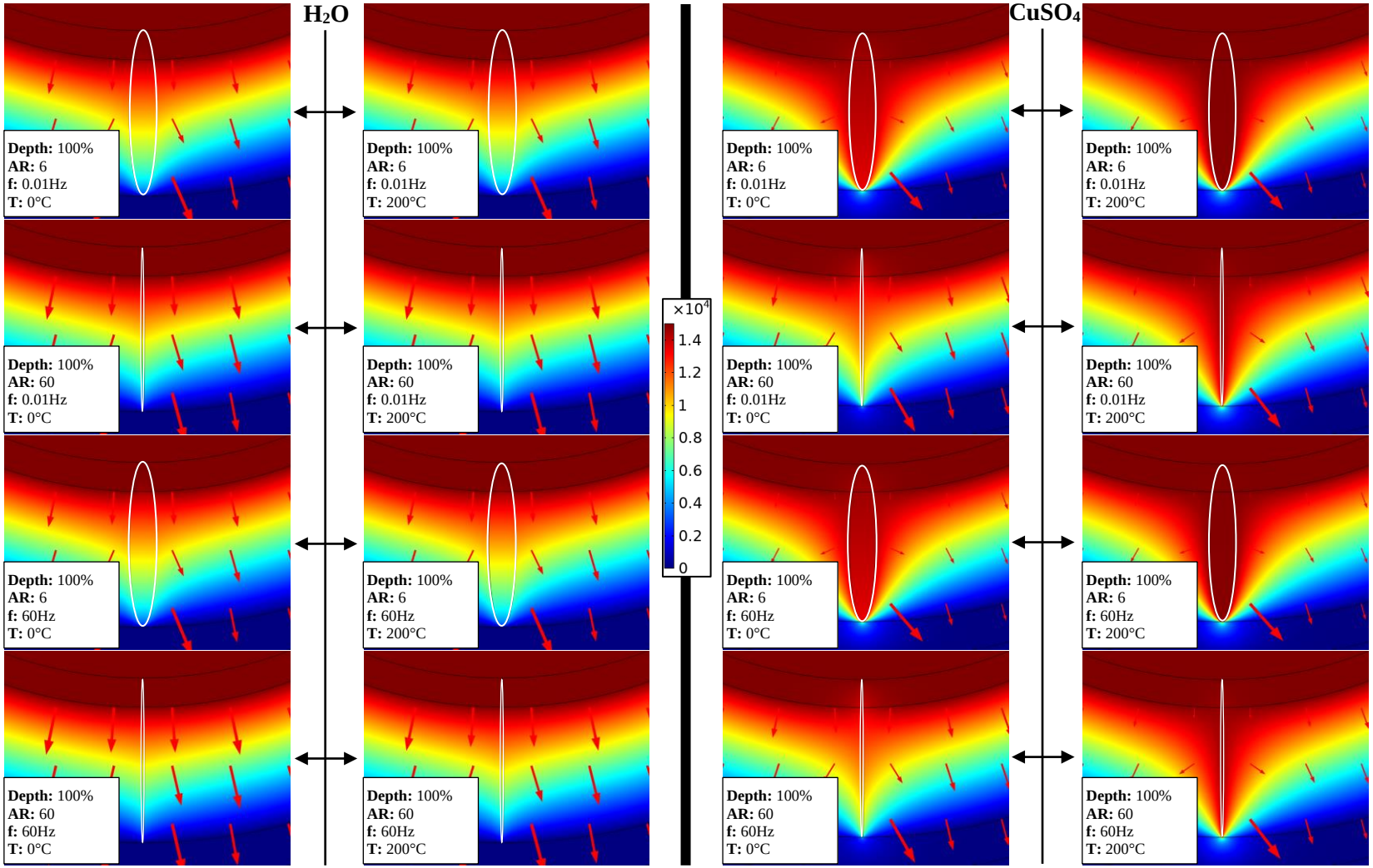

Figure 38. Voltage and electric field distribution plots at 100% water tree depth and frequencies (“f”) of 0.01 and 60 Hz.

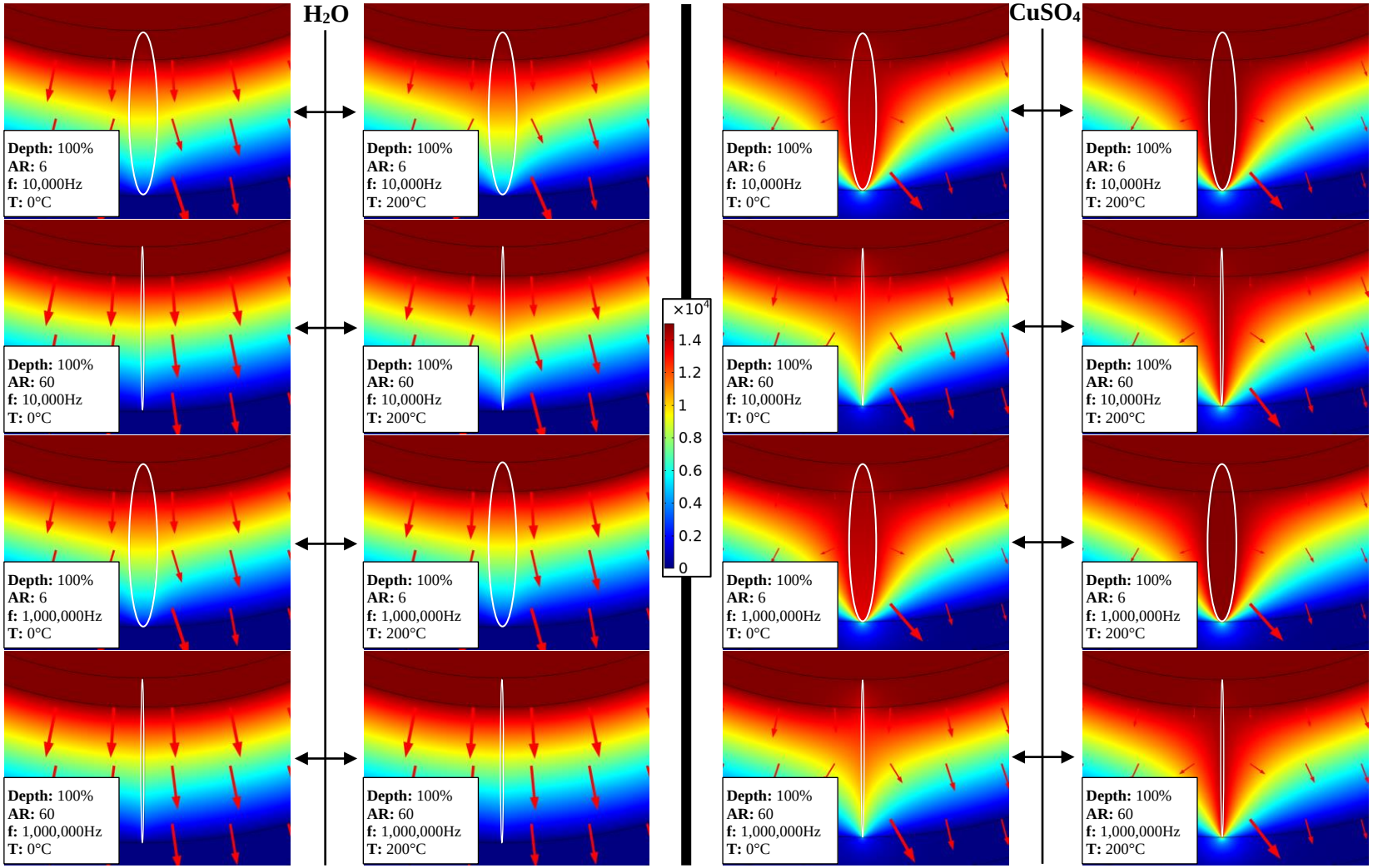

Figure 39. Voltage and electric field distribution plots at 100% water tree depth and frequencies ("f") of 10,000 and 1,000,000 Hz.

5.5.6 Summary of Major Observations

This section presented voltage and electric field distribution plots for H_2O and $CuSO_4$ compositions at varying water tree ARs, frequencies, and temperatures for depths of 10, 50, 70, 90, and 100%. The following is a list of major observations found through visual examination of the distribution plots, and extrapolation for the entire range of water tree depths:

- For both compositions, distribution distortion increases as the water tree grows from a depth of 10 to 80%, with the effects being an approximate zero voltage inside and around the water tree region, and an increase in the electric field intensity in the same area. These relationships are identical to those which are found when using XLPE as the insulation material [80].
- Between depths of 10 and 80%, as water tree AR increases, voltage and electric field distortion for both compositions decreases because of the reduction in area being occupied by the water tree region.
- Between depths of 10 and 80%, as frequency increases, voltage and electric field distortion for H_2O decreases; frequency has no noticeable effect for $CuSO_4$.
- Between depths of 10 and 80%, as temperature increases, voltage and electric field distortion for both compositions increases, with this trend being visually apparent only at certain frequency and depth combinations for H_2O. The exception to this trend for H_2O occurs at a frequency of 1,000,000 Hz where the opposite is observed: as temperature increases, voltage and electric field distortion appears to decrease.

- For both compositions at depths of 90 and 100%, the water tree has entered the conductor shield and created a pathway for the flow of leakage current out of the conductor. The flow of leakage current creates an elevated voltage inside and around the water tree, with the effect being more apparent for $CuSO_4$ because of its greater electrical conductivity.
- For H_2O at depths of 90 and 100%, voltage distortion is less compared to previous depths. At both depths, the following trends exist: as water tree AR increases, there is slightly less voltage distortion and a minimal increase in length of the electric field vectors; as temperature increases, there is no noticeable difference in voltage distortion, and no noticeable change in the length or direction of the electric field vectors; as frequency increases, voltage distortion decreases with only a minimal reduction in length of the electric field vectors and no noticeable change in direction.
- For $CuSO_4$ at depths of 90 and 100%, noticeable distortion of the voltage distribution exists because of the leakage current flowing through the water tree. At both depths, the following trends exist: as water tree AR increases, there is significantly less voltage distortion because of the narrowing of the water tree region, along with a minimal increase in length of the electric field vectors with no noticeable directional change; as temperature increases, voltage distortion increases with no noticeable change in length or direction of the electric field vectors; there is no noticeable difference with increasing frequency.

5.6 Localized Specific Energy Absorption Rate

The effects of water tree degradation can be visualized when examining a cable's voltage and electric field distribution. As shown in the previous section, it is even possible to describe degradation trends by visual comparison of distortion of the cable's distribution at different environmental and operational conditions. That being said, attempting to quantify these effects and how they change with varying conditions is a difficult task using only a visual, qualitative assessment. Additionally, visual observation alone cannot identify specifically when permanent breakdown of the insulation occurs. As previously noted, permanent breakdown of the insulation first occurs at the pole of the water tree region closest to the conductor. Because the maximum electric field intensity occurs in this area, as shown in Figure 40 and verified in literature [49], it will be the first to exceed the breakdown strength of the insulation, thus resulting in a permanent breakdown of the material. Directly related to the electric field intensity is the specific energy absorption rate (SAR) experienced in this area of insulation, which this thesis uses as a measure of the rate of cable degradation caused by water treeing.

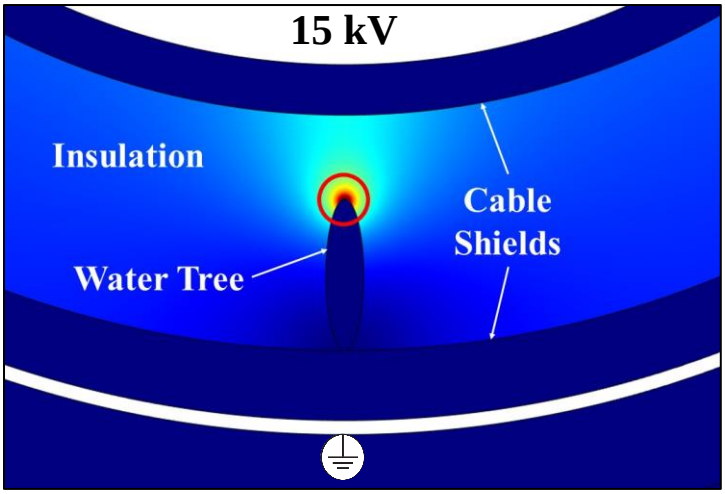

Figure 40. Maximum electric field intensity at the pole of the water tree region.

SAR can be defined generally as a measure of the amount of energy absorbed per unit of mass. It has traditionally been used to quantify the amount of energy absorbed by dielectric substances such as human tissue when exposed to a radio frequency electromagnetic field (RF-EMF). Common RF-EMF-emitting devices that are of particular interest to researchers using SAR in this manner include cellular phones, wireless fidelity routers, and magnetic resonance imaging machines [94,95]. AC electric cable insulation, which is a dielectric substance itself, also experiences the effects of a RF-EMF and therefore can be evaluated for degradation using SAR as a measurement.

Like human tissue, insulation is a lossy dielectric material, which implies both that the electrical conductivity of the material is greater than zero and that the material is not a good conductor of electricity [94,95]. Additionally, because the insulation material is non-ferromagnetic, it is said to be magnetically transparent with a relative permeability equal to one [95,97]. Given the fact that the insulation material is both a lossy dielectric and magnetically transparent, the SAR can be calculated using the following equation [95]:

$$SAR = \frac{\sigma |E|^2}{\rho} \tag{3}$$

where, σ is electrical conductivity at the water tree-insulation interface (S m^{-1}), E is electric field strength (V m^{-1}), and ρ is mass density of the dielectric material (kg m^{-3}).

Using this equation, localized SAR values at the pole of the water tree region were calculated for various water tree depths, water tree ARs, operating frequencies, and temperatures. To best represent the changes that are occurring, 3D surface plots comparing SAR, water tree AR, and temperature are provided for each water tree

composition at various operating frequencies. The following parameter values are represented by the 3D surface plots provided in this thesis:

- Water Tree Depth: 10%; 50%; 70%; and 80%
- Water Tree AR: 1; 6; 12; 18; 24; 30; 36; 42; 48; 54; and 60
- Operating Frequency: 0.01 Hz; 60 Hz; 800 Hz; 10,000 Hz; and 1,000,000 Hz
- Temperature: 0°C; 20°C; 40°C; 60°C; 80°C; 100°C; 120°C; 140°C; 160°C; 180°C; and 200°C

As with the voltage and electric field distribution plots in the previous section, only a subset of water tree depths will be shown in the 3D surface plots provided in this thesis. The water tree depths selected for surface plot representation are those that provide the most relevant information regarding breakdown of the insulation, and exhibit the most apparent relationship between the parameters being compared. Although water tree depths of 20, 30, 40, 60, 90, and 100% are excluded, the findings at these depths can be inferred when considering both where the water tree is located in the cable at any particular depth, and the general relationship between SAR and water tree depth, which are both discussed in the following section. Lastly, a base-10 logarithmic transformation was applied to the SAR measurements in order to better visualize the changes occurring across the simulated parameter ranges.

5.6.1 Connection between SAR, Water Tree Location, and Depth

Before observing and discussing the 3D surface plots, the connection between SAR, water tree location, and water tree depth must first be understood. In addition to being able to infer findings at excluded water tree depths, developing an understanding of

this connection will make the 3D surface plots and their differences with respect to each other more easily understood. To develop this understanding, SAR will be compared to water tree depth using constant values for water tree AR, frequency, and temperature.

Figure 41 shows the comparison between logarithmic SAR and water tree depth for both H_2O and $CuSO_4$ using a water tree AR of six, frequency of 60 Hz, and temperature of 20°C. Shown in the middle of the plot is a cutout of the cable model spanning from the insulation shield to the conductor with percentages corresponding to the depth of the water tree at those locations. Comparing percentages to their corresponding water tree locations in the cable, the following observations can be made: between depth percentages of 10 and 80, the water tree is completely enclosed inside the insulation; at 90% depth, the water tree has grown partially through the conductor shield; at 100% depth, the water tree has grown completely through the conductor shield and is now in contact with the conductor.

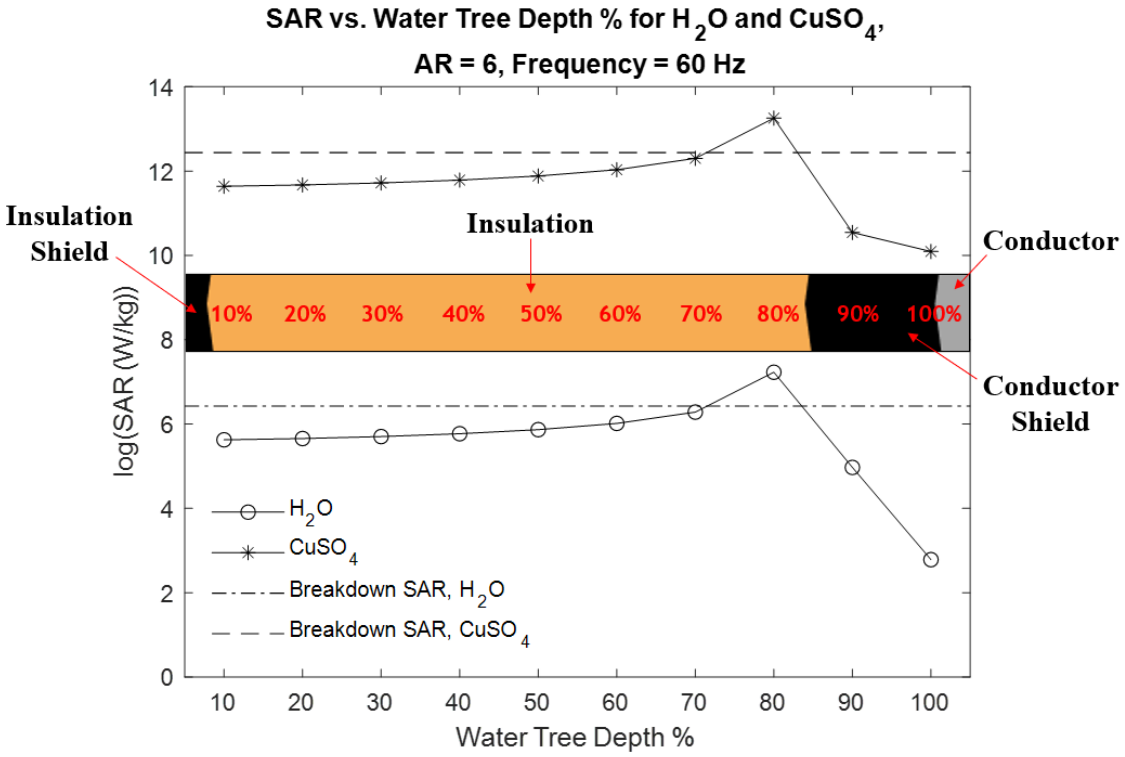

Figure 41. Logarithmic SAR versus water tree depth for H_2O and $CuSO_4$ using a water tree AR of six, frequency of 60 Hz, and temperature of 20°C. The horizontal "Breakdown SAR" lines indicate the SAR value where insulation breakdown occurs.

In the depth range of 10 to 80%, both compositions exhibit a similar relationship between SAR and water tree depth, although the SAR values for $CuSO_4$ are greater than those for H_2O because the former has a higher electrical conductivity than the latter. It is observed that SAR increases with increasing water tree depth, which is the same relationship found between electric field strength and water tree depth. Between depths of 10 and 70%, SAR increases approximately 12% in value for H_2O, and approximately 6% in value for $CuSO_4$. The most significant increase in SAR occurs between depths of 70 and 80%, which coincides with the water tree growing to a location just outside of the conductor shield. Between depths of 70 and 80%, SAR increases approximately 15% in

value for H_2O, and approximately 8% in value for $CuSO_4$. At 80% depth, the breakdown SAR of the insulation, which is represented on the plot by a horizontal line for each composition, has been exceeded, causing a permanent breakdown at that location. Although it appears that both water tree compositions first experience a permanent breakdown at identical depths, this is not correct. Permanent breakdown first occurs for $CuSO_4$ and H_2O at water tree depths of 74 and 75%, respectively. $CuSO_4$ experiences a permanent breakdown before H_2O because of its slightly greater electric field strength in that area of the insulation. The water tree grows through the conductor shield between depths of 80 and 100%, which produces a rapid decrease in SAR for both compositions. In this depth range, the water tree is approaching the conductor where inside an electric field cannot exist because of the absence of free electron movement. As a result, the SAR values experience a continual decrease as the water tree grows through the conductor shield until reaching a value of zero inside the conductor. Although interesting, the values and trends of SAR in this area of the cable are not particularly relevant to the primary area of concern for this thesis, which is the effect of water treeing on the insulation component. Localized permanent breakdown of the insulation previously occurred just prior to the water tree entering this area, which has created an increased probability of cable failure as a result.

5.6.2 3D Surface Representations of SAR using Pure Distilled Water

Having reviewed the relationship between SAR, water tree location, and water tree depth, the 3D surface representations can now be observed and discussed more clearly. Figures 42 through 46 show surface plots comparing logarithmic SAR, water tree

AR, and temperature for H_2O at water tree depths of 10, 50, 70, and 80%, and frequencies of 0.01, 60, 800, 10,000, and 1,000,000 Hz, respectively. Each plot contains a multi-colored surface of SAR values at different water tree ARs and temperatures, and a single-colored surface representing the breakdown threshold. The breakdown threshold surface is calculated using known values of breakdown strength (35 kV mm^{-1}) and mass density (860 kg m^{-3}) for the EPR insulation, along with a temperature-dependent electrical conductivity calculated at the pole of the water tree region. Therefore, the breakdown threshold surface indicates the minimum SAR values at different water tree ARs and temperatures that will produce a permanent breakdown of the insulation at the pole of the water tree region. To put it another way, any point on the multi-colored surface at or above the breakdown threshold surface is classified as a permanent breakdown, whereas any point below is indicative of degraded but still functional insulation material. With respect to water tree AR, the breakdown threshold values remain unchanged with increasing water tree AR because the electrical conductivity at the water tree pole is constant. As for temperature, the breakdown threshold values increase with increasing temperature because of the direct relationship between temperature, electrical conductivity, and thus SAR. Taking both relationships into account, the following observations are noted for the breakdown threshold surface: in the plane comparing logarithmic SAR to water tree AR, a perfectly horizontal line is shown; in the plane comparing logarithmic SAR to temperature, an exponential curve trending upwards with increasing temperature is shown.

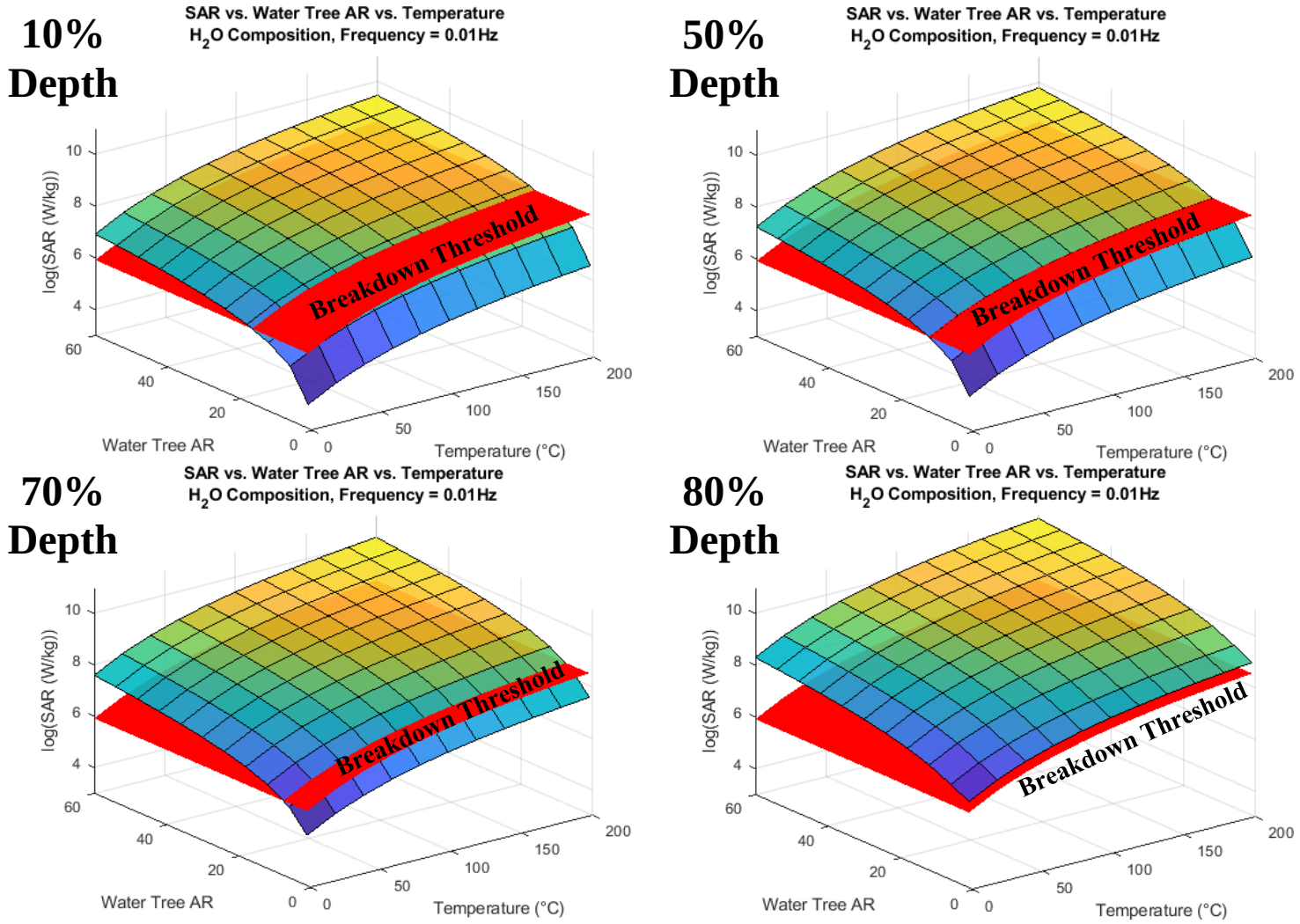

Figure 42. Surface plots comparing logarithmic SAR, water tree AR, and temperature for H_2O at a frequency of 0.01 Hz.

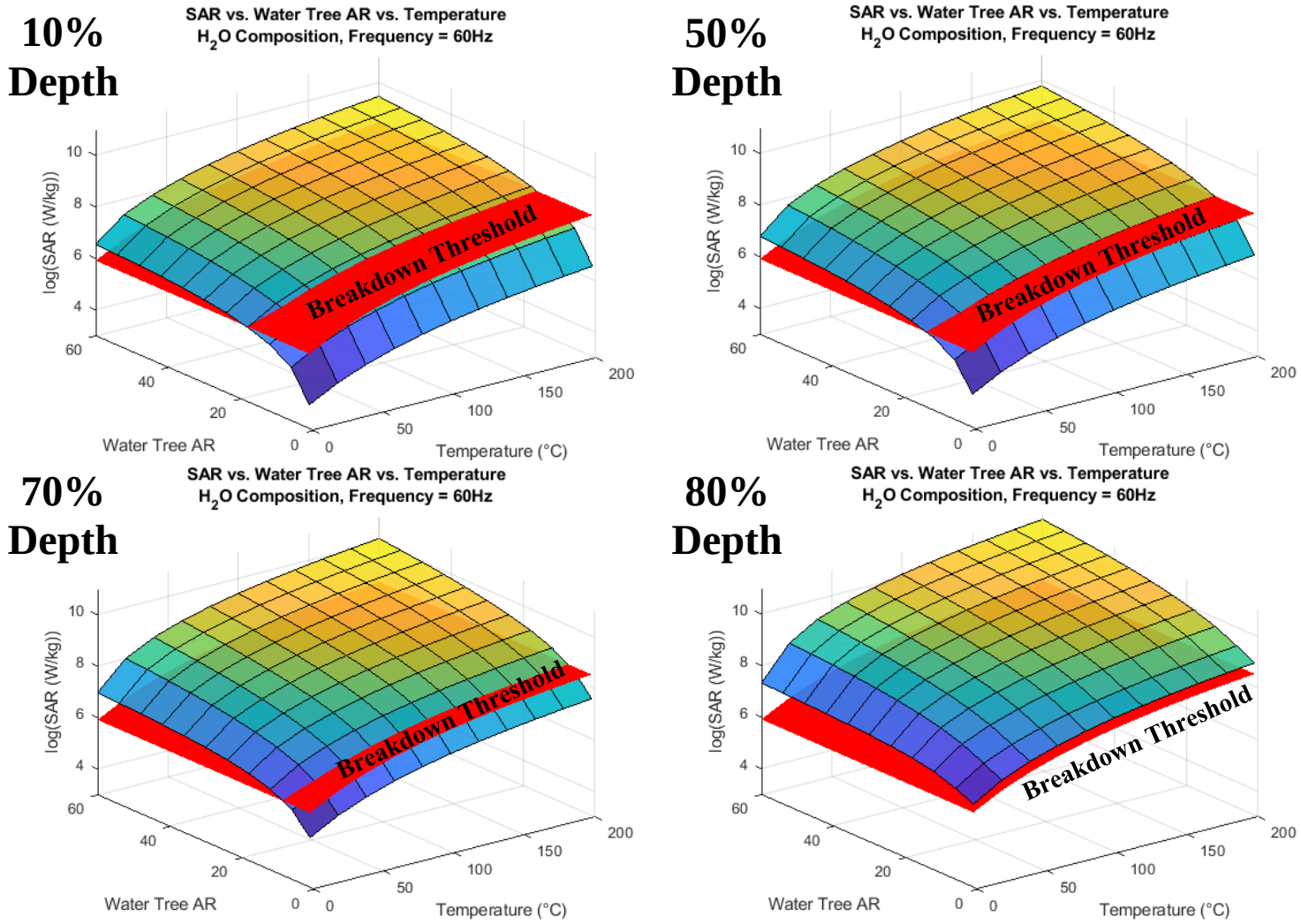

Figure 43. Surface plots comparing logarithmic SAR, water tree AR, and temperature for H_2O at a frequency of 60 Hz.

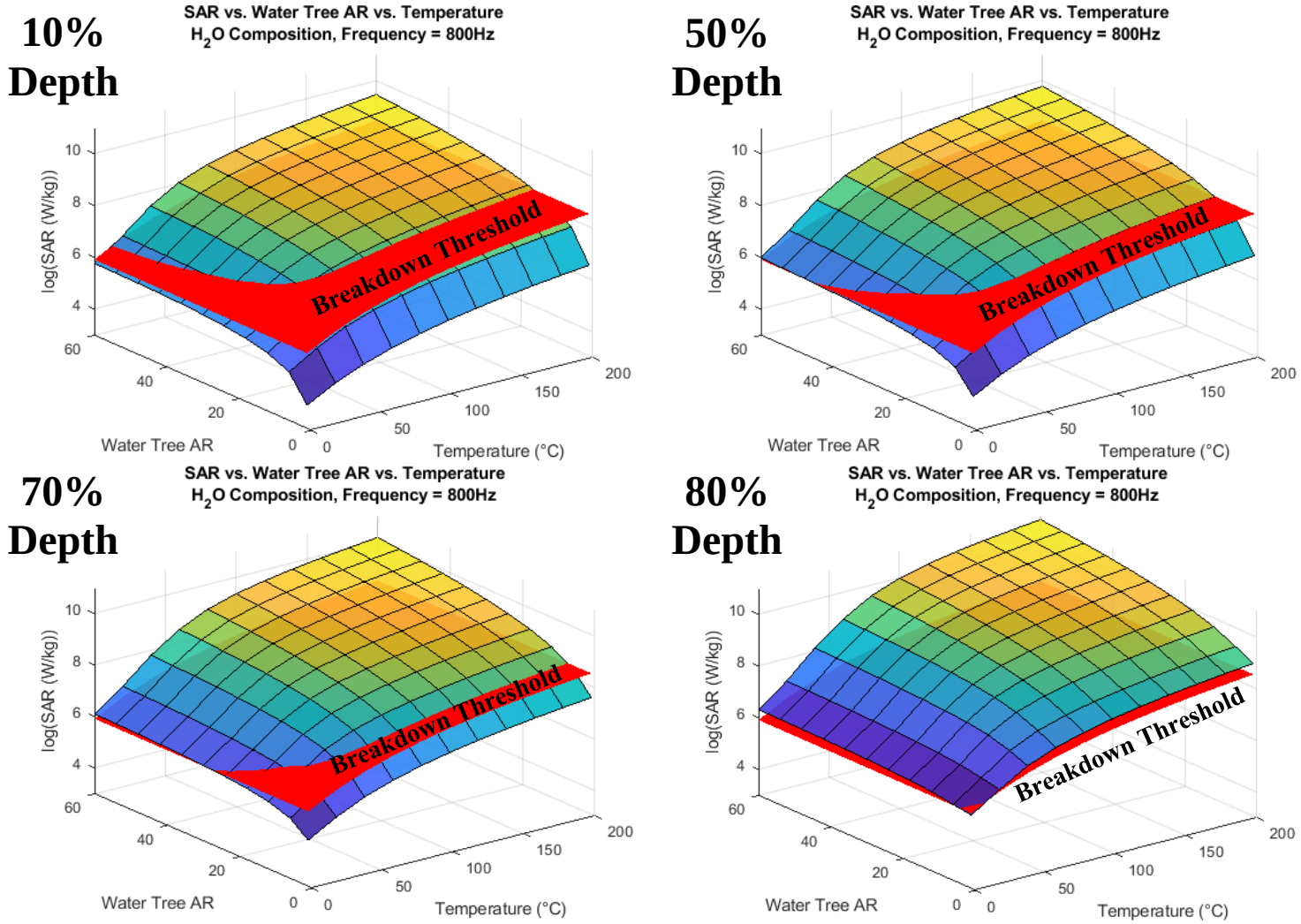

Figure 44. Surface plots comparing logarithmic SAR, water tree AR, and temperature for H_2O at a frequency of 800 Hz.

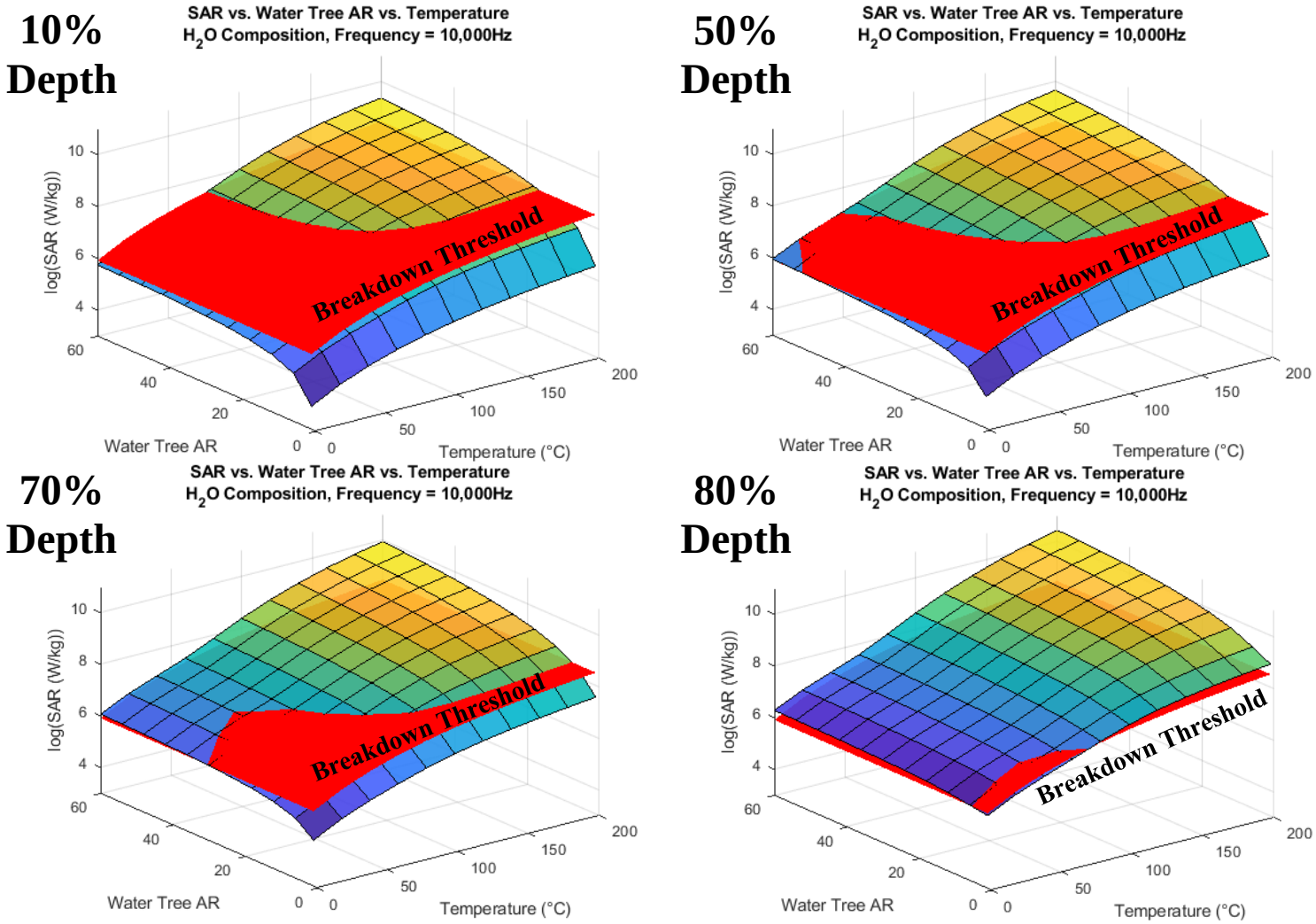

Figure 45. Surface plots comparing logarithmic SAR, water tree AR, and temperature for H_2O at a frequency of 10,000 Hz.

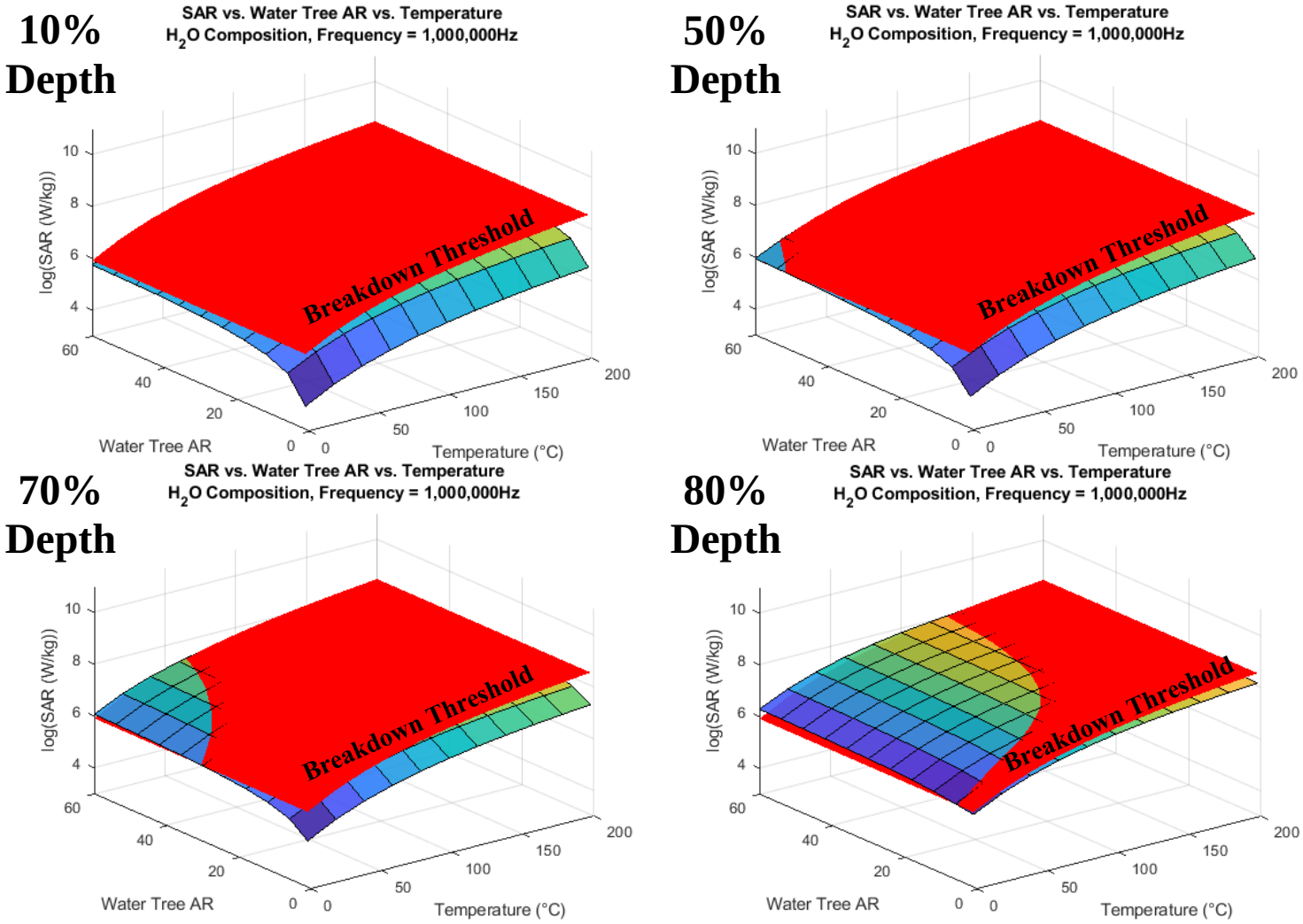

Figure 46. Surface plots comparing logarithmic SAR, water tree AR, and temperature for H_2O at a frequency of 1,000,000 Hz.

It is observed that for each frequency, the general relationship between SAR and water tree depth is the same. As water tree depth increases from 10 to 80%, the number of water tree AR and temperature combinations producing a SAR value above the breakdown threshold increases. Using Figure 42 as a discussion example, there already exists many water tree AR and temperature combinations that produce a permanent breakdown in the insulation at 10% depth. In fact, each water tree AR equal to a value of 18 and above produces a permanent breakdown across the entire range of temperature values. With regards to the magnitude of SAR with respect to water tree AR and temperature, it is observed that SAR increases with both increasing water tree AR and temperature, which is logical considering the relationships between water tree AR and electric field strength, and temperature, electrical conductivity, and SAR. The largest SAR value occurs at the maximum values for water tree AR and temperature (60, 200°C), whereas the smallest occurs at the minimum values (1, 0°C).

As the water tree grows from 10 to 50 to 70% depth, the number of water tree AR and temperature combinations producing a permanent breakdown increases. This is visually shown on the surface plots in Figure 42 by the increasing distance between the multi-colored and breakdown threshold surfaces as water tree depth increases. It should be noted that these observations also apply for surface plots at water tree depths between 10 and 70%. At 80% depth, it is observed that the multi-colored surface is completely above the breakdown threshold surface and thus every combination of water tree AR and temperature produces a permanent breakdown. This is reminiscent of Figure 41 which compared SAR to water tree depth and showed that for a standard water tree geometry,

permanent breakdown always occurs at a depth of 80%. As for depths of 90 and 100%, there exists no discernible relationships between the parameters because of the absence of a significantly intense electric field when the water tree enters the conductor shield. For this reason, surface plots at these depths are not provided in this thesis, but their general trends with respect to SAR can be inferred for both compositions based on the results shown in Figure 41.

As previously mentioned, the general relationship between SAR and water tree depth remains the same regardless of frequency. What is affected by frequency is the rate of increase in SAR as water tree AR and temperature increase. It is observed that as frequency increases, the rate of increase in SAR becomes less. For example, the percent difference between the maximum and minimum SAR values at 80% water tree depth is approximately 52% for a frequency of 0.01 Hz, but only approximately 35% for a frequency of 1,000,000 Hz. At high frequencies, this has the effect of lowering the number of parameter combinations producing a permanent breakdown at any given water tree depth. In comparison to 0.01 Hz, this effect is first visually noticeable at a frequency of 800 Hz, and becomes increasingly more apparent at frequencies of 10,000 and 1,000,000 Hz. The SAR values at these high frequencies are less than those at low frequencies such as 0.01 and 60 Hz, which indicates that less degradation has occurred. With that said, this does not account for the possibility of other degradation sources such as dielectric heating which is known to occur at frequencies above 800 Hz [71]. Further analysis and discussion of the difference in SAR values between frequencies is provided later in this chapter.

5.6.3 3D Surface Representations of SAR using Aqueous Copper Sulfate

In contrast to those for H_2O, the SAR values using $CuSO_4$ as the water tree composition were found to be largely independent of frequency, with only an insignificant decrease occurring at a frequency of 1,000,000 Hz. Figures 47 and 48 show surface plots comparing logarithmic SAR, water tree AR, and temperature for $CuSO_4$ at water tree depths of 10, 50, 70, and 80%, and frequencies of 0.01 and 1,000,000 Hz, respectively. To illustrate the observed relationship with frequency, the percent difference between the maximum and minimum SAR values at 80% water tree depth is almost identical for frequencies of 0.01 and 1,000,000 Hz, whereas for H_2O there was a noticeable difference between frequencies. Because of the relationship between the $CuSO_4$ SAR values and frequency, surface plots at 60, 800, and 10,000 Hz are excluded from this thesis.

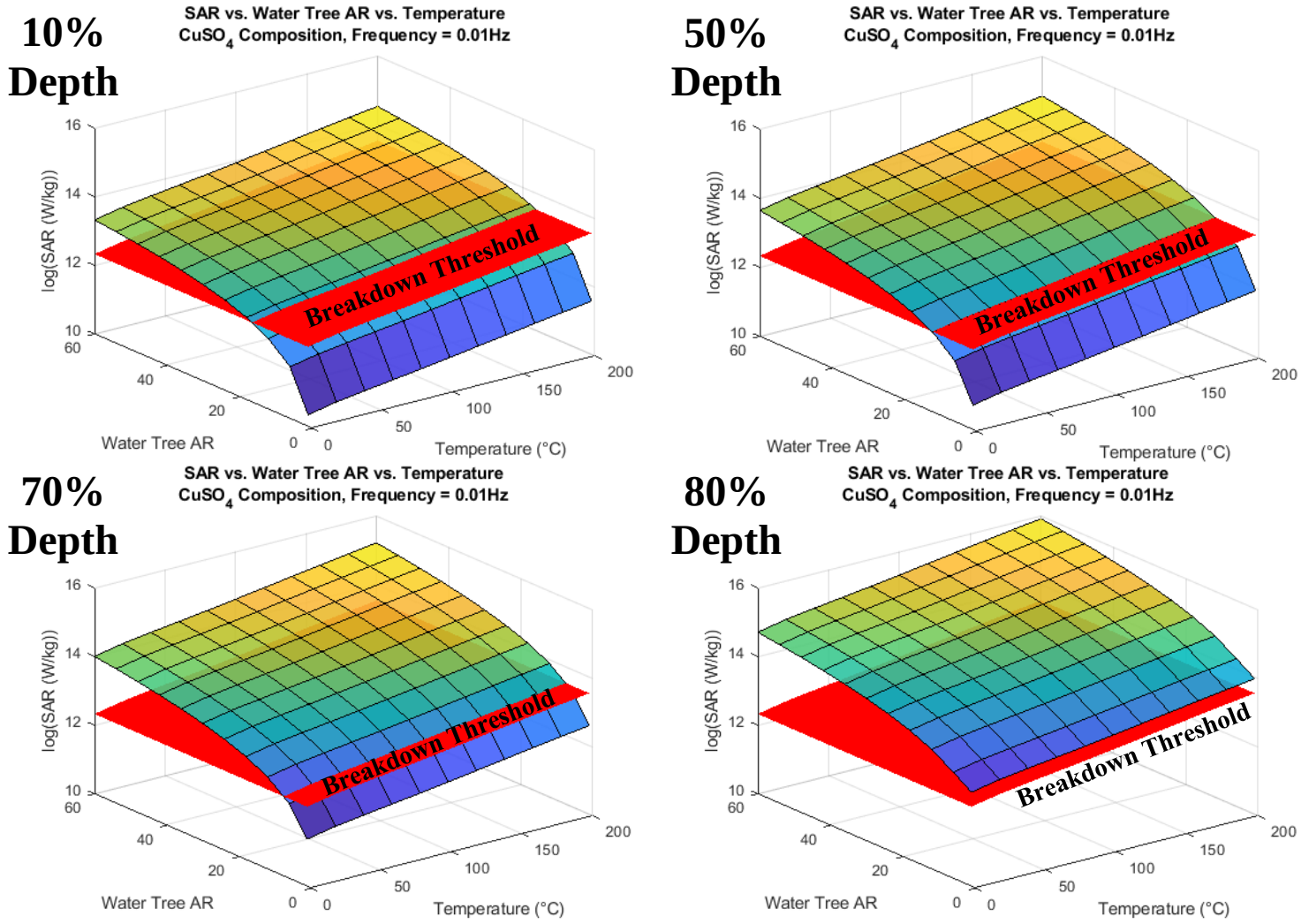

Figure 47. Surface plots comparing logarithmic SAR, water tree AR, and temperature for $CuSO_4$ at a frequency of 0.01 Hz.

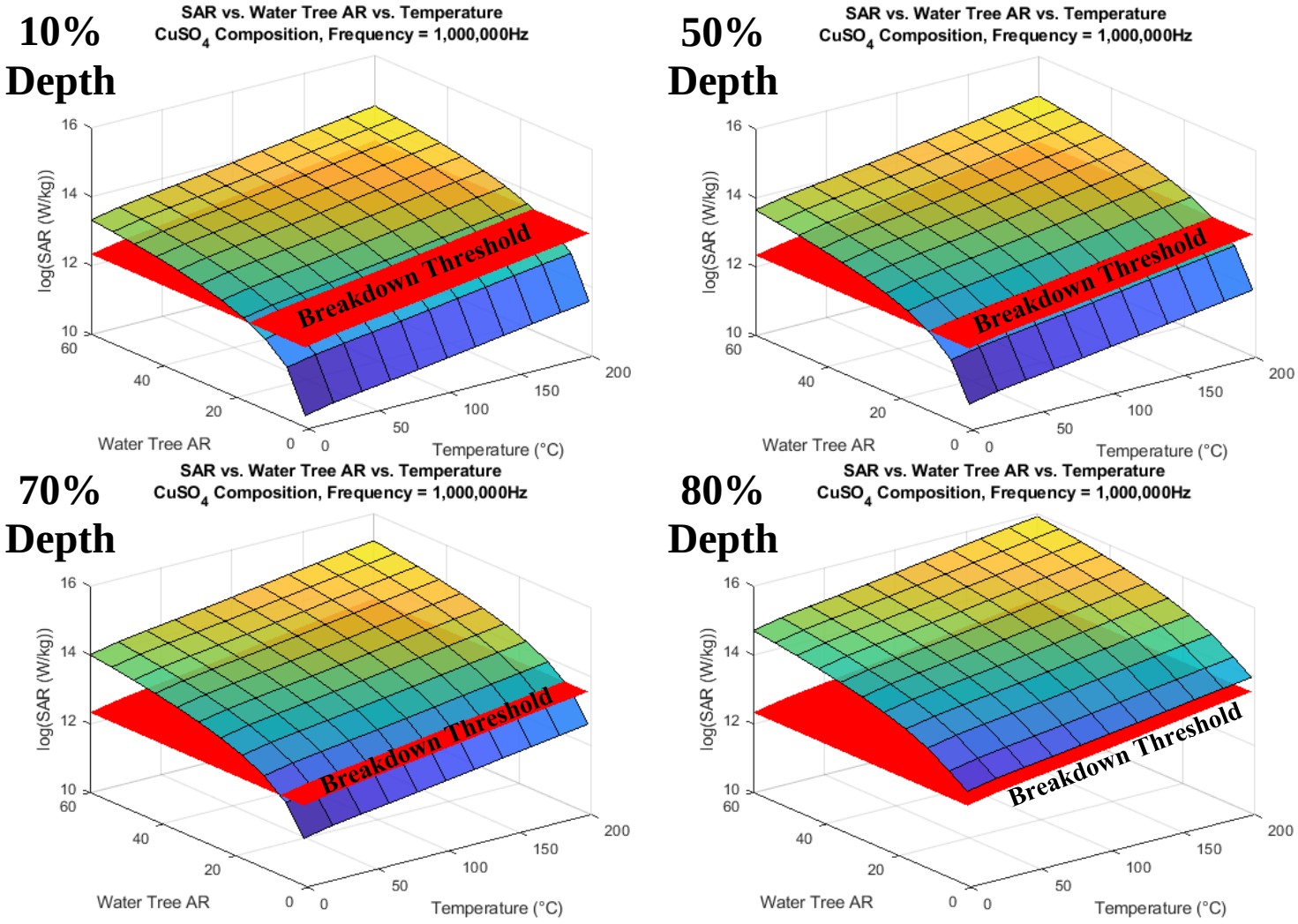

Figure 48. Surface plots comparing logarithmic SAR, water tree AR, and temperature for $CuSO_4$ at a frequency of 1,000,000 Hz.

Overall, the relationship between SAR and water tree depth for $CuSO_4$ is analogous to that found for H_2O. As water tree depth increases from 10 to 80%, the number of water tree AR and temperature combinations producing a SAR value above the breakdown threshold increases. Using Figure 47 as a discussion example, there already exists many water tree AR and temperature combinations that produce a permanent breakdown in the insulation at 10% depth. In fact, each water tree AR equal to a value of 18 and above produces a permanent breakdown across the entire range of temperature values. With regards to the magnitude of SAR with respect to water tree AR and temperature, it is observed that SAR increases with both increasing water tree AR and temperature. Like H_2O, the largest SAR value occurs at the maximum values for water tree AR and temperature (60, 200°C), whereas the smallest occurs at the minimum values (1, 0°C).

As the water tree grows from 10 to 50 to 70% depth, the number of water tree AR and temperature combinations producing a permanent breakdown increases. This is visually shown on the surface plots in Figure 47 by the increasing distance between the multi-colored and breakdown threshold surfaces as water tree depth increases. It should be noted that, like H_2O, these observations also apply for surface plots at water tree depths between 10 and 70%. At 80% depth, it is observed that the multi-colored surface is completely above the breakdown threshold surface and thus every combination of water tree AR and temperature produces a permanent breakdown. As for depths of 90 and 100%, there exists no discernible relationships between the parameters because of the

absence of a significantly intense electric field when the water tree enters the conductor shield.

5.6.4 SAR Comparison at Frequency Extremes for Pure Distilled Water

Figure 49 shows a surface plot comparing logarithmic difference in SAR between the frequency extremes of 0.01 and 1,000,000 Hz, water tree AR, and temperature, for H_2O at 80% water tree depth. Because similar relationships exist for each surface plot between depths of 10 and 80%, only the surface plot at 80% depth is provided in this thesis. Additionally, of the water tree depths simulated, 80% is where the insulation is most at risk of a breakdown, making it ideal for further analysis. As for $CuSO_4$, because there was found to be an insignificant difference in SAR values between the frequency extremes, no analysis is provided for this composition.

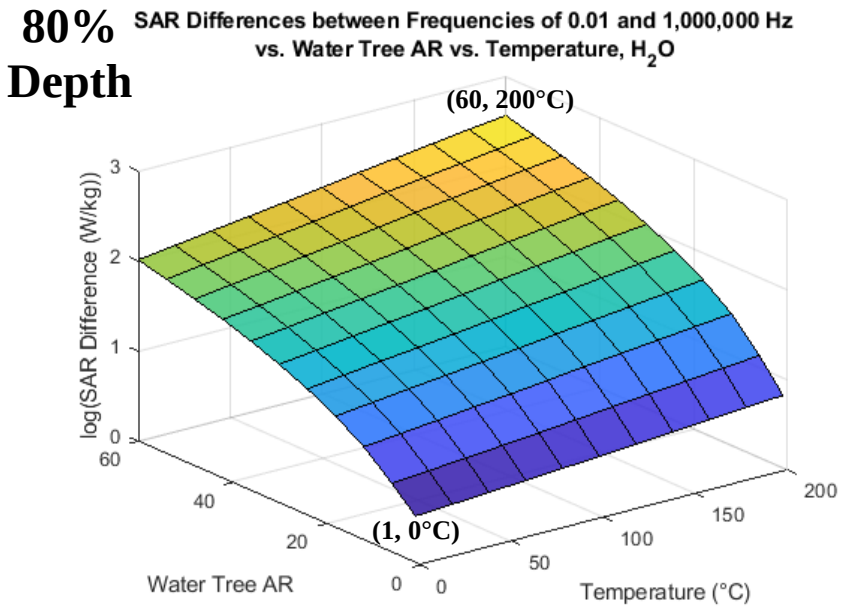

Figure 49. Surface plot comparing logarithmic difference in SAR between frequencies of 0.01 and 1,000,000 Hz, water tree AR, and temperature, for H_2O at 80% water tree depth.

It is observed that the greatest difference in SAR occurs at the maximum values for water tree AR and temperature (60, 200°C), whereas the smallest difference occurs at the minimum values (1, 0°C). To expand upon this, it can be stated that the difference in SAR between frequency extremes increases with both water tree AR and temperature. This is explained when considering the relationships between water tree AR and electric field strength, and temperature, electrical conductivity, and SAR. SAR is a function of both electric field strength and electrical conductivity, and increases with both parameters. Because the largest SAR value occurs at the maximum values for water tree AR and temperature, it is logical that the greatest difference in SAR between frequency extremes would also occur at this point. Conversely, it is logical that the smallest difference in SAR between frequency extremes occurs where the SAR value is smallest, which is at the point of minimum values for water tree AR and temperature.

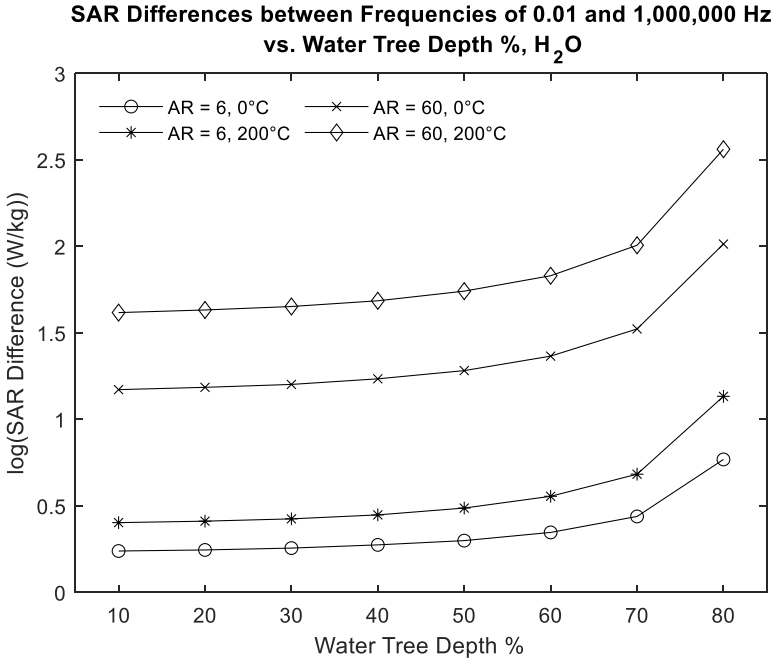

Figure 50. Logarithmic difference in SAR between frequencies of 0.01 and 1,000,000 Hz versus water tree depth for various water tree AR and temperature combinations.

The aforementioned relationships between difference in SAR, water tree AR, and temperature are also shown in Figure 50 which compares the logarithmic difference in SAR to water tree depths ranging from 10 to 80%. Because no discernible relationships between the parameters exist at depths of 90 and 100%, they are therefore excluded from the plot. As shown in Figure 50, the difference in SAR increases as the water tree grows further through the insulation, with the greatest increase in difference in SAR occurring between depths of 70 and 80%. It is also observed that, as was previously shown in Figure 49, the difference in SAR is a function of both water tree AR and temperature, with the greatest and smallest differences in SAR occurring at the maximum and minimum value combinations of water tree AR and temperature, respectively.

5.6.5 SAR Comparison between Water Tree Compositions

Figures 51 through 55 show surface plots comparing the logarithmic difference in SAR between $CuSO_4$ and H_2O at frequencies of 0.01, 60, 800, 10,000, and 1,000,000 Hz, respectively. For each frequency, the largest difference in SAR occurs at a water tree AR of 60 and temperature of 0°C (indicated on each plot), whereas the smallest difference in SAR occurs at a water tree AR of one and temperature of 200°C. Excluding 0.01 Hz, the following relationship between the value of the largest difference in SAR and water tree depth is observed: as water tree depth increases from 10 to 80%, the value of SAR at this point also increases. It is also observed that the differences in SAR increase as frequency changes from 0.01 to 10,000 Hz. Going from 10,000 to 1,000,000 Hz, there is either a slight decrease or no change in the difference in SAR depending on the water tree depth, with a larger SAR decrease observed at greater water tree ARs and lower temperatures.

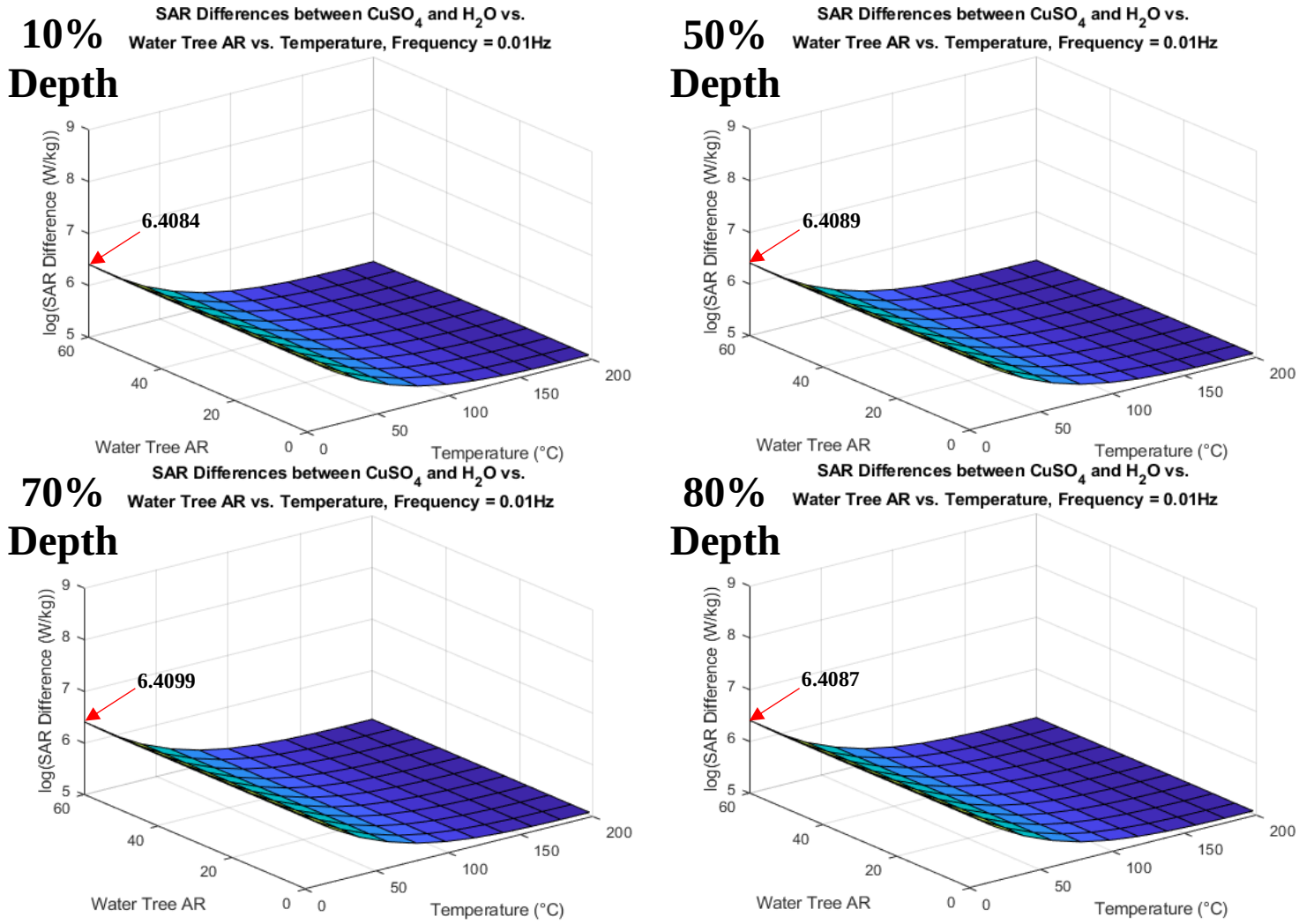

Figure 51. Surface plots comparing logarithmic SAR difference, water tree AR, and temperature at a frequency of 0.01 Hz.

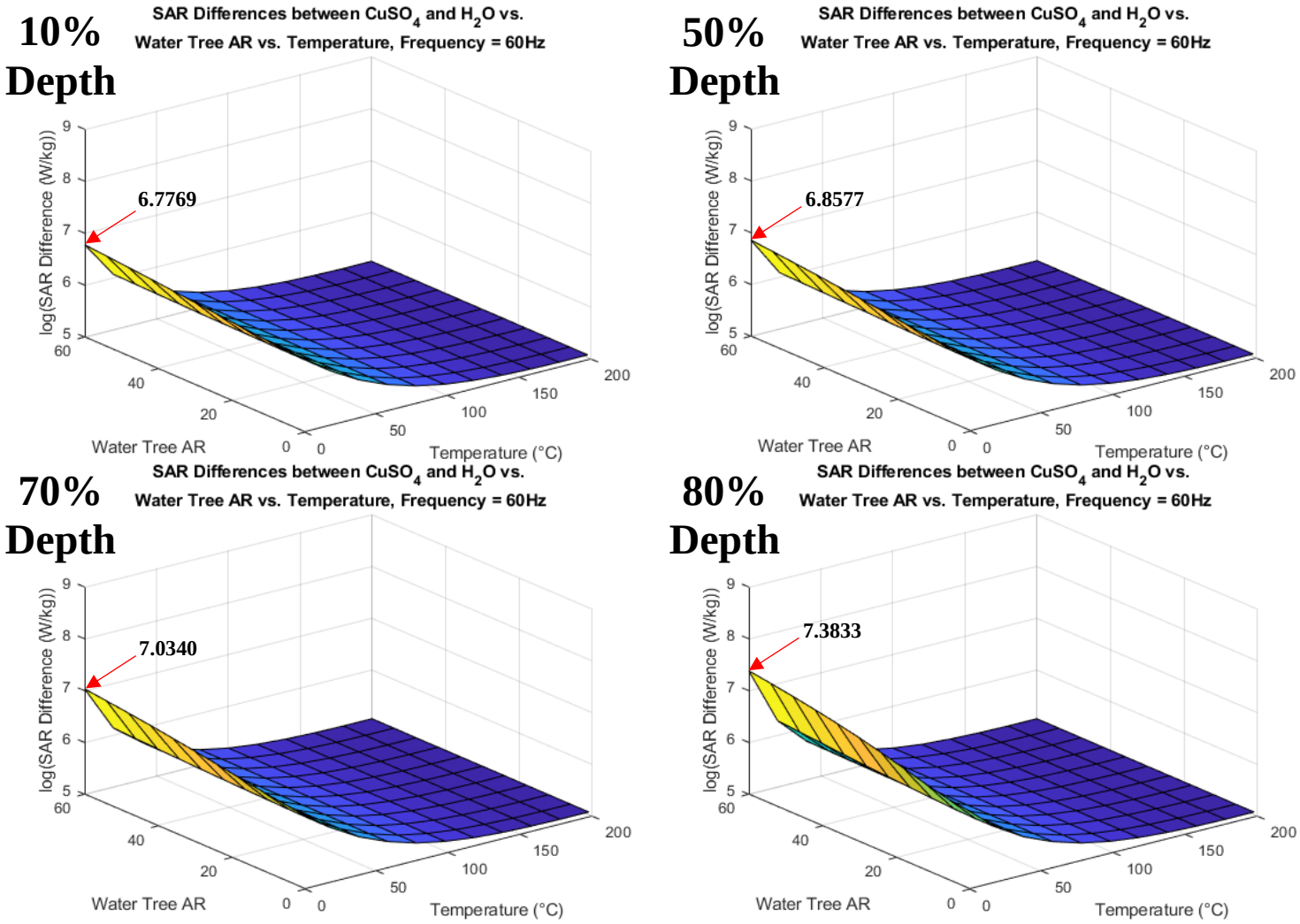

Figure 52. Surface plots comparing logarithmic SAR difference, water tree AR, and temperature at a frequency of 60 Hz.

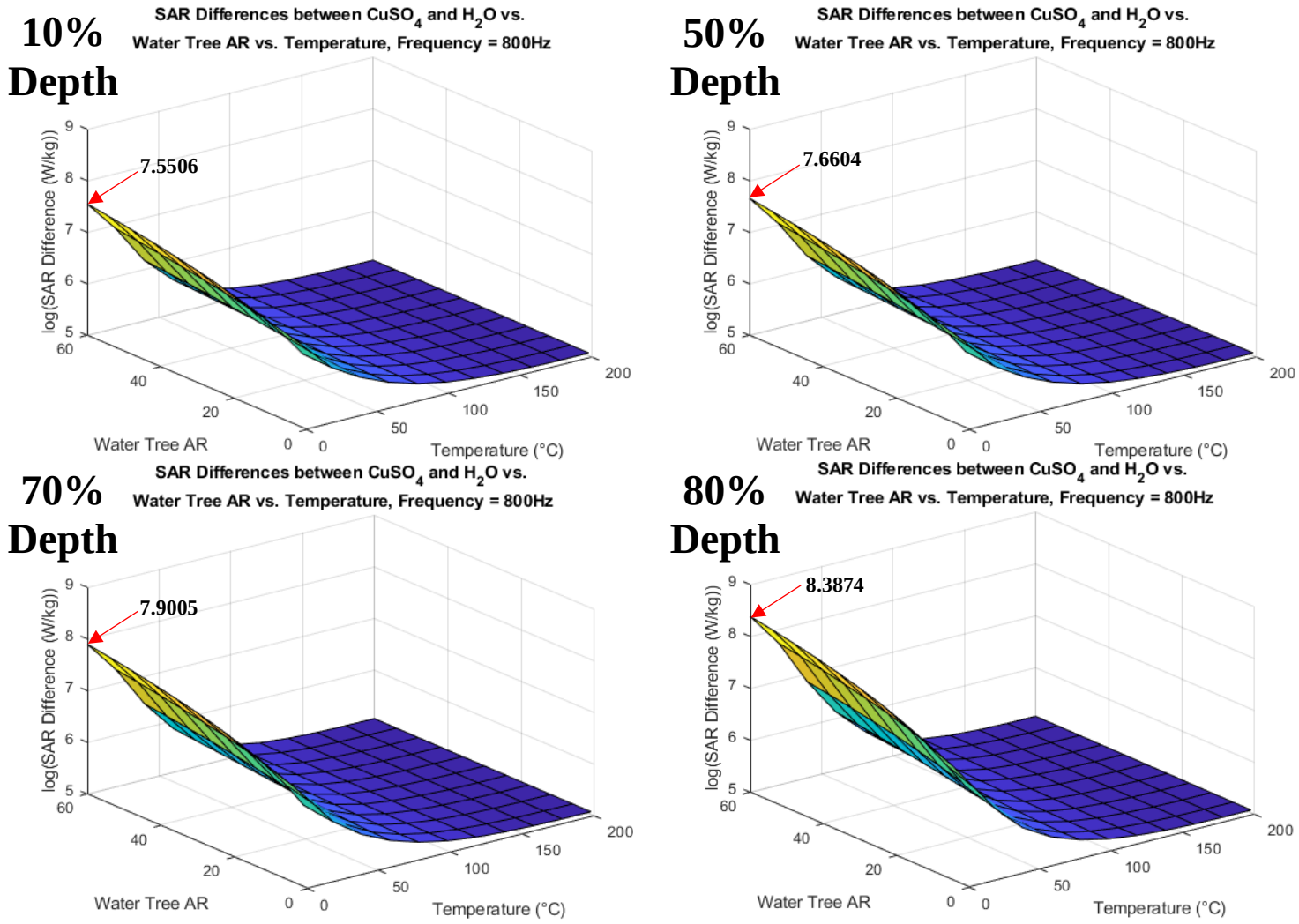

Figure 53. Surface plots comparing logarithmic SAR difference, water tree AR, and temperature at a frequency of 800 Hz.

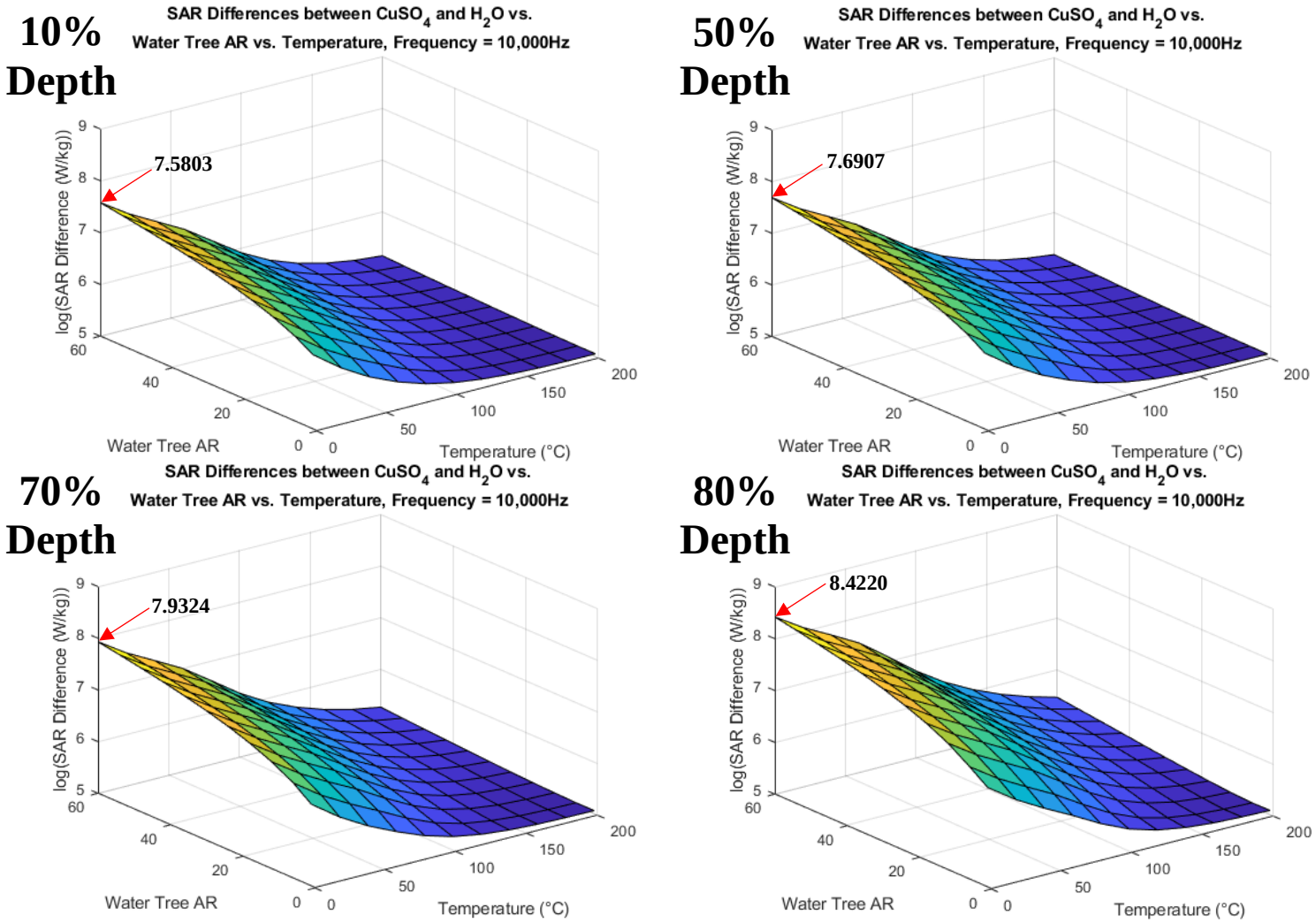

Figure 54. Surface plots comparing logarithmic SAR difference, water tree AR, and temperature at a frequency of 10,000 Hz.

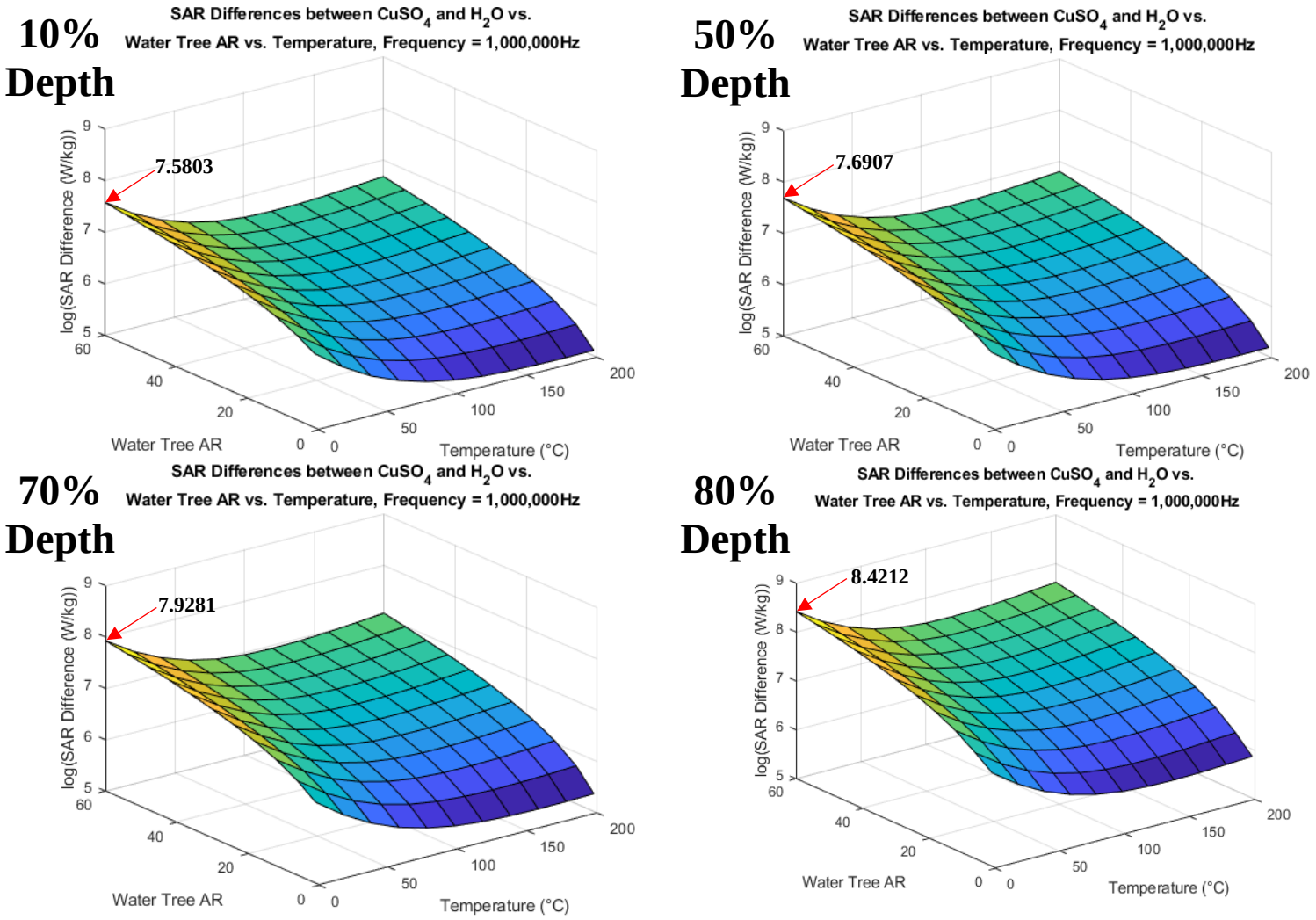

Figure 55. Surface plots comparing logarithmic SAR difference, water tree AR, and temperature at a frequency of 1,000,000 Hz.

As frequency increases, the differences in SAR at higher temperatures become more apparent. For example, when examining the plots at a frequency of 0.01 Hz, it is observed that the difference in SAR does not change drastically at temperatures of 100°C and higher for each water tree AR. In contrast, when examining the plots at a frequency of 1,000,000 Hz, there is a noticeable change in the difference in SAR across the entire temperature range. Also, the difference in SAR at this frequency increases with water tree AR, which as previously noted was not the relationship observed for 0.01 Hz.

5.6.6 Summary of Major Observations

Figures 41 through 55 demonstrate the relationship between SAR, water tree depth, water tree AR, temperature, and frequency for compositions of H_2O and $CuSO_4$. SAR, which was uniquely used as a measure of cable degradation caused by water treeing, was found to vary as the values for each simulation parameter changed. The following major observations were found in this section:

- For both compositions, SAR increases as the water tree grows through the insulation between water tree depths of 10 and 80%. At 80% depth, when the water tree has grown to a location just outside the conductor shield, permanent insulation breakdown occurs for both compositions. Although not shown graphically, permanent breakdown first occurs at depths of 74 and 75% for $CuSO_4$ and H_2O, respectively. After entering the conductor shield at 90% depth, there is a significant decrease in SAR because the intensity of the electric field has lessened. As the water tree grows completely through the conductor shield and

impacts the conductor at a depth of 100%, the intensity of the electric field continues to lessen resulting in a further decrease in SAR.

- When comparing the SAR value magnitudes, it is observed that the SAR values for $CuSO_4$ are greater than those for H_2O because of the difference in electrical conductivities between the compositions.
- For both compositions, SAR increases with water tree AR and temperature, with the largest SAR values occurring at the maximums of the two parameters, and the smallest values occurring at the minimums of the two parameters.
- From the 3D surface plots for both compositions, it is observed that the number of water tree AR and temperature combinations that produce a permanent breakdown increases with water tree depth. This is represented on the plots by a growing distance between the multi-colored SAR and breakdown threshold surfaces as water tree depth increases.
- When comparing the H_2O SAR values and surface plots at different frequencies, it is observed that the relationship between SAR and water tree depth remains unchanged, but the SAR values decrease with increasing frequency. This has the effect of decreasing the number of water tree AR and temperature combinations that produce a permanent breakdown at any given depth.
- The greatest difference in H_2O SAR values between frequencies of 0.01 and 1,000,000 Hz occurs at 80% depth for a water tree AR and temperature combination of 60 and 200°C, respectively, whereas the smallest difference occurs at a combination of one and 0°C, respectively.

- When comparing the $CuSO_4$ SAR values and surface plots at different frequencies, it is observed that the values are largely independent of frequency, with only an insignificant decrease occurring at a frequency of 1,000,000 Hz.
- When comparing SAR values between the compositions, it is observed that the difference in SAR increases as frequency changes from 0.01 to 10,000 Hz, with the $CuSO_4$ SAR values being consistently greater than those for H_2O. Going from 10,000 to 1,000,000 Hz, there is either a slight decrease or no change in SAR depending on the water tree depth. The largest differences in SAR consistently occur with greater water tree ARs and lower temperatures, with the maximum difference occurring at the water tree AR and temperature combination of 60 and 0°C, respectively. With the exception of 0.01 Hz, as water tree depth increases from 10 to 80%, the maximum difference in SAR also increases.

5.7 Localized Temperature Rise

It is well known that SAR is strongly correlated with a temperature increase due to electromagnetic heating inside the dielectric material [95,99,100]. The consequence of this correlation is the addition of another degradation source which further synergistically increases the rate of cable failure due to insulation breakdown. Because the loss of heat due to processes such as conduction is insignificant in electric cable insulation, SAR and temperature can be directly related using the following equation [95]:

$$SAR = C\frac{dT}{dt} \tag{4}$$

where, C is specific heat capacity of the dielectric material (J kg^{-1} $°C^{-1}$), T is temperature (°C), and t is the duration of exposure (s).

Given in Figure 56 is a set of distribution plots showing the temperature gradient magnitude inside the insulation and around the water tree region using water trees with ARs of six and 60, respectively, for H_2O. It is observed that the maximum value of the temperature gradient magnitude occurs at the pole of the water tree region closest to the conductor. This is identical to where the maximum electric field intensity and thus the maximum SAR occurs, which verifies the correlation between SAR and temperature change. Comparing water tree ARs, it is observed that the high intensity area of the temperature gradient magnitude is more widely dispersed inside the insulation for an AR of 60 compared to an AR of six. This visual observation is explained when comparing the values of the temperature gradient magnitude at the water tree pole. For ARs of 60 and six, the value of the temperature gradient magnitude is 167.08 and 76.52 °C m^{-1}, respectively, which represents an increase of approximately 118% as AR increases and the water tree narrows. This result also proves that, like SAR, localized temperature rise (LTR) is related with water tree AR, which will be explored further in this section.

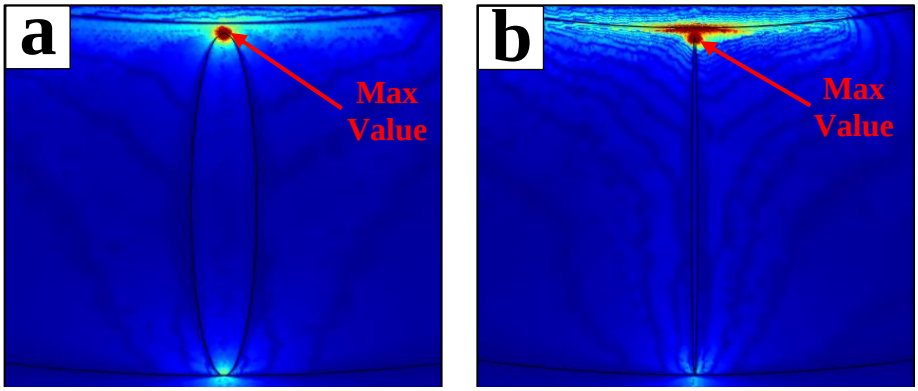

Figure 56. Localized temperature gradient magnitude at the water tree pole for a depth of 80% using H_2O with: (a) water tree AR of six; (b) water tree AR of 60.

For both H_2O and $CuSO_4$, it has been shown that SAR at the water tree pole increases with water tree AR. This is explained by the fact that the electric field strength,

which is directly related with SAR, increases as the water tree becomes narrower. It has also been shown that there is an apparent relationship between LTR at the water tree pole and water tree AR. Now, an effort will be made to correlate this LTR with water tree AR and SAR using a subset of values from the simulations. Because the primary interest is the correlation between the parameters, only SAR values at a temperature of 20°C will be used for this analysis. With that said, it is noted that higher temperatures produce greater SAR values with the expected result being a greater LTR in these scenarios.

Figures 57 and 58 show the LTR at the water tree pole versus water tree depths between 10 and 80% for compositions of H_2O and $CuSO_4$, respectively, and water tree ARs ranging from one to 60. Because the primary focus of this section is correlating LTR with SAR and water tree AR, only results using 60 Hz, which is the typical standard operating frequency for MV AC cables, are provided in this thesis. That being said, frequency is known to affect a variety of material properties including relative permittivity and electrical conductivity, and also cause dielectric heating at frequencies above 800 Hz. For these reasons, one would expect to see a larger LTR at frequencies above 800 Hz, specifically those of 10,000 and 1,000,000 Hz. Lastly, temperatures were recorded after only 10 seconds of exposure to the cable's electric field. Based on the relationship between LTR and exposure time, it is noted that longer exposure times such as days or months would be expected to produce a more significant LTR than what is presented in this thesis.

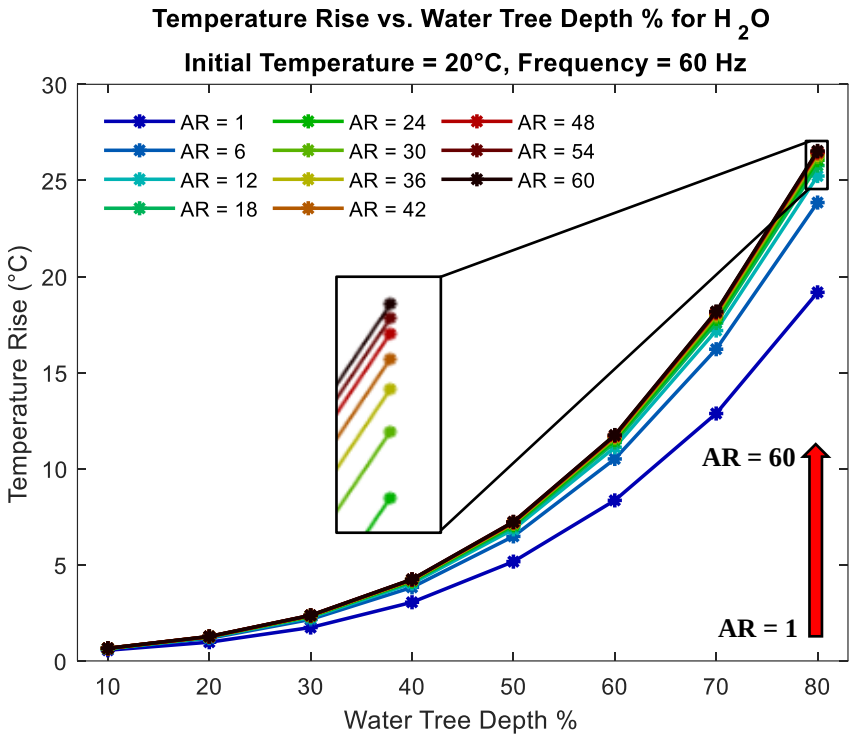

Figure 57. LTR versus water tree depth for H_2O. The arrow denotes the direction of AR increase corresponding to the order of data sets.

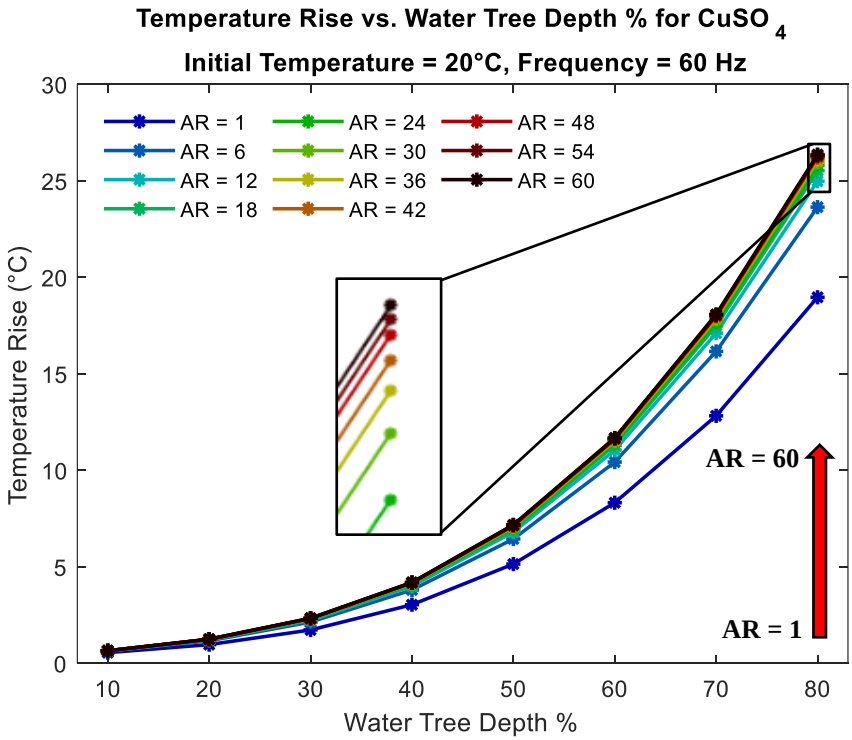

Figure 58. LTR versus water tree depth for $CuSO_4$. The arrow denotes the direction of AR increase corresponding to the order of data sets.

As predicted based on its relationship with SAR, it is observed that the LTR increases with water tree depth for both compositions. With each incremental depth change, the water tree grows closer to the charged conductor which has an operating temperature greater than the surrounding cable components. This produces a larger LTR at the water tree pole, which is the point closest to the conductor. It is also observed that the LTR increases with water tree AR, which was also predicted based on the relationship between AR and SAR. Another observation based on this relationship is that the difference in LTR between ARs increases as the water tree grows further through the insulation. Using Figure 57 as an example, at a water tree depth of 10%, the difference in LTR between ARs of one and 60 is approximately 0.1°C, whereas at a water tree depth of 80%, the difference is approximately 7°C. Because the water tree is closer to the conductor at 80% depth, there is more variability in the LTR values with increasing water tree AR. Lastly, it is observed that at each water tree depth, the difference in LTR between water tree ARs decreases with increasing AR. In other words, at each water tree depth, the largest difference in LTR occurs between water tree ARs of one and six, whereas the smallest difference occurs between ARs of 54 and 60. This is explained by the fact that as the water tree narrows with increasing AR, the region acting as the calculation point for the LTR becomes increasingly smaller. Although not tested, it is hypothesized that this trend of diminishing difference in LTR would continue at water tree ARs greater than 60, with an equilibrium LTR eventually being reached.

Figure 59 shows the difference in LTR between H_2O and $CuSO_4$ versus water tree depth using ARs ranging from one to 60. The overall trend is that the difference in LTR

increases with water tree depth, with the largest difference occurring at 80% depth and the smallest difference occurring at 10% depth. Apart from a single data point at 10% depth, each water tree AR and depth combination produces a LTR that favors H_2O over $CuSO_4$. This is counter to the expected result based on the relationship between SAR and LTR. Because $CuSO_4$ consistently produces SAR values that are larger than those produced using H_2O, it is expected that $CuSO_4$ would produce a larger LTR as a result. Further analysis is required to confirm this result and also to determine if it is sustained at higher temperatures than what was simulated for this thesis.

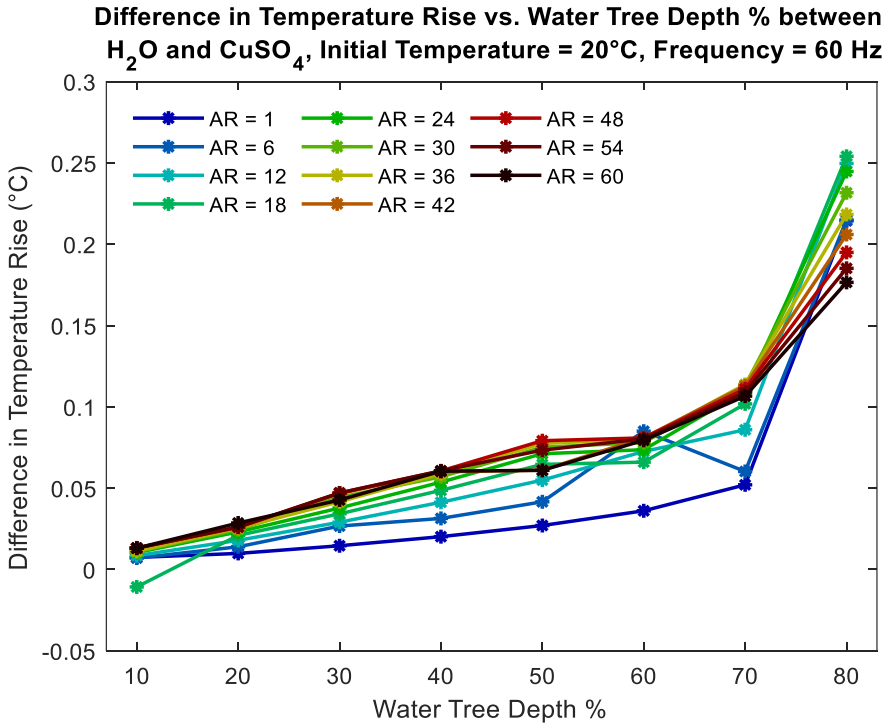

Figure 59. Difference in LTR between H_2O and $CuSO_4$ versus water tree depth.

Figures 60 and 61 show the relationship between logarithmic SAR and LTR at water tree depths between 10 and 80% for compositions of H_2O and $CuSO_4$, respectively, and water tree ARs ranging from one to 60. Comparing the compositions, it is observed

that practically identical trends exist between SAR, LTR, and water tree depth and AR. For each water tree depth and AR combination, the following relationship exists: SAR increases with both water tree depth and water tree AR, and as a result, a larger LTR is produced. There does exist a noticeable increase in SAR for an AR of one between water tree depths of 70 and 80%. Because the largest increase in electric field strength values between 70 and 80% depths occurs for an AR of one, it follows that the largest increase in SAR occurs between these depths, as indicated by Figures 60 and 61. That being said, the aforementioned relationships of SAR and LTR increasing with water tree depth and AR are still valid for the entire range of simulated values. Although these relationships have previously been shown in Figures 41 through 48, the direct relationship between SAR and LTR has until now not been visualized graphically as it is in Figures 60 and 61.

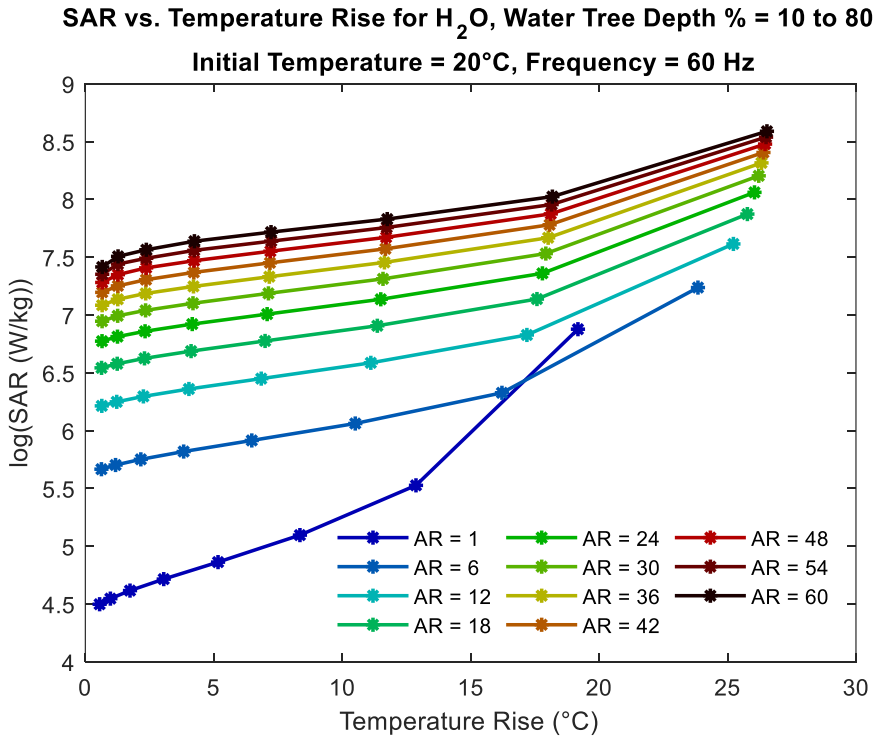

Figure 60. Logarithmic SAR versus LTR for H_2O with water tree depths ranging from 10 to 80%.

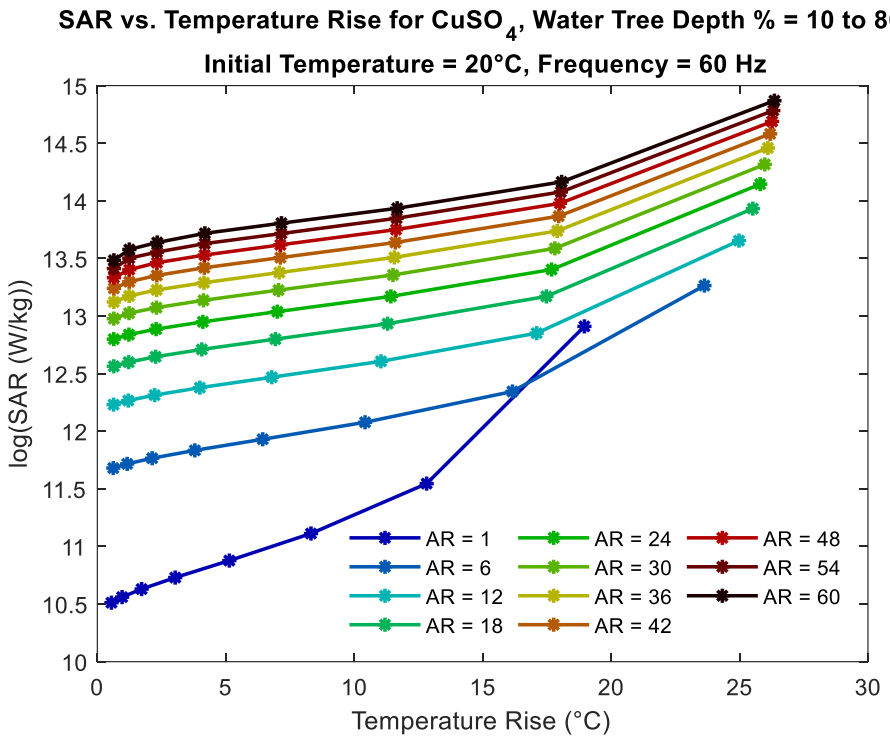

Figure 61. Logarithmic SAR versus LTR for $CuSO_4$ with water tree depths ranging from 10 to 80%.

5.8 Results Comparison

Global capacitance and resistance measurements were taken and analyzed at various water tree depths and temperatures. It was found that capacitance increases with water tree depth, whereas resistance slightly decreases between depths of 10 and 80%, followed by a significant decrease at depths of 90 and 100%. The largest change in capacitance occurs between depths of 90 and 100%, which corresponds to the depth range where resistance is minimized. These findings were true for both H_2O and $CuSO_4$. Additionally, capacitance and resistance both exhibit similar relationships with temperature for H_2O and $CuSO_4$, which is that increasing temperature produces smaller values for both. When comparing these results to those found from the voltage and electric field distribution plots, several similarities can be observed. First, distortion of

the cable's distribution increases steadily as the water tree grows in the depth range of 10 to 80%. Upon entering the conductor shield at 90% depth, there is a change in the distribution which coincides with the significant decrease in resistance. Second, the voltage distribution inside and around the water tree region indicated a voltage of approximately zero while it was inside the insulation. Considering this observation along with the relationship between capacitance, charge, and voltage, it makes sense that a reduction in the overall voltage of the system would produce an increase in capacitance. Lastly, it was noted that the flow of leakage current out of the conductor is more visually apparent when using $CuSO_4$ as the water tree composition, which helps to explain the larger decrease in resistance for $CuSO_4$ compared to H_2O.

Another observation is that localized SAR and LTR are related to the cable's global resistance. When comparing the measurements of SAR to those of resistance, it is observed that SAR increases with temperature, while resistance decreases. This is logical when considering the relationship between electrical conductivity, which affects both SAR and resistance, and temperature. Electrical conductivity increases with temperature, thus producing the observations for SAR and resistance that were found. It is also observed that the reduction in SAR occurs at the same depth and cable location as the reduction in resistance, which is when the water tree first enters the conductor shield. A further reduction in both SAR and resistance is observed as the water tree grows completely through the conductor shield to a depth of 100%. As for temperature, when comparing the difference in value of both SAR and resistance between water tree

compositions, the largest difference occurs at the minimum temperature of 0°C whereas the smallest difference occurs at the maximum temperature of 200°C.

In addition to global resistance, SAR is also related to distortion of the cable's voltage and electric field distribution. As the water tree grows through the insulation between depths of 10 and 80%, distortion of the cable's distribution increases which corresponds with increasing SAR in that depth range. It was also observed from the distribution plots that, based on the length of the electric field vector in this location, the maximum electric field intensity always occurs at the water tree pole. This observation is verified when quantifying the electric field strength around the water tree region, which by doing so proves that the maximum intensity and thus the maximum SAR occurs at the water tree pole. Lastly, the reduction in SAR at 90% depth corresponds to the water tree region experiencing an elevated voltage because of the flow of leakage current, which continues as the water tree grows further through the conductor shield.

5.9 Connection to Physical Cable Tests

The final section of this chapter consists of a discussion regarding the connection between the areas of results and physical cable tests. Global capacitance measurements are similar to the physical parameters of cabling that are tested with TDR and PDC. Both tests make use of capacitance indirectly, with TDR's electrical impedance measurement being a function of capacitance, and PDC using capacitance in the calculation of both current types for which it is named. TDR and PDC have similar disadvantages including difficulty in detecting certain defects such as early-stage water trees, and requiring the cable to be taken offline during testing. The impact of these disadvantages can be

lessened by using FEA capacitance measurements in conjunction with physical measurements taken with TDR and PDC to create a more accurate assessment of a cable's health.

Global resistance measurements can be used to enhance leakage current testing of physical cables in operation. This test is used to measure the amount of leakage current flowing through the insulation because of defects such as water treeing. Knowing the leakage current and voltage rating, the cable's resistance can be calculated and compared against that of a healthy cable, as well as FEA results such as those obtained in this thesis. The primary disadvantage of leakage current testing is that the results are affected by the environmental conditions of the cable being tested, which makes it difficult to measure degradation over time. Although not attempted for this thesis, these environmental conditions can be simulated using FEA at various points in time to help predict the progression of degradation in a physical cable based solely on its resistance.

Voltage and electric field distributions and localized SAR measurements are both connected to a physical test not particularly common in the electric cable testing industry. This test uses a device called an electromagnetic field meter to measure the electric field of an object which can then be compared to that of an identical object in pristine condition. Using this test on physical cables, distortions in the voltage and electric field distribution can be recorded and potentially compared to FEA results such as the distribution plots provided in this thesis. Additionally, results obtained from this test in conjunction with electrical conductivity measurements taken from a physical test such as PDC can be used to quantify the SAR of a cable, with the possibility of determining

specific locations where the SAR is greatest and thus most likely to contain a defect such as a water tree.

LTR is, by itself, most connected with TIRI testing. In the field of electric cable testing, TIRI is used to measure the cable's temperature distribution to locate regions of abnormally high temperature which may indicate the presence of a defect. One disadvantage of TIRI is that it is difficult to detect water-related degradation such as water treeing, which, as is shown in this thesis, experiences a LTR and thus can be classified as a region of abnormally high temperature. Without direct access to the insulation, TIRI cannot be used to measure this LTR, as well as predict how it will affect the cable's electrical properties over time. Results taken from FEA simulations of water tree degradation, such as those presented in this thesis, can help alleviate this disadvantage of TIRI.

CHAPTER SIX:
CONCLUSIONS AND FUTURE WORK

6.1 Conclusions

This thesis presented a parametric evaluation of the water treeing phenomenon in EPR-insulated MV cables using FEA. After reviewing relevant literature related to the water treeing phenomenon, a variety of shortcomings were noted, which this thesis set out to address. Among these shortcomings was a lack of knowledge regarding the effects of various cable and water tree parameters on the rate of cable degradation caused by water treeing. To overcome this lack of knowledge, a parametric study was created to evaluate the effects of changing water tree depth, water tree AR, water tree composition, cable operating frequency, and temperature on the rate of cable degradation. Evaluation was performed in five separate but interrelated areas pertaining to the measurement of cable degradation: global capacitance, global resistance, voltage and electric field distribution, localized specific energy absorption rate, and localized temperature rise. The results from each area provided a significant amount of information regarding the water treeing phenomenon in general, but also a better understanding of how the parametric study parameters affect the rate of degradation.

Global capacitance measurements were taken at various locations along a water tree's growth path towards the conductor for both H_2O and $CuSO_4$ water tree compositions at temperatures ranging from 0 to 200°C. It was determined that capacitance decreases with increasing water tree AR, with the effect being fairly insignificant but more profound at greater water tree depths. Because similar

relationships were observed for each water tree AR, only an AR of six was used for these simulations. For both compositions, it was found that capacitance increases as the water tree grows closer to the conductor, and that increasing temperature produces a decrease in capacitance. When comparing capacitance measurements between the compositions, relationships between the difference in capacitance and both water tree depth and temperature were found. As water tree depth increases, the difference in capacitance between the compositions also increases, with the minimum and maximum differences occurring at water tree depths of 10 and 100%, respectively. As for the relationship with temperature, it was found that the difference in capacitance between the compositions increases with temperature, with each temperature in the simulated range apart from 0°C producing a difference in capacitance that favored $CuSO_4$ over H_2O. Based on these findings, it can be concluded that the rate of cable degradation measured with respect to capacitance is influenced to some extent by water tree depth, water tree AR, water tree composition, and temperature.

In similar fashion, global resistance measurements were taken at various locations along a water tree's growth path towards the conductor for both H_2O and $CuSO_4$ water tree compositions at temperatures ranging from 0 to 200°C. For both compositions, it was found that the resistance is relatively constant up to a water tree depth of 80%. As the water tree grows from 80 to 90% depth, there is a sudden decrease in resistance followed by a slight decrease going from 90 to 100% depth. These observations are explained when considering the location of the water tree at these depths. Between 10 and 80% depth, the water tree is completely enclosed inside the insulation, whereas between 80

and 100% depth, the water tree has partially entered the semi-conductive conductor shield. Upon entering the conductor shield, the water tree becomes a pathway for the flow of leakage current which causes a reduction in resistance. In addition to water tree depth, temperature was found to have a noticeable effect on the resistance with an increasing temperature producing a decrease in resistance. As for water tree AR, a direct relationship between resistance and AR was observed, with the effect being fairly insignificant between water tree depths of 10 and 80%, but more so at 90 and 100%. When comparing resistance measurements between compositions, there was found to be little to no difference in the depth range of 10 to 80%, but there was a noticeable temperature-dependent difference between depths of 80 and 100% with H_2O producing greater resistance values than $CuSO_4$. As with capacitance, it can be concluded that the rate of cable degradation measured with respect to resistance is influenced by water tree depth, water tree AR, water tree composition, and temperature.

Water tree degradation was visually observed on voltage and electric field distribution plots at various water tree depths, water tree ARs, operating frequencies, and temperatures for both H_2O and $CuSO_4$ water tree compositions. For both compositions, it was found that voltage and electric field distortion increases between depths of 10 and 80%, with the effects being an approximate zero voltage inside and around the water tree region, and an increase in electric field intensity in the same area. At depths of 90 and 100%, the water tree enters the conductor shield allowing for the flow of leakage current out of the conductor. The flow of leakage current creates an elevated voltage inside and around the water tree region, with this effect being more visually apparent for $CuSO_4$. It

was also found that for each water tree composition, voltage and electric field distortion increases as water tree AR decreases and temperature increases. Except for 90 and 100% depths for H_2O, this trend was maintained across the entire range of water tree depths. As for frequency, it was found that for H_2O, voltage and electric field distortion decreased with increasing frequency along the entire range of water tree depths, with no noticeable change observed for $CuSO_4$. These findings show that water tree degradation works to distort the normal voltage and electric field distribution of a cable, and that the level of distortion is dependent on each parameter being studied.

One additional observation taken from the voltage and electric field distribution plots is that the maximum electric field intensity always occurs at the location of the water tree pole closest to the conductor. As a result, it was noted that this area of insulation will be the first to experience an electric field magnitude that exceeds the breakdown strength of the insulation material, thus producing a permanent breakdown. Despite knowing the location, visual observation of the distribution plots alone cannot determine when and under what conditions a permanent breakdown will occur. To alleviate this inadequacy, this thesis conducts a novel quantitative assessment of insulation breakdown using a calculated parameter called SAR, which is defined as the amount of energy absorbed per unit of mass by a dielectric material such as cable insulation. SAR is directly related to the electric field magnitude and was used as both a measure of the rate of cable degradation caused by water treeing, and for a determination of permanent breakdown based on various cable and water tree conditions defined by the parameters being studied.

Using an equation that relates electric field strength, electrical conductivity, and mass density, localized SAR values at the water tree pole were calculated for various water tree depths, water tree ARs, operating frequencies, and temperatures for both H_2O and $CuSO_4$ water tree compositions. Both compositions exhibited the same general relationship between SAR and water tree depth, which is that SAR increases between depths of 10 and 80%, and decreases between 80 and 100%. Permanent breakdown was found to occur for both compositions at a location just outside the conductor shield, which corresponds to a depth of 80%. Although not shown graphically, permanent breakdown first occurs at depths of 74 and 75% for $CuSO_4$ and H_2O, respectively. When examining the 3D surface representations, relationships were found between SAR and the parameters being studied. For both compositions in the depth range of 10 to 80%, SAR was found to increase with increasing water tree AR and temperature. In the same depth range, SAR was found to decrease with increasing frequency for H_2O, but was largely independent of frequency for $CuSO_4$, with only an insignificant decrease occurring at 1,000,000 Hz. No discernible relationships exist between SAR and the study parameters at water tree depths of 90 and 100%, so they were excluded from this thesis. These findings, along with additional analysis provided in Chapter Five, show that SAR can be used as both a measure of the rate of cable degradation caused by water treeing, and as a quantitative determination of when and under what cable and water tree conditions a permanent breakdown occurs.

There exists a connection between SAR, water tree AR, and LTR at the water tree pole. Based on the relationship found between SAR and water tree AR, and the fact that

SAR is correlated with LTR, it is expected that increasing water tree AR will produce a larger LTR. For both water tree compositions, this expectation was found to be accurate. It was also determined that LTR increases with water tree depth, which is identical to the relationship between SAR and water tree depth. As the water tree grows closer to the charged conductor, which has an operating temperature greater than the surrounding cable components, the LTR at the point closest to the conductor, being the water tree pole, increased after each incremental depth change.

The other objective of this thesis was to present an argument for further use of FEA in conjunction with physical cable testing. As shown by this thesis, FEA can be used to simulate a wide variety of conditions and scenarios related to water tree degradation, including some of which may only occur in physical cables under unique circumstances. Additionally, FEA has many advantages that together provide a motivation for its use as a companion component to traditional physical testing. In situations where an operational cable cannot be easily accessed or would be burdensome to take offline, FEA can fill the void by providing an initial assessment of the cable's health. This initial assessment, albeit limited in accuracy, can then be interpreted by cable degradation testers to determine if more thorough testing is required. FEA can also be used to alleviate two common disadvantages found in most physical cable tests, which are the inability to track water tree degradation over time and inability to predict future cable conditions. Using physical test results as simulation inputs, a realistic model of an operational cable can be designed and simulated at various future points in time to predict the evolution of the cable's degradation, including the expected remaining lifetime.

Another advantage of FEA in contrast to physical testing is its ability to assess the early stages of water tree degradation, including the point at which a water tree is first formed. Occasionally, physical tests will return results that are indicative of a healthy cable when in fact a defect such as a water tree is present but has not grown to a sufficient extent to be noticeable. FEA can determine the degradation characteristics of such a water tree and also predict when it will have grown to a sufficient extent to be detectable by physical tests. Although not all-encompassing, the advantages of FEA given in this thesis provide a motivation for its further use in conjunction with physical cable testing, with the overall result being improved outcomes in the long run for cable testers and operators of NPPs.

The results and findings presented in this thesis have provided an advanced understanding of the water treeing phenomenon in MV EPR-insulated cables under changing operational and environmental conditions. In addition, an argument for further use of FEA in conjunction with physical cable testing was presented, with the conclusion being that there exists a strong motivation to pair the two together. Given the limited time associated with this project, several ideas for further research regarding the topic of water tree degradation were left unexplored. To close out this thesis, these ideas will be described with the hope that future water tree degradation researchers can explore them and build upon the findings of this thesis.

6.2 Future Work

Although this thesis produced a better understanding of both the water treeing phenomenon and its effects on EPR-insulated MV cables using simulation software, there exists several ideas left unexplored that future research should address. First, this thesis

did not consider the effect of frequency on various material properties including relative permittivity and electrical conductivity. Frequency is known to affect these properties for both EPR and H_2O [73,101,102], and it is hypothesized that similar trends exist with those properties for $CuSO_4$. Additionally, the LTR using frequencies greater than 800 Hz was not examined in this thesis. Frequencies greater than 800 Hz are known to cause dielectric heating with the expected result being a more significant LTR at these frequencies. A complete understanding of the water treeing phenomenon requires simulating with a physically accurate model, which is accomplished when considering the full effects of frequency.

Second, this thesis did not consider the effect of different filler materials present in the EPR blend. EPR is known to have a complex formulation with varying material properties depending on the filler materials that have been added. Filler materials such as hard clay, barium sulfate, and calcium carbonate are often added to EPR to improve specific properties such as flame retardancy [103]. Additional simulation work using a variety of common EPR blends will produce a more accurate characterization of the material and a better understanding of how EPR filler materials affect the occurrence of water tree degradation.

Third, further validation and verification of the simulation results is required to enhance their credibility. This can be accomplished through physical testing using similar conditions as those defined in the parametric study. Results from physical testing of water tree degradation can be compared to those obtained through simulation to improve confidence in both the cable model and simulation setup. In addition, findings obtained

through physical testing can be incorporated into the simulation work to create a more accurate representation of the water treeing environment.

Fourth, this thesis only examined a 2D representation of water tree degradation in MV cables. Although sufficient for the objectives of this thesis, this does not provide a complete understanding of how water tree degradation affects the entire cable length, which is only possible with a 3D representation. A 3D representation can also provide additional information such as how water tree location and orientation along a cable's length affect the rate of degradation. This information can be used in conjunction with physical cable testing results to better inform lifetime service predictions for existing MV cables.

Fifth, this thesis relied on two assumptions for the water tree region that are known to be physically inaccurate. The first assumption was that the entire composition of the water tree region is either H_2O or $CuSO_4$. In a physical water tree inside cable insulation, the water tree region will be a mixture of aqueous solution and insulation material, and therefore have composite material properties that are somewhere between those of the aqueous solution and the insulation material. The second assumption was that the relative permittivity and electrical conductivity are constant across the entire length of the water tree region. Because a physical water tree is known to be a collection of micro-sized cylindrical pathways with varying densities, this assumption is not physically accurate. The water tree's relative permittivity and electrical conductivity will vary across its entire length, with the formation point producing the greatest values followed by a decrease along the water tree's length. This has been examined previously in research by

Burkes [80], but only to examine how changing water tree depth affects the rate of degradation. Further research exploring the effects of the parameters used in this thesis in conjunction with length-varying relative permittivity and electrical conductivity values will contribute to a more accurate understanding of water tree degradation in MV cables insulated with EPR.

Lastly, the results of this thesis are truly informative of a cable's expected service lifetime when they can be directly compared to physical measurements taken in the field. Although possible for a cable's capacitance and resistance, quantifying a cable's SAR and determining high electric field-intense locations such as those around a water tree is not as easy of a task. The development of a physical measuring technique for SAR in cable insulation will provide more relevance to the results of this thesis and allow for a more synergistic measure of water tree degradation in cables. Addressing this shortcoming along with those previously noted will help build upon the work that was done in this thesis and improve the overall understanding of both the water treeing phenomenon and its effects on the health of MV electric cables.

REFERENCES

[1] Gannon, Mary, “When to use medium-voltage cables,” Oct. 21, 2014. https://www.wireandcabletips.com/use-medium-voltage-cables/.

[2] “LV cables application,” *SAMPSISTEMI*. https://www.sampsistemi.com/applications/lv-cables/.

[3] “Low Voltage - Electrical 101.” https://www.electrical101.com/low-voltage.html.

[4] “Difference Between High, Medium and Low Voltages | Generator Voltage Ranges & More!” https://www.generatorsource.com/Articles/Generator-Info/High-Medium-and-Low-Voltage-Differences.aspx.

[5] “High Voltage Wire and Cable | High Voltage Wire and Cable Manufacturer,” *Calmont Wire & Cable*. https://www.calmont.com/products/high-voltage-and-co-extrusion/.

[6] E. Csanyi, “Shielding Of Power Cables,” *EEP - Electrical Engineering Portal,* Dec. 12, 2010. https://electrical-engineering-portal.com/shielding-of-power-cables.

[7] “Medium Voltage Underground Cable White Paper.,” Nuclear Energy Institute, NEI 06-05, Apr. 2006.

[8] V. Buchholz, “Finding the Root Cause - of Power Cable Failures,” *Electric Energy Online*, Dec. 2004. https://electricenergyonline.com/show_article.php?article=186.

[9] “Cable Jacket Types 101 | Anixter.” https://www.anixter.com/en_us/resources/literature/wire-wisdom/cable-jackets-types-101.html.

[10] R. C. Duckworth, A. Ellis, B. Hinderliter, E. Hill, and M. Maurer-Jones, “Aqueous Degradation in Harvested Medium Voltage Cables in Nuclear Power Plants,” in *Proceedings of the 18th International Conference on Environmental Degradation of Materials in Nuclear Power Systems – Water Reactors*, Cham, 2019, pp. 1257–1265, doi: 10.1007/978-3-030-04639-2_80.

[11] E. Csanyi, “The Good, The Bad and The Ugly Cable Insulation,” *EEP - Electrical Engineering Portal*, Oct. 23, 2012. https://electrical-engineering-portal.com/the-good-bad-ugly-cable-insulation.

[12] “Dictionary of defects for cables – maintenance work↓ service life↑.” https://www.igus.eu/info/unharnessed-cables-dictionary-of-defects.

[13] G. Wilson, “Inaccessible or Underground Power Cable Failures that Disable Accident Mitigation Systems or Cause Plant Transients,” Nuclear Regulatory Commission, GL 2007-01, Nov. 2008.

[14] S. L. Nunes and M. T. Shaw, “Water Treeing in Polyethylene - A Review of Mechanisms,” *IEEE Transactions on Electrical Insulation*, vol. EI-15, no. 6, pp. 437–450, Dec. 1980, doi: 10.1109/TEI.1980.298272.

[15] W. Shu, J. Guo, and S. A. Boggs, “Water treeing in low voltage cables,” *IEEE Electrical Insulation Magazine*, vol. 29, no. 2, pp. 63–68, Mar. 2013, doi: 10.1109/MEI.2013.6457600.

[16] B. Hickman, “Captured Lightning - Bert Hickman’s web site about Lichtenberg Figures, Coin Shrinking, Nikola Tesla, Pulsed Power, and big Arcs and Sparks.” http://capturedlightning.com/.

[17] “Lightning Strikes,” *Teague Insurance*, Oct. 10, 2018. https://www.teagueins.com/2018/10/10/lightning-strikes/.

[18] R. M. Eichhorn, “Treeing in Solid Extruded Electrical Insulation,” *IEEE Transactions on Electrical Insulation*, vol. EI-12, no. 1, pp. 2–18, Feb. 1977, doi: 10.1109/TEI.1977.298001.

[19] W. B. Glew *et al.*, “TESTIMONY OF ENTERGY WITNESSES ALAN B. COX, ROGER B. RUCKER, THOMAS S. MCCAFFREY, AND HOWARD G. SEDDING CONCERNING CONTENTIONS NYS-6/NYS-7 (NON-EQ INACCESSIBLE MEDIUM- AND LOW-VOLTAGE CABLES),” p. 87.

[20] Q. Chen, K. Burkes, E. Makram, R. Hadidi, and X. Xu, “Capacitance of Water Tree Modeling in Underground Cables,” *Journal of Power and Energy Engineering*, vol. 2, no. 11, Art. no. 11, Nov. 2014, doi: 10.4236/jpee.2014.211002.

[21] S. Famakin and C. Kim, “Modeling for Underground Cable Water Tree Growth Dynamics,” *Journal of Power and Energy Engineering*, vol. 07, pp. 51–65, Jan. 2019, doi: 10.4236/jpee.2019.712004.

[22] D. Editor, “Water Tree in XLPE Cable.,” *TNB Electrical Engineer*, Dec. 28, 2009. http://tnbelectricaleng.blogspot.com/2009/12/water-tree-in-xlpe-cable.html.

[23] N. Hampton, R. Hartlein, H. Lennartsson, H. Orton, and R. Ramachandran, “LONG-LIFE XLPE INSULATED POWER CABLE,” p. 6.

[24] B. Lanz and B. Corrente, “Water Trees Don’t Fail Cable,” *IMCorp*. https://www.imcorp.com/imcorp-blog?article=42.

[25] E. H. Doedens, “Organic Contaminants in Crosslinked Polyethylene for Demanding High Voltage Applications,” Chalmers University of Technology.

[26] A. Eccles, L. A. Dissado, J. C. Fothergill, and J. A. Houlgreave, “Water tree inception-experimental support for a mechanical/chemical/electrical theory,” in *1992., Sixth International Conference on Dielectric Materials, Measurements and Applications*, Sep. 1992, pp. 294–297.

[27] J.- Crine and J. Jow, “A water treeing model,” *IEEE Transactions on Dielectrics and Electrical Insulation*, vol. 12, no. 4, pp. 801–808, Aug. 2005, doi: 10.1109/TDEI.2005.1511105.

[28] *Testimony of Entergy Witnesses Alan B. Cox, Roger B. Rucker, Thomas S. McCaffrey, and Howard G. Sedding Concerning Contentions NYS-6/NYS-7 (Non-Eq Inaccessible Medium- and Low-Voltage Cables*. 2012.

[29] A. El-Zein, M. M. E. Bahy, and M. Talaat, “Types of electrical trees in solid insulation under electrical and mechanical energy basis,” in *2008 12th International Middle-East Power System Conference*, Mar. 2008, pp. 80–84, doi: 10.1109/MEPCON.2008.4562308.

[30] M. Huang, K. Zhou, W. Tao, M. Yang, and D. Yang, “Transformation mechanism of electrical tree to water tree in XLPE cables,” in *2014 International Conference on Power System Technology*, Oct. 2014, pp. 1491–1496, doi: 10.1109/POWERCON.2014.6993780.

[31] M. Morita, K. Wu, F. Komori, and Y. Suzuoki, “Investigation of electrical tree propagation from water tree by utilizing partial discharge and optical observation,” in

Proceedings of the 7th International Conference on Properties and Applications of Dielectric Materials (Cat. No.03CH37417), Jun. 2003, vol. 3, pp. 891–894 vol.3, doi: 10.1109/ICPADM.2003.1218565.

[32] Y. Suzuoki *et al.*, "Inception and propagation of electrical tree from water tree degradation [polyethylene cable insulation]," in *The 17th Annual Meeting of the IEEE Lasers and Electro-Optics Society, 2004. LEOS 2004.*, Oct. 2004, pp. 302–305, doi: 10.1109/CEIDP.2004.1364248.

[33] T. Yamaguchi, T. Kato, Y. Suzuoki, F. Komori, T. Tsuji, and H. Mashima, "Influence of structural change by water-tree degradation on electrical-tree inception voltage," in *Proceedings of 2011 International Symposium on Electrical Insulating Materials*, Sep. 2011, pp. 229–232, doi: 10.1109/ISEIM.2011.6826274.

[34] S. Rasikawan, H. Ishihara, and N. Shimizu, "Comparison Between Water-Treed and Deteriorated Regions Electrical Tree Precursor," *Dielectrics and Electrical Insulation, IEEE Transactions on*, vol. 1, pp. 597–603, Sep. 1994, doi: 10.1109/94.311702.

[35] Y. Hayashi, Y. Suzuoki, T. Kato, F. Komori, and H. Mashima, "Temperature dependence of inception of electrical tree from water-tree degradation," in *2009 IEEE Conference on Electrical Insulation and Dielectric Phenomena*, Oct. 2009, pp. 498–501, doi: 10.1109/CEIDP.2009.5377732.

[36] N. Shimizu and C. Laurent, "Electrical tree initiation," *IEEE Transactions on Dielectrics and Electrical Insulation*, vol. 5, no. 5, pp. 651–659, Oct. 1998, doi: 10.1109/94.729688.

[37] “Electron-avalanche Meaning | Best 1 Definitions of Electron-avalanche.” https://www.yourdictionary.com/electron-avalanche.

[38] J. Brown *et al.*, “Submerged Medium Voltage Cable Systems at Nuclear Power Plants: A Review of Research Efforts Relevant to Aging Mechanisms and Condition Monitoring,” 2015, doi: 10.2172/1177756.

[39] “Infrared & Thermal Imaging Applications.” https://www.techimaging.com/applications/infrared-thermal-imaging-applications.

[40] “IEEE Guide for Field Testing and Evaluation of the Insulation of Shielded Power Cable Systems Rated 5 kV and Above,” *IEEE Std 400-2012 (Revision of IEEE Std 400-2001)*, pp. 1–54, Jun. 2012, doi: 10.1109/IEEESTD.2012.6213052.

[41] C.-W. Ha, K.-N. Jang, and S.-C. Jeong, “Diagnosis of MV Power Cables for Nuclear Power Plants,” *Journal of International Council on Electrical Engineering*, vol. 2, no. 3, pp. 317–320, Jul. 2012, doi: 10.5370/JICEE.2012.2.3.317.

[42] W. Zhang, H. Li, C. Liu, and K. C. Tan, “A Technique for Assessment of Thermal Condition and Current Rating of Underground Power Cables Installed in Duct Banks,” in *2012 Asia-Pacific Power and Energy Engineering Conference*, Mar. 2012, pp. 1–6, doi: 10.1109/APPEEC.2012.6307374.

[43] M. Sha, S. Taib, and S. Kabir, “Infrared thermography for assessing and monitoring electrical components within concrete structures,” *Progress in Electromagnetics Research Symposium*, pp. 786–789, Jan. 2011.

[44] J. C. Hernández Mejía, “Characterization of real power cable defects by diagnostic measurements,” Nov. 2008, Available: https://smartech.gatech.edu/handle/1853/31841.

[45] “Hipot Cable Testing.” KharkovEnergoPribor Ltd.

[46] “The Basics of Time Domain Reflectometry (TDR),” *HV Technologies*, Oct. 18, 2018. https://hvtechnologies.com/the-basics-of-time-domain-reflectometry-tdr/.

[47] N. A. Muhamad, T. Phung, T. Blackburn, and K. X. Lai, *Polarization and Depolarization Current (PDC) tests on biodegradable and mineral transformer oils at different moisture levels*. 2009, p. 6.

[48] “Dissipation/Power Factor Measurement.” https://omnexus.specialchem.com/polymer-properties/properties/dissipation-factor.

[49] Zuoqian Wang *et al.*, “Mechanical fatigue as a mechanism of water tree propagation in TR-XLPE,” *IEEE Trans. Dielect. Electr. Insul.*, vol. 19, no. 1, pp. 321–330, Feb. 2012, doi: 10.1109/TDEI.2012.6148534.

[50] E. Khouildi, R. Attia, and R. Cherni, “Investigating Thermal Effect on a Cross Linked Polyethylene Power Cable,” *TELKOMNIKA Indonesian Journal of Electrical Engineering*, vol. 5, Feb. 2017, doi: 10.11591/ijeecs.v2.i2.pages.

[51] Z. Xia *et al.*, “Electric Field and Temperature Distribution of High Voltage Cables with the Addition of Particles based on COMSOL Simulation,” in *2020 IEEE International Conference on High Voltage Engineering and Application (ICHVE)*, Sep. 2020, pp. 1–4, doi: 10.1109/ICHVE49031.2020.9280024.

[52] K. Burkes, E. Makram, and R. Hadidi, “Modeling the Effect of a Water Tree inside Tape Shield and Concentric Neutral Cables,” *undefined*, 2014, [Online]. Available: /paper/Modeling-the-Effect-of-a-Water-Tree-inside-Tape-and-Burkes-Makram/a34c849a6e42a74a3f17b898d3b90a2da979c2cb.

[53] J. Liu *et al.*, “Analysis of electric field distribution of cable insulation defects,” *J. Phys.: Conf. Ser.*, vol. 1087, p. 042040, Sep. 2018, doi: 10.1088/1742-6596/1087/4/042040.

[54] M. Alsharif, P. A. Wallace, D. M. Hepburn, and C. Zhou, “FEM Modelling of Electric Field and Potential Distributions of MV XLPE Cables Containing Void Defect,” p. 4, 2012.

[55] N. Promvichai, K. Minja, P. V. Chombo, T. Suphanarapan, T. Boonraksa, and B. Marungsri, *Effects of Ionic solutions in Water Treeing Propagation of XLPE Insulated HV Cable by Using ANSYS MAXWELL 2D*. 2017, p. 266.

[56] M. Kachi, M. Nemamcha, L. Herous, and M. Houabes, *Effect of Water Treeing on Electrical Properties of XLPE Cables*. 2009.

[57] J. Wang, J. Wu, Y. Li, and X. Zheng, “Simulation of Electric Field Distributions in Water Treed XLPE Using Finite Element Method,” in *2012 Spring Congress on Engineering and Technology*, May 2012, pp. 1–4, doi: 10.1109/SCET.2012.6341942.

[58] T. Maeda, D. Kaneko, Y. Ohki, T. Konishi, Y. Nakamichi, and M. Okashita, “Effect of the applied voltage frequency on the water tree shape in polyethylene,” in *Proceedings of the 2004 IEEE International Conference on Solid Dielectrics, 2004. ICSD 2004.*, Jul. 2004, vol. 1, pp. 276-279 Vol.1, doi: 10.1109/ICSD.2004.1350344.

[59] N. Promvichai, T. Boonraksa, and B. Marungsri, “The ionic solutions effects to degradation on XLPE insulated underground cable with environmental model,” *GMSARN International Journal*, vol. 13, pp. 12–25, Mar. 2019.

[60] M. I. Qureshi, N. H. Malik, and A. A. Al-Arainy, “Impact of cations toward the water tree propensity in crosslinked polyethylene insulation,” *Journal of King Saud University - Engineering Sciences*, vol. 23, no. 1, pp. 43–48, Jan. 2011, doi: 10.1016/j.jksues.2010.01.002.

[61] T. Boonraksa and B. Marungsri, “Role of Ionic Solutions Affect Water Treeing Propagation in XLPE Insulation for High Voltage Cable,” *International Journal of Electrical and Computer Engineering*, vol. 8, no. 5, pp. 795–798, May 2014.

[62] L. Huimin, B. H. Crichton, and R. A. Fouracre, “The association between ion-ion interaction in solution and water tree degradation of polymeric electrical insulation,” *J. Phys. D: Appl. Phys.*, vol. 24, no. 8, pp. 1436–1442, Aug. 1991, doi: 10.1088/0022-3727/24/8/031.

[63] A. A. Al-Arainy, A. A. Ahaideb, M. I. Qureshi, and N. H. Malik, “Statistical evaluation of water tree lengths in XLPE cables at different temperatures,” *IEEE Transactions on Dielectrics and Electrical Insulation*, vol. 11, no. 6, pp. 995–1006, Dec. 2004, doi: 10.1109/TDEI.2004.1387823.

[64] F. Mauseth, M. Amundsen, A. Lind, and H. Faremo, “Water tree growth of wet XLPE insulation stressed with DC and high frequency AC,” in *2012 Annual Report Conference on Electrical Insulation and Dielectric Phenomena*, Oct. 2012, pp. 692–695, doi: 10.1109/CEIDP.2012.6378875.

[65] I. Radu, M. Acedo, J. C. Filippini, P. Notingher, and F. Ftutos, “The effect of water treeing on the electric field distribution of XLPE,” *Dielectrics and Electrical Insulation, IEEE Transactions on*, vol. 7, pp. 860–868, Jan. 2001, doi: 10.1109/94.892001.

[66] A. T. Bulinski, S. S. Bamji, and R. J. Densley, “The Effects of Frequency and Temperature on Water Tree Degradation of Miniature XLPE Cables,” *IEEE Transactions on Electrical Insulation*, vol. EI-21, no. 4, pp. 645–650, Aug. 1986, doi: 10.1109/TEI.1986.348970.

[67] A. Garton, S. Bamji, A. Bulinski, and J. Densley, “Oxidation and Water Tree Formation in Service-Aged XLPE Cable Insulation,” *IEEE Transactions on Electrical Insulation*, vol. EI-22, no. 4, pp. 405–412, Aug. 1987, doi: 10.1109/TEI.1987.298900.

[68] Z. Lei *et al.*, “Influence of temperature on dielectric properties of EPR and partial discharge behavior of spherical cavity in EPR insulation,” *IEEE Transactions on Dielectrics and Electrical Insulation*, vol. 22, no. 6, pp. 3488–3497, Dec. 2015, doi: 10.1109/TDEI.2015.004942.

[69] R. Duckworth, A. R. Ellis, and T. Ha, “ELECTRICAL BREAKDOWN STRENGTH AND AC WITHSTAND IN HARVESTED EPR INSULATIONS FOR NUCLEAR POWER PLANTS,” Oak Ridge National Lab. (ORNL), Oak Ridge, TN (United States), Nov. 2019. [Online]. Available: https://www.osti.gov/biblio/1607164.

[70] L. Cao and S. Grzybowski, “Life-time characteristics of EPR cable insulation under electrical and thermal stresses,” in *2013 IEEE International Conference on Solid Dielectrics (ICSD)*, Jun. 2013, pp. 632–635, doi: 10.1109/ICSD.2013.6619873.

[71] D09 Committee, “Test Method for Dielectric Breakdown Voltage and Dielectric Strength of Solid Electrical Insulating Materials at Commercial Power Frequencies,” ASTM International. doi: 10.1520/D0149-20.

[72] J. G. Brennan, “Dielectric Heating - an overview | ScienceDirect Topics.” https://www.sciencedirect.com/topics/medicine-and-dentistry/dielectric-heating.

[73] Z. Lei *et al.*, “Influence of cavities on the dielectric properties of Ethylene Propylene Rubber insulation,” in *Proceedings of 2014 International Symposium on Electrical Insulating Materials*, Jun. 2014, pp. 437–440, doi: 10.1109/ISEIM.2014.6870812.

[74] J. Wu, H. Jin, A. R. Mor, and J. Smit, “The effect of frequency on the dielectric breakdown of insulation materials in HV cable systems,” in *2017 International Symposium on Electrical Insulating Materials (ISEIM)*, Sep. 2017, vol. 1, pp. 251–254, doi: 10.23919/ISEIM.2017.8088734.

[75] “Lecture 6: Meshing and Mesh Operations ANSYS Maxwell V16 Training Manual.”

[76] C. Fairclough, “Efficiently Mesh Your Model Geometry with Meshing Sequences,” *COMSOL Multiphysics*. https://www.comsol.com/blogs/efficiently-mesh-your-model-geometry-with-meshing-sequences/.

[77] “Improving Convergence of Nonlinear Stationary Models - Knowledge Base.” https://www.comsol.com/support/knowledgebase/103.

[78] J. C. Chan, M. D. Hartley, and L. J. Hiivala, “Performance characteristics of XLPE versus EPR as insulation for high voltage cables,” *IEEE Electrical Insulation Magazine*, vol. 9, no. 3, pp. 8–12, May 1993, doi: 10.1109/57.216782.

[79] A. Wicker, “Nexans Technical Review,” Nexans, Oct. 2004.

[80] K. W. Burkes, “Water Tree Analysis and On-Line Detection Algorithm Using Time Domain Relectometry,” Clemson University.

[81] “Introduction to the AC/DC Module,” p. 50.

[82] “High Temperature Operation of Extruded Distribution Cable Systems,” Georgia Tech Research Corporation, White Paper, Oct. 2018.

[83] R. M. Eichhorn, “A Critical Comparison of XLPE-and EPR for Use as Electrical Insulation on Underground Power Cables,” *IEEE Transactions on Electrical Insulation*, vol. EI-16, no. 6, pp. 469–482, Dec. 1981, doi: 10.1109/TEI.1981.298377.

[84] V. Dubickas, H. Edin, and R. Papazyan, “Cable diagnostics with on-voltage time domain reflectometry,” Jan. 2006.

[85] D19 Committee, “Test Methods for Electrical Conductivity and Resistivity of Water,” ASTM International. doi: 10.1520/D1125-14.

[86] C. G. Malmberg and A. A. Maryott, “Dielectric constant of water from 0 to 100 C,” *J. RES. NATL. BUR. STAN.*, vol. 56, no. 1, p. 1, Jan. 1956, doi: 10.6028/jres.056.001.

[87] G. C. Akerlof and H. I. Oshry, “The Dielectric Constant of Water at High Temperatures and in Equilibrium with its Vapor,” *J. Am. Chem. Soc.*, vol. 72, no. 7, pp. 2844–2847, Jul. 1950, doi: 10.1021/ja01163a006.

[88] C. Akilan, “Thermodynamic and Related Studies of Aqueous Copper (II) Sulfate Solutions,” Murdoch University Western Australia, 2008.

[89] M. W. Chase, “NIST-JANAF Themochemical Tables, Fourth Edition,” *J. Phys. Chem. Ref. Data, Monograph 9*, pp. 1–1951, 1998.

[90] “Water - Thermal Conductivity.” https://www.engineeringtoolbox.com/water-liquid-gas-thermal-conductivity-temperature-pressure-d_2012.html.

[91] “Water - Specific Heat.” https://www.engineeringtoolbox.com/specific-heat-capacity-water-d_660.html.

[92] I. Zaytsev and G. Aseyev, *Properties of Aqueous Solutions of Electrolytes*. CRC Press, 1992.

[93] H. St-Onge, “Research to determine the acceptable emergency operating temperatures for extruded dielectric cables. Final report,” SEE CODE- 9698356 Hydro-Quebec, Varennes (Canada). Research Inst., EPRI-EL-938, Nov. 1978. doi: 10.2172/6529299.

[94] Z. Pšenáková, M. Šmondrk, and M. Beňová, “MODELLING AND SIMULATION OF THE ELECTRIC FIELD STRENGTH DISTRIBUTION IN A HUMAN HEAD MODEL BY 2,4 GHZ RADIOFREQUENCY RADIATION,” p. 4.

[95] I. C. on N.-I. R. Protection (ICNIRP)1, “Guidelines for Limiting Exposure to Electromagnetic Fields (100 kHz to 300 GHz),” *Health Physics*, vol. 118, no. 5, pp. 483–524, May 2020, doi: 10.1097/HP.0000000000001210.

[96] J. Tang and F. P. Resurreccion Jr., “Dielectric Medium - an overview | ScienceDirect Topics.” https://www.sciencedirect.com/topics/engineering/dielectric-medium.

[97] “Magnetic properties of materials.” http://info.ee.surrey.ac.uk/Workshop/advice/coils/mu/.

[98] J. D. Cutnell and K. W. Johnson, *Physics*. John Wiley & Sons, 2009.

[99] P. R. Wainwright, “The relationship of temperature rise to specific absorption rate and current in the human leg for exposure to electromagnetic radiation in the high frequency band,” *Phys Med Biol*, vol. 48, no. 19, pp. 3143–3155, Oct. 2003, doi: 10.1088/0031-9155/48/19/004.

[100] Y. Seo and Z. J. Wang, “Measurement and evaluation of specific absorption rate and temperature elevation caused by an artificial hip joint during MRI scanning,” *Scientific Reports*, vol. 11, no. 1, Art. no. 1, Jan. 2021, doi: 10.1038/s41598-020-80828-7.

[101] Z. Lei *et al.*, “Influence of temperature on dielectric properties of EPR and partial discharge behavior of spherical cavity in EPR insulation,” *IEEE Transactions on Dielectrics and Electrical Insulation*, vol. 22, no. 6, pp. 3488–3497, Dec. 2015, doi: 10.1109/TDEI.2015.004942.

[102] A. A. Volkov, V. G. Artemov, and A. V. Pronin, “A radically new suggestion about the electrodynamics of water: Can the pH index and the Debye relaxation be of a common origin?,” *EPL*, vol. 106, no. 4, p. 46004, May 2014, doi: 10.1209/0295-5075/106/46004.

[103] M. Brown, “Compounding of ethylene-propylene polymers for electrical applications,” *IEEE Electrical Insulation Magazine*, vol. 10, no. 1, pp. 16–22, Jan. 1994, doi: 10.1109/57.259977.

APPENDIX A:
ANALYTICAL SOLUTION EQUATIONS USED FOR VERIFICATION OF PRELIMINARY SIMULATIONS

The following equations were used to calculate the capacitance and resistance analytical solutions for the purpose of verifying the preliminary simulations described in Chapter Three.

Capacitance for the 2D coaxial cable geometry type with a single dielectric:

$$\frac{C}{L} = \frac{2\pi\varepsilon_R\varepsilon_0}{ln\,(\frac{r_1}{r_4})} \tag{5}$$

where, C is capacitance (F), L is model length (m), ε_R is relative permittivity of the dielectric, ε_0 is permittivity of free space (8.854 * 10^{-12} F m^{-1}), r_1 is radius of the dielectric (m), and r_4 is radius of the conductor (m).

Resistance for the 2D coaxial cable geometry type with a single dielectric:

$$RL = \frac{ln\,(\frac{r_1}{r_4})}{2\pi\sigma} \tag{6}$$

where, R is resistance (Ω), r_1 is radius of the dielectric (m), r_4 is radius of the conductor (m), σ is electrical conductivity of the dielectric (S m^{-1}), and L is model length (m).

Capacitance for the 3D coaxial cable geometry type with a single dielectric:

$$C = \frac{2\pi\varepsilon_R\varepsilon_0 L}{ln\,(\frac{r_1}{r_4})} \tag{7}$$

where, C is capacitance (F), L is model length (m), ε_R is relative permittivity of the dielectric, ε_0 is permittivity of free space (8.854 * 10^{-12} F m^{-1}), r_1 is radius of the dielectric (m), and r_4 is radius of the conductor (m).

Resistance for the 3D coaxial cable geometry type with a single dielectric:

$$R = \frac{ln\,(\frac{r_1}{r_4})}{2\pi\sigma L} \tag{8}$$

where, R is resistance (Ω), r_1 is radius of the dielectric (m), r_4 is radius of the conductor (m), σ is electrical conductivity of the dielectric (S m^{-1}), and L is model length (m).

Capacitance for the 2D coaxial cable geometry type with a mixed dielectric:

$$\frac{C}{L} = \frac{2\pi\varepsilon_0\varepsilon_{R_1}\varepsilon_{R_2}\varepsilon_{R_3}}{\varepsilon_{R_2}\varepsilon_{R_3}\,ln\,(\frac{r_3}{r_4})\,\varepsilon_{R_1}\varepsilon_{R_3}\,ln\,(\frac{r_2}{r_3})\,\varepsilon_{R_1}\varepsilon_{R_2}\,ln\,(\frac{r_1}{r_2})} \tag{9}$$

where, C is capacitance (F), L is model length (m), ε_0 is permittivity of free space (8.854 * 10^{-12} F m^{-1}), ε_{R1} is relative permittivity of dielectric #1, ε_{R2} is relative permittivity of dielectric #2, ε_{R3} is relative permittivity of dielectric #3, r_3 is radius of dielectric #3 (m), r_4 is radius of the conductor (m), r_2 is radius of dielectric #2 (m), and r_1 is radius of dielectric #1 (m).

Resistance for the 2D coaxial cable geometry type with a mixed dielectric:

$$\frac{R}{L} = \frac{ln\,(\frac{r_1}{r_4})}{2\pi\sigma} \tag{10}$$

where, R is resistance (Ω), L is model length (m), r_1 is radius of dielectric #1 (m), r_4 is radius of the conductor (m), and σ is electrical conductivity of the dielectric (S m^{-1}).

Capacitance for the 3D coaxial cable geometry type with a mixed dielectric:

$$C = \frac{2\pi\varepsilon_0\varepsilon_{R_1}\varepsilon_{R_2}\varepsilon_{R_3}L}{\varepsilon_{R_2}\varepsilon_{R_3}\,ln(\frac{r_3}{r_4})\,\varepsilon_{R_1}\varepsilon_{R_3}\,ln(\frac{r_2}{r_3})\,\varepsilon_{R_1}\varepsilon_{R_2}\,ln(\frac{r_1}{r_2})} \tag{11}$$

where, C is capacitance (F), ε_0 is permittivity of free space (8.854 * 10^{-12} F m^{-1}), ε_{R1} is relative permittivity of dielectric #1, ε_{R2} is relative permittivity of dielectric #2, ε_{R3} is relative permittivity of dielectric #3, L is model length (m), r_3 is radius of dielectric #3 (m), r_4 is radius of the conductor (m), r_2 is radius of dielectric #2 (m), and r_1 is radius of dielectric #1 (m).

Resistance for the 3D coaxial cable geometry type with a mixed dielectric:

$$R = \frac{ln\left(\frac{r_1}{r_4}\right)}{2\pi\sigma L} \tag{12}$$

where, R is resistance (Ω), r_1 is radius of dielectric #1 (m), r_4 is radius of the conductor (m), σ is electrical conductivity of the dielectric (S m^{-1}), and L is model length (m).

Capacitance for the 2D parallel plate geometry type with a single dielectric:

$$\frac{C}{L} = \frac{\varepsilon_R \varepsilon_0}{d} \tag{13}$$

where, C is capacitance (F), L is model length (m), ε_R is relative permittivity of the dielectric, ε_0 is permittivity of free space (8.854 * 10^{-12} F m^{-1}), and d is distance between the charged plates (m).

Resistance for the 2D parallel plate geometry type with a single dielectric:

$$\frac{R}{L} = \frac{1}{\sigma d} \tag{14}$$

where, R is resistance (Ω), L is model length (m), σ is electrical conductivity of the dielectric (S m^{-1}), and d is distance between charged plates (m).

Capacitance for the 3D parallel plate geometry type with a single dielectric:

$$C = \frac{\varepsilon_R \varepsilon_0 A}{d} \tag{15}$$

where, C is capacitance (F), ε_R is relative permittivity of the dielectric, ε_0 is permittivity of free space (8.854 * 10^{-12} F m^{-1}), and A is area of the charged plate (m^2).

Resistance for the 3D parallel plate geometry type with a single dielectric:

$$R = \frac{L}{\sigma A} \tag{16}$$

where, R is resistance (Ω), L is model length (m), σ is electrical conductivity of the dielectric (S m^{-1}), and A is area of the charged plate (m^2).

Capacitance for the 2D parallel plate geometry type with a mixed dielectric:

$$\frac{C}{L} = \frac{\varepsilon_0}{\frac{d_1}{\varepsilon_{R_1}} + \frac{d_2}{\varepsilon_{R_2}} + \frac{d_3}{\varepsilon_{R_3}}} \tag{17}$$

where, C is capacitance (F), L is model length (m), ε_0 is permittivity of free space (8.854 * 10^{-12} F m^{-1}), d_1 is width of dielectric #1 (m), ε_{R1} is relative permittivity of dielectric #1, d_2 is width of dielectric #2 (m), ε_{R2} is relative permittivity of dielectric #2, d_3 is width of dielectric #3 (m), and ε_{R3} is relative permittivity of dielectric #3.

Resistance for the 2D parallel plate geometry type with a mixed dielectric:

$$\frac{R}{L} = \frac{1}{\sigma d} \tag{18}$$

where, R is resistance (Ω), L is model length (m), σ is electrical conductivity of the dielectric (S m^{-1}), and d is distance between charged plates (m).

Capacitance for the 3D parallel plate geometry type with a mixed dielectric:

$$C = \frac{\varepsilon_0 A}{\frac{d_1}{\varepsilon_{R_1}} + \frac{d_2}{\varepsilon_{R_2}} + \frac{d_3}{\varepsilon_{R_3}}} \tag{19}$$

where, C is capacitance (F), ε_0 is permittivity of free space (8.854 * 10^{-12} F m^{-1}), A is area of the charged plate (m^2), d_1 is width of dielectric #1 (m), ε_{R1} is relative permittivity of dielectric #1, d_2 is width of dielectric #2 (m), ε_{R2} is relative permittivity of dielectric #2, d_3 is width of dielectric #3 (m), and ε_{R3} is relative permittivity of dielectric #3.

Resistance for the 3D parallel plate geometry type with a mixed dielectric:

$$R = \frac{L}{\sigma A} \tag{20}$$

where, R is resistance (Ω), L is model length (m), σ is electrical conductivity of the dielectric (S m^{-1}), and A is area of the charged plate (m^2).

APPENDIX B:
PRELIMINARY SIMULATION ANALYTICAL RESULTS

Tables 3 and 4 provide the analytical solution results referenced in Chapter Three, while tables 5 and 6 provide the relative errors. For each geometry type, configuration, and dielectric setup, capacitance and resistance values obtained through analytical calculation, Ansys, and COMSOL, are provided. It is noted that each value uses insignificant digits which were required for this comparison.

Table 3. Preliminary simulation results using the coaxial cable geometry type.

Coaxial Cable	**Analytical Solution**	**Ansys**	**COMSOL**
Single Dielectric, 2D	C = 367.66 pF m^{-1}	C = 367.25 pF m^{-1}	C = 367.67 pF m^{-1}
	R = 54.184 TΩ m^{-1}	R = 54.245 TΩ m^{-1}	R = 54.184 TΩ m^{-1}
Single Dielectric, 3D	C = 367.66 pF	C = 368.08 pF	C = 367.67 pF
	R = 54.184 TΩ		R = 54.184 TΩ
Mixed Dielectric, 2D	C = 326.47 pF m^{-1}	C = 320.03 pF m^{-1}	C = 320.35 pF m^{-1}
	R = 54.184 TΩ m^{-1}	R = 53.686 TΩ m^{-1}	R = 54.184 TΩ m^{-1}
Mixed Dielectric, 3D	C = 326.47 pF	C = 320.63 pF	C = 320.35 pF
	R = 54.184 TΩ		R = 54.184 TΩ

Table 4. Preliminary simulation results using the parallel plate geometry type.

Parallel Plate	**Analytical Solution**	**Ansys**	**COMSOL**
Single Dielectric, 2D	C = 99.608 pF m^{-1}	C = 99.610 pF m^{-1}	C = 99.610 pF m^{-1}
	R = 200.00 TΩ m^{-1}	R = 200.00 TΩ m^{-1}	R = 200.00 TΩ m^{-1}
Single Dielectric, 3D	C = 1.4941 pF	C = 1.4941 pF	C = 1.4941 pF
	R = 13,333 TΩ	R = 12,361 TΩ	R = 13,333 TΩ
Mixed Dielectric, 2D	C = 87.613 pF m^{-1}	C = 87.615 pF m^{-1}	C = 87.615 pF m^{-1}
	R = 200.00 TΩ m^{-1}	R = 197.91 TΩ m^{-1}	R = 200.00 TΩ m^{-1}
Mixed Dielectric, 3D	C = 1.3142 pF	C = 1.3142 pF	C = 1.3142 pF
	R = 13,333 TΩ	R = 12,503 TΩ	R = 13,333 TΩ

Table 5. Relative errors between Ansys and the analytical solutions, and between COMSOL and the analytical solution, respectively, for the coaxial cable geometry type.

Coaxial Cable	Relative Error	Parameter
Single Dielectric, 2D Setting	0.1% / 0.003%	Capacitance
	0.1% / Zero	Resistance
Single Dielectric, 3D Setting	0.1% / 0.003%	Capacitance
	N/A / Zero	Resistance
Mixed Dielectric, 2D Setting	2% / 2%	Capacitance
	0.5% / Zero	Resistance
Mixed Dielectric, 3D Setting	2% / 2%	Capacitance
	N/A / Zero	Resistance

Table 6. Relative errors between Ansys and the analytical solutions, and between COMSOL and the analytical solution, respectively, for the parallel plate geometry type.

Parallel Plate	Relative Error	Parameter
Single Dielectric, 2D Setting	0.002% / 0.002%	Capacitance
	Zero / Zero	Resistance
Single Dielectric, 3D Setting	Zero / Zero	Capacitance
	7% / Zero	Resistance
Mixed Dielectric, 2D Setting	0.001% / 0.001%	Capacitance
	1% / Zero	Resistance
Mixed Dielectric, 3D Setting	Zero / Zero	Capacitance
	6% / Zero	Resistance

APPENDIX C:

ELECTRICAL PROPERTIES OF WATER TREE COMPOSITIONS

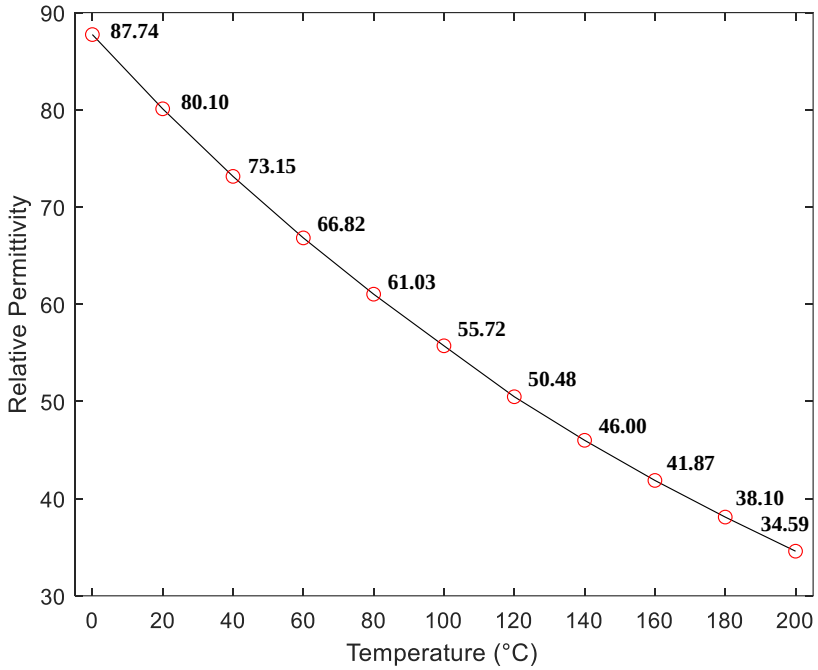

Figure 62. Relative permittivity versus temperature for the H_2O composition.

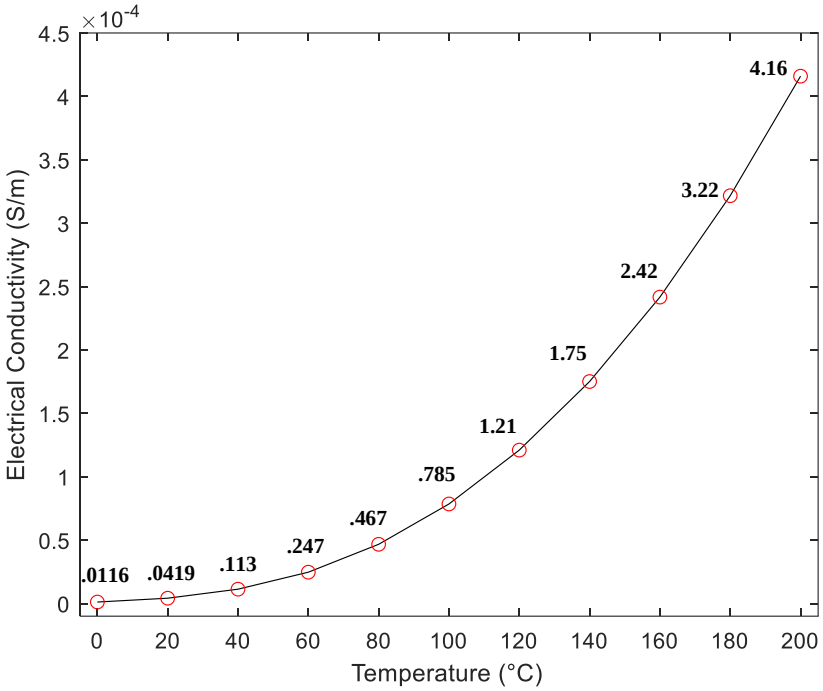

Figure 63. Electrical conductivity versus temperature for the H_2O composition.

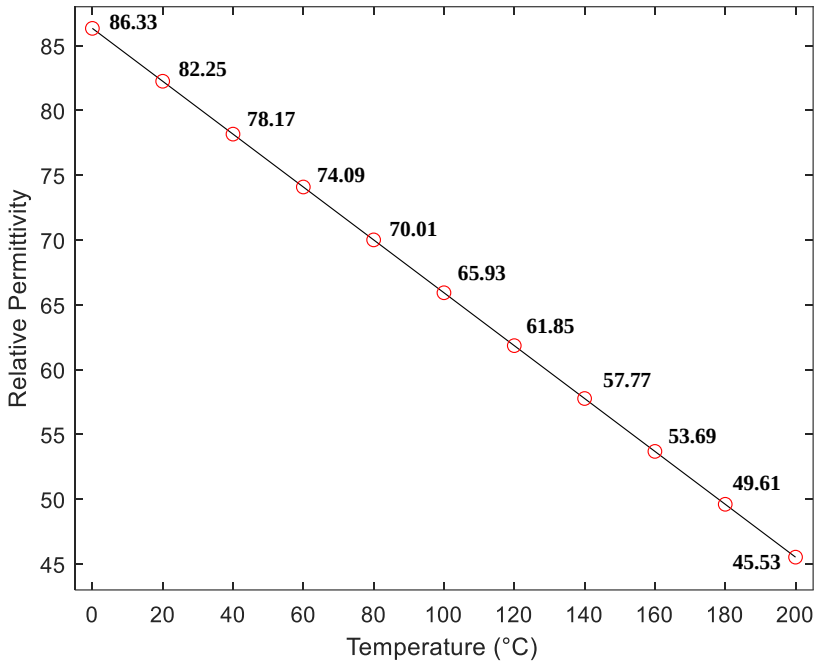

Figure 64. Relative permittivity versus temperature for the $CuSO_4$ composition.

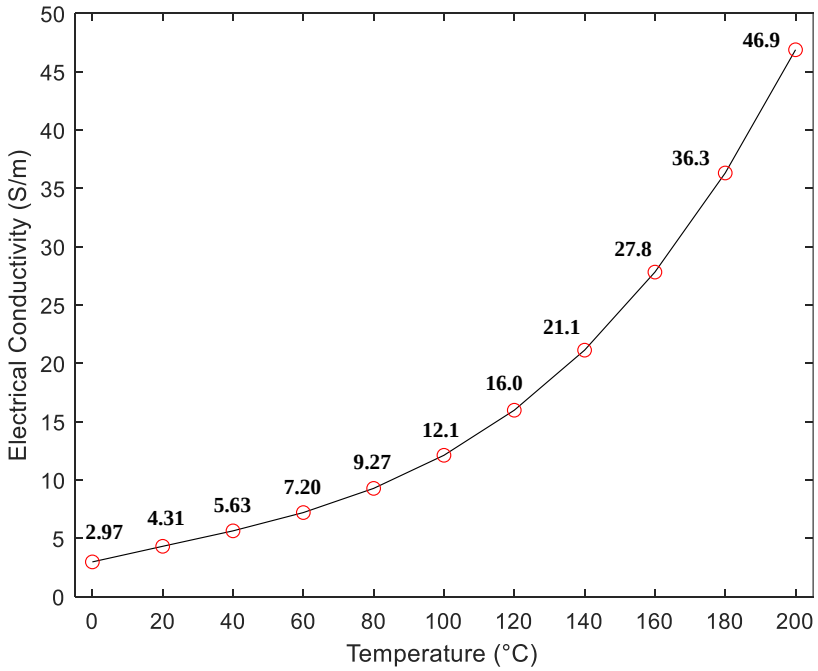

Figure 65. Electrical conductivity versus temperature for the $CuSO_4$ composition.